Dissertation
submitted to the
Combined Faculty of Mathematics, Engineering and Natural Sciences
of Heidelberg University, Germany
for the degree of
Doctor of Natural Sciences

Put forward by
Jeannette Jansen
born in: Mainz, Germany
Oral examination: January 19$^{\text{th}}$, 2022

Oxygen Effects in (FLASH-) Radiotherapy on a Radiochemical and Genetic Level

Referees:

Prof. Dr. Joao Seco
Prof. Dr. Oliver Jäkel

Abstract

In radiotherapy, oxygen acts as strong radiosensitizer and alters cellular response to radiation drastically. Especially, the effect of the so-called FLASH radiotherapy, which applies high dose rates above $40\,\text{Gy/s}$ to spare healthy tissue from radiation damage, is influenced by oxygen. At high O_2 levels the protective effect of FLASH is decreased *in vivo*. The underlying mechanisms are not completely understood yet. In this thesis, oxygen effects were investigated on (i) a radiochemical level by oxygen depletion measurements in water phantoms and together with cancer cells, (ii) on a genetic level developing a novel analysis method on gene expression patterns and (iii) on a mechanistic, radical scavenging level by modulating cellular defense. It was found, that a popular hypothesis for explaining the FLASH effect, the oxygen depletion hypothesis, cannot be solely responsible for the observed altered cellular response after FLASH through radiation induced hypoxia alone. However, radical concentrations are highly dependent on dose rate and beam pulse structure implying potential biological impact. Radical scavenging systems in cells were found to be altered using SOD-mimicking CuL/FeL compounds leading to a decrease of metastatic potential. The results strengthen the link between FLASH effects and radical levels, influenced by radical scavenging systems in cancer cells and oxygen conditions.

Zusammenfassung

Bei der Strahlentherapie wirkt Sauerstoff als starker Strahlensensibilisator und verändert die zelluläre Reaktion auf Strahlung drastisch. Insbesondere die Wirkung der sogenannten FLASH-Strahlentherapie, die mit hohen Dosisleistungen über $40\,\text{Gy/s}$ gesundes Gewebe vor Strahlenschäden bewahrt, wird durch Sauerstoff beeinflusst. Bei hohen O_2-Werten wird die Schutzwirkung von FLASH *in vivo* verringert. Die zugrunde liegenden Mechanismen sind noch nicht vollständig verstanden. In dieser Arbeit wurden Sauerstoffeffekte (i) auf radiochemischer Ebene durch Sauerstoffdepletionsmessungen in Wasserphantomen und zusammen mit Krebszellen gemessen, (ii) auf genetischer Ebene eine neuartige Analysemethode zu Genexpressionsmustern entwickelt und (iii) auf Radikalfängerebene durch Modulation der Zellverteidigung gemessen. Es wurde festgestellt, dass eine populäre Hypothese zur Erklärung des FLASH-Effekts, die Sauerstoffverarmungshypothese, die beobachtete veränderte zelluläre Reaktion nach FLASH nicht allein durch strahlungsinduzierte Hypoxie erklären kann. Radikalkonzentrationen sind jedoch stark abhängig von Dosisleistung und Strahlpulsstruktur, was potenzielle biologische Auswirkungen impliziert. Es wurde festgestellt, dass Radikalfängersysteme in Zellen durch SOD-nachahmende CuL/FeL-Verbindungen verändert werden, was zu einer Verringerung des Metastasepotenzials führt. Die Ergebnisse belegen die Verbindung zwischen FLASH-Effekten und Radikalkonzentrationen, die durch Radikalfängersysteme in Krebszellen und Sauerstoffbedingungen beeinflusst werden.

ii

Contents

Introduction

Nothing in life is to be feared, it is only to be understood.

— Marie Curie

With 17.0 million new cancer cases and 9.5 million cancer deaths worldwide in 2018[1], cancer is one of the most abundant diseases and often ends deadly. Cancer treatment targets the malignant cells to induce a shrinkage of the cancerous tissue with the aim to ideally remove the tumor. Common treatment techniques involve different possibilities: Local treatment like surgery, or radiotherapy of the tumor, or systemic therapies such as chemotherapy and immunotherapy. Often, a combination of different treatment forms is applied.

In radiotherapy, different techniques are available nowadays: The standard procedure is irradiation with photons or electrons; newer techniques also involve the radiotherapy with protons or heavier charged ions such as $^4\text{He}^{2+}$ or $^{12}\text{C}^{6+}$[2]. Current research focuses hereby on irradiation at ultra-high dose rates (so called FLASH irradiation), or irradiation with mini- and microbeams. FLASH is defined as radiotherapy using dose rates higher than 40 Gy/s with the dose rate of single beam pulses reaching more than 10^5 Gy/s[3]. Both FLASH radiation and mini-/microbeams show a comparable tumor response as conventional radiotherapy while side effects are reduced and healthy tissue is optimally spared. These techniques are still under development, but show promising results in first clinical studies.

In all forms of radiation therapy, the presence or absence of oxygen in the target volume plays a critical role as oxygen works as an important radiosensitizer[4,5]. However, the exact mechanisms of the interplay of oxygen and radiation are not fully understood, which is of special importance in explaining mechanisms suitable for understanding FLASH effects. One part of the interplay of oxygen and radiation is

based on radiolytic chemical yields and their impact on cellular material. Another crucial part is the cell's response system, in form of radical scavengers and DNA repair mechanisms.

In this thesis, the aim was to investigate oxygen effects from three different perspectives: (i) on a radiochemical level performing oxygen measurements in water phantoms with respect to potential changes in oxygen abundance due to irradiation with photons, protons and ^{12}C ions at FLASH dose rates; (ii) on a genetic level, where differences in the cells' genetic fingerprints were compared between photon-treatment and non-treatment for oxygen levels of the cells of 0.6 % O_2 and 21 % O_2 and (iii) on a mechanistic, molecular level, where scavenging systems of Reactive Oxygen Species (ROS) were mimicked by metal compounds and the impact of these compounds were tested on cancer cells during radiation with respect to the cells' ability to form metastasis. In addition, the impact of beam pulse structures in proton FLASH beams was investigated in water phantoms and feasibility studies were conducted of joined oxygen measurements in cellular samples. Each of the three aspects i) - iii) have been published in peer reviewed journals and are reprinted in this cumulative thesis as Publications I - III in Chapter 4. Additional work is shown in Appendix A.1, B.1 and B.2.

In the course of this thesis, special focus will be given to FLASH related O_2 mechanisms and cellular response mechanisms. Hence, Chapter 2 will describe the theoretical background of physical radiation processes and provides radiobiological basics. Chapter 3 gives an overview on the state-of-the-art of FLASH research and oxygen-based radiolytic processes.The publications that were developed in the course of this dissertation are presented in Chapter 4 and a discussion and summary follows in Chapter 5 and 6.

Theoretical Background

This thesis investigates the role of oxygen in radiotherapy and focuses deeply on oxygen effects in FLASH radiotherapy. To provide a theoretical background, the aspects of interaction and production of radiation will be described in this chapter, Section 2.1, with a special focus given on the production of FLASH-suitable radiation. The fundamentals of cell structures, as target of radiation in Publication II and III, will be described on a genetic, biochemical and mechanistical level and concepts of radiobiology will be presented in Section 2.2. In both FLASH and conventional radiotherapy, oxygen plays a major role as a radiosensitizer, which will be investigated in detail in all publications in this thesis. As a fundamental background, the role of oxygen in cells will be described in Section 2.3 and knowledge about oxygen-related biochemical processes in cells will be provided.

2.1   Physical Background

In this section, the physical concepts of ionizing radiation and its interaction with matter will be described. A special focus will lie on the production of ionizing radiation at conventional and ultra-high dose rates and the challenges of dosimetry at high dose rates.

2.1.1   Interaction of Ionizing Radiation with Matter

Tumor treatment is usually done by irradiation with photons, electrons or heavy ions of an energy high enough to reach tumors inside a human body. The beam types are different with respect to their physical impact onto the irradiated target. The following section is based on Schlegel and Bille (2002)[6].

Photons

The energy range of photons used in clinical radiotherapy is around 4-6 MeV, while X-ray tubes used for research usually operate at around 220 keV. Depending on the energy of the photon beam, photons will either be absorbed by the target material, or they will be scattered. In all cases, the intensity I of a photon beam decreases exponentially with increasing depth d within an irradiated target. This process is described by the Lambert-Beer-Law:

$$I(d) = I_0 e^{-\mu d},\tag{2.1}$$

where, the attenuation coefficient μ is given in units $\frac{1}{\text{cm}}$.

Three main processes can occur in the interaction of photons with the target material: the photo-electrical effect, the Compton effect and pair production. In the following, the photo-electrical effect and the Compton effect will be described, as they are the dominant processes at the energy ranges used in radiotherapy.

Photo-electrical Effect

In the photo-electrical effect, the incoming photon gets completely absorbed by an inner shell electron of a target atom. If the energy of the photon is larger than the binding energy of the electron, the electron gets released from the atom, leaving a positively charged atom. The kinetic energy of the released electron E_{kin} is hence described by the difference between the photon energy E_γ and the binding energy E_{binding}:

$$E_{\text{kin}} = E_\gamma - E_{\text{binding}}\tag{2.2}$$

With increasing energy, the photo-electrical effect dominates less and the Compton effect gains in relevance.

Compton Effect

The Compton effect is dominant for photon energies around 0.01 - 100 MeV[7]. It describes the inelastic scattering of a photon at a loosely bound electron. Since the photon is not absorbed in this effect, the resulting kinetic energy of the electron is described by:

$$E_{\text{kin}} = E_\gamma - E_{\gamma'} - E_{\text{binding}}\tag{2.3}$$

$E_{\gamma'}$ describes the energy of the photon after interaction with the target atom. $E_{\gamma'}$ depends on the initial photon energy E_γ, the angle α of the scattered photon and the rest energy of the electron $E_{e_0^-}$:

$$E_{\gamma'} = \frac{E_\gamma}{1 + \frac{E_\gamma}{E_{e_0^-}} \cdot (1 - \cos\alpha)} \tag{2.4}$$

Charged Particles

When charged particles like electrons, protons and heavier ions are passing a target, their electrical field interacts elastically or inelastically with shell electrons of the target or with the coulomb field of the nuclei. Also, direct, inelastic nuclear interactions with the nucleons are possible. The stopping power of charged particles is hence the sum of the collision stopping power and the radiative stopping power. For electrons, the radiative stopping power is dominant.

The collision stopping power is given by the energy loss dE due to inelastic collisions per path length dx.

The energy loss of heavier charged particles like protons and heavier ions was initially described by Hans Bethe[8] and updated by the Particle Data Group to the following[9]:

$$-\frac{dE}{dx} = \rho 4\pi N_A r_e^2 m_e c^2 z^2 \frac{Z}{A} \frac{1}{\beta^2} \left(\frac{1}{2} \ln \left(\frac{2 m_e c^2 \beta^2 \gamma^2 W_{max}}{I^2} \right) - \beta^2 - \frac{\delta(\beta\gamma)}{2} \right) \tag{2.5}$$

$\frac{dE}{dx}$ describes the mass stopping power of the projectile, ρ is the target's density, N_A is the Avogadro's constant, r_e describes the (classical) electron radius, z is the charge number of the projectile, Z the atomic number of the target and A the atomic mass of the target. The maximum possible energy transfer to an electron in a single collision is described by W_{max}. I describes the mean excitation energy. The δ-term describes density effect corrections to the energy loss due to ionization.

The Bethe-formula (Equation 2.5) is valid if it holds for the particle's energy: $0.1 \leq \beta\gamma \leq 1000$. In case of $z = 1$ (i.e. a proton), the proton energy should be higher than 10 MeV for the energy loss to be described by the formula[9].

Dose

The interaction of charged or uncharged particles or photons with matter causes energy absorption in the material. The absorbed energy dE per unit mass dm is described as dose D:

$$D = \frac{\mathrm{d}E}{\mathrm{d}m}, \tag{2.6}$$

given in the unit Gray (Gy), which equals J/kg.

If energy is absorbed from charged particles, the energy is transferred via direct ionizations. For photons however, energy contributing to dose is transferred via secondary electrons stemming from initial ionizations caused by the photons. Therefore, depth-dose curves of photons show a strong build-up effect, as secondary electrons produced in different penetration depths are needed until the maximal dose is reached. At the point of maximal dose, a charged particle equilibrium exists, where the number of secondary electrons produced equals the number of absorbed electrons. Higher photon beam energies lead to a build-up-effect in deeper layers of the target. For ion radiation, dose is applied directly through direct ionizations from the primary beam. Hence, no build-up is visible. According to Bethe-Bloch's Formula, energy loss increases for decreasing particle velocity. Hence, most dose is delivered only when particles stop, in the so-called Bragg peak.

Physically, dose can be described as follows:

$$D = \int \mathrm{d}E\, S(E)\, \rho \Phi_E = \frac{S}{\rho} \cdot \Phi = \frac{S}{\rho} \cdot \frac{\mathrm{d}N}{\mathrm{d}A_\perp}, \tag{2.7}$$

where S describes the mass stopping power (also often referred to as $-\frac{\mathrm{d}E}{\mathrm{d}x}$), ρ is the material's density and $\frac{\mathrm{d}N}{\mathrm{d}A_\perp}$ describes the amount of particles per area perpendicular to the beam.
The physical dose depends only on the beam's energy and the absorber material. However, in biological and clinical studies, not only the target material is crucial for determining the dose. Instead, the ability of a cell or an organ to repair is taken into account as well. In addition, the same physical dose can cause large differences in cell response, depending on the beam's Linear Energy Transfer (LET) (see Section 2.1.1), leading to a measurable difference described by Relative Biological Effectiveness (RBE) (see Section 2.2.4).

Linear Energy Transfer

Ionizing radiation creates electrons around the incoming particle's track. The amount of energy loss, caused by collision, per path length can be described by the LET. Only energy transfers below a threshold energy Δ are taken into account, which occur within the range of electrons with energy Δ around the particle's track:

$$LET_\Delta = \left(\frac{dE}{dx}\right)_\Delta .$$

(2.8)

Usually, for determining the LET of a charged particle, all energies of secondary electrons are taken into account, hence $\Delta \to \infty$. Then, the LET is equal to the collision stopping power.

Typical LET values of radiation used in this thesis are shown in Table 2.1. The implications of LET on biological tissue in radiotherapy will be discussed in Section 2.2.4.

Radiation	Energy	LET_{H_2O} in keV/µm
X-ray	225 kV	1.7
e^-	30 MeV	0.27
p	224 MeV	0.42
p	35 MeV	1.65
^{12}C	400 MeV/u	10.89
^{12}C	150 Mev/u	19.47

Table 2.1: Overview on beam energies and corresponding LETs for energies used within this thesis.

2.1.2 Generation of Ionizing Radiation at Conventional and Ultra-High Dose Rates

In the course of this thesis, irradiation at high and ultra high dose rates plays a major role. In the following, the production of ionizing radiation in general and the generation of ultra-high dose rates will be explained.

For clinical relevance, radiation of any kind has to have an energy high enough to have a sufficient range inside a patient; the required penetration depths range from several mm until 30 cm. To obtain this range, X-rays or electrons of 6 - 25 MeV are used. For protons, 30 cm depth are reached when accelerating the protons up to 220 MeV and ^{12}C up to 425 MeV/u.

X-rays

X-rays suitable for clinical appliance or laboratory purpose are typically generated using a linear accelerator (Linac) in which electrons are accelerated. These electrons hit a target, usually of high atomic number Z like tungsten, where they get slowed down by the Coulomb field of the target atoms and shell electrons. During that process, bremsstrahlung is released showing a continuous energy spectrum. The

minimal emitted wavelength λ_{min} is reached when the kinetic energy E_{kin} of the electron is converted completely. Together with the acceleration voltage U, E_{kin} is given by:

$$E_{kin} = e \cdot U = h \cdot \frac{c}{\lambda_{min}} \Rightarrow \lambda_{min} = \frac{h \cdot c}{e \cdot U}. \tag{2.9}$$

Here e is the electron's charge, c the speed of light and h the Planck constant. In addition to the continuous bremsstrahlung, radiation with discrete energies can be emitted if the electrons directly ionize a target atom. This electron-"hole" is filled by an electron of a higher shell, emitting radiation with a discrecte energy.

In clinical Linacs, radiation of 6-25 MeV is used, at a dose rate of around 2 Gy/min.[10] To obtain higher dose rates, it is possible to make use of the usually cone-shaped photon beam: closer distances to the source lead to an increased dose rate, since the dose rate decreases with $1/r$, r being the distance to the source. This technique was used in Publication I and is described in detail there.

Electrons

To generate electron radiation, the same systems can be used as for generation of X-rays, but the tungsten target can be removed. Hence, the electrons are accelerated directly and can be released onto the patient. If the linear accelerator allows for changing the acceleration parameters, high dose rates of electrons can be generated also in clinical linacs by changing beam parameters like the pulse width or pulse frequency[11,12].

In this thesis, electrons of ultra-high dose rates were generated at the ELBE accelerator, Dresden[13]. ELBE is known for its supraconducting high-frequency resonators which are able to generate continuous electrical fields of up to 30 MV/m. With the resonators at ELBE, it is possible to accelerate electrons in a quasi-continuous wave mode and to generate high currents of an energy up to 40 MeV[14]. The pulse repetition rates can be set flexibly. Hence, ELBE is a very suitable accelerator for FLASH studies *in vitro*, as it allows for various currents and pulse repetition rates which allow for studying multiple dose rate setting (see Appendix A.1).

Ions in Synchrotrons and Cyclotrons

For clinical use, ions need to be accelerated to high energies of up to 220 MeV for protons and 425 MeV/u for carbon ions to ensure sufficient penetration depth of around 30 cm in a patient. These high energies are easier to generate in circular accelerators like cyclotrons and synchrotrons because the particles can pass the same acceleration modules repeatedly, gaining velocity each time they pass the acceleration modules. For heavier ions such as helium and carbon ions, synchrotrons are better suited than cyclotrons due to their larger radius being proportional to the charge-to-mass ratio q/m, which is half the size for protons).

For protons, cyclotrons are often used in clinical practice due to their compact construction compared to synchrotrons. Robust high dose rates are achievable with cyclotrons, as their beam delivery is continuous, allowing for large doses at high dose rates. Regarding high dose rate experiments, recent publication discussed the feasibility of achieving high dose rates with carbon ions in synchrotrons[15]. Here, the challenge in achieving high dose rates is the acceleration, which is done in cycles of at least 1-2 s[16]. Delivering the beam over more than one cycle would decrease the average dose rate drastically. In order to generate a high average dose rate, it is therefore necessary to extract the particles needed within one cycle. This limits the maximal achievable dose with synchrotrons under FLASH conditions. However, FLASH dose rates were recently obtained in Helium-FLASH beams from synchrotrons[17].

Laser accelerated protons
A special subgroup of proton irradiation with ultra-high dose rates is the irradiation with laser-accelerated protons. This technique became popular over the last decade as it allows for dose rates of more than 10^{11} Gy/s[18] while maintaining a very short acceleration length of a few micrometers[19]. Laser-accelerated protons are generated by a powerful laser of several PW power or higher shooting onto a solid target, typically a thin foil. In this shot, relativistic electrons are produced which create a strong plasma on the foil's surface. This causes an acceleration of protons existing on the target[20] via Target Normal Sheath Acceleration (TNSA). The energy spectrum of the particles can be sharpened quadrupol magnets or with solenoid coils with a distinct magnetic field in the order of several Tesla field strength[21]. At the DRACO laser in Dresden, Germany, up to 25 Gy per shot were available up to a dose rate of 10^9 Gy/s. This set up was applied in *in vitro* experiments in Appendix B.1.

2.2 Radiobiology

In this section, the basics of radiobiology will be described with respect to the structure of cells, the different stages of cells during the course of their cell cycle and its implication in radiotherapy. Furthermore, DeoxyriboNucleic Acid (DNA) repair mechanisms will be explained.

2.2.1 The Cell - Target of Radiation

Mammalian cells are the main target of radiotherapy. In the following, the structure of mammalian cells will be described and a schematic picture can be found in Figure 2.1: Cells are surrounded by a double-lipid layer membrane. Inside, different membranes subdivide the cell into compartments; these compartments are called
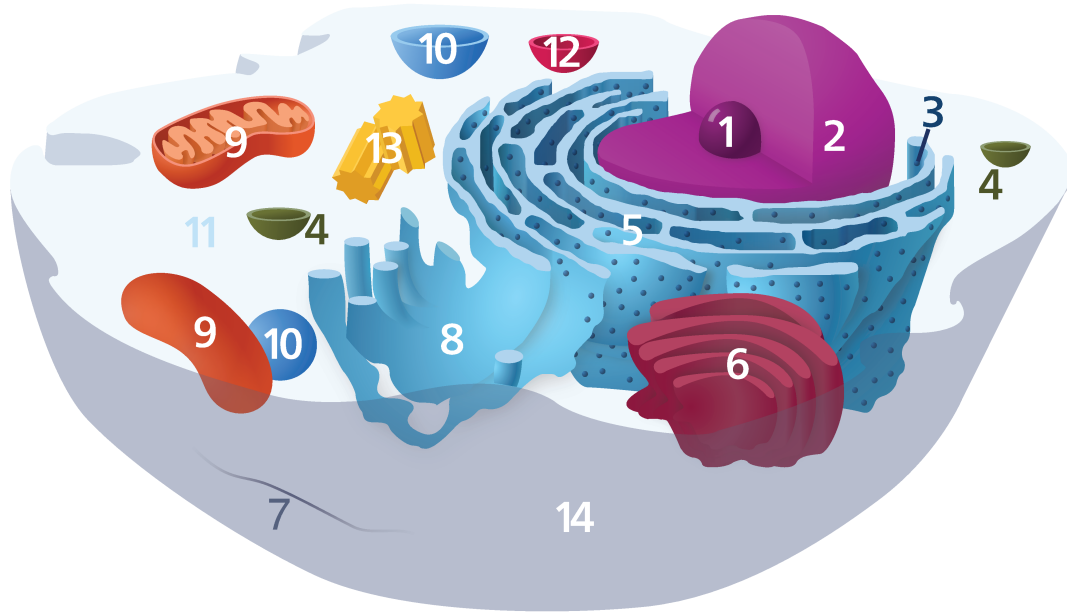
Figure 2.1: Structure of a mammalian cell. 1: Nucleolus, 2: Nucleus, 3: Ribosomes, 4: Vesicle, 5: Rough ER, 6: Golgi apparatus, 7: Cytoskeleton, 8: Smooth ER, 9: Mitochondrion, 10: Vacuole, 11: Cytosol, 12: Lysosome, 13: Centriole, 14: Cell membrane. Taken from [22]

organelles. The most important organelle for radiotherapy is the nucleus, where the DNA is located: The nucleus has a double-membrane layer which contains pores. The inside of the nucleus contains chromatin and the nucleolus: Chromatin is a combination of DNA and proteins and is the material chromosomes consist of. The nucleolus is an organelle responsible for ribosome production. On the outside of the nuclear membrane, the Endoplasmatic Reticulum (ER) is made of a continuous membrane network which can be distinguished in two types: the smooth and the rough ER. The smooth ER cisternae are mainly involved in lipid biosynthesis, which are used to produce new membranes. In contrast, the rough ER is so called due the presence of ribosomes on the outer surface. It is connected with the outer nuclear membrane and it is the site for the synthesis, folding and modification of specific proteins.

Other important organelles to mention are the mitochondrion, where adenosin triphosphate (ATP) is built. In that function, mitochondrion is the energy supplier of the cell. The peroxisome is an organelle where oxidation reaction of fatty acids and aminoacids occur. In these processes, H_2O_2 is produced, and gets transformed to H_2O via the enzyme *catalase.*
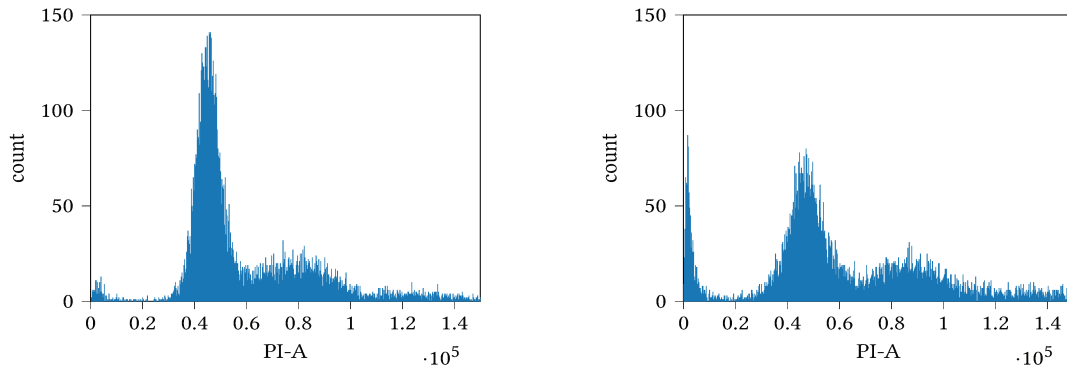
Cell Cycle

Proliferating cells go through different phases during their division cycle: After mitosis, cells enter the G1 phase, in which the cells grow in size. Organelles and enzymes that are needed for DNA synthesis are built up. During the G1-phase, the DNA only appears in one copy. After the G1 phase, the S phase begins, in which DNA is replicated. In addition, proteins are built up that are required for DNA structuring. In the G2 phase, which begins after the S phase, the cell begins to prepare for mitosis, the cell division phase. During mitosis (= M phase) the cell divides into two daughter cells. In this last phase, akk the cellular components, including the genetic material, are distributed in the newly formed cells.

The cell cycle length depends on the type of tissue and takes usually 1-2 days. Hereby, the longest cell cycle phase is G1. Hence, in a heterogeneous culture, most cells are in G1 phase (see Figure 2.2 a). In cancer cells, proliferation can take less time since the checkpoints in G1 phase tend to be deactivated[23]. Checkpoints can be activated between all phases, in order to check the integrity of the cell. In the event of errors which cannot be fixes, apoptosis can take place. In terms of radio-damage, a critical checkpoint is located in the G2 / M transition, which detects radiation-induced damage and delays the cell cycle to ensure that DNA repair occurs before the mitosis begins. Due to this checkpoint, cells "stop" in the G2/M phase after irradiation for a while depending on the extent of the damage and the cell type (see Figure 2.2 b).

DNA

Inside the cell nucleus, the chromosomes are located, which consist of a chromatin fiber. The chromatin fiber consists of DNA wrapped around histones in the nucleosomes. The building blocks of the DNA are the nucleotides, made of a base bound to a phosphate-deoxyribose-molecule. There are four types of bases: Adenine (A), Cytosine (C), Guanine (G) and Thymine (T). Hereby, A and G are called "purines" and T and C are called "pyrimidines". Via the amino group (NH), A and T form two hydrogen bonds with each other, and G and C form three (see Figure 2.3). Each of the bases is connected to a molecule of deoxyribose which is bound to a phosphate group itself. In Figure 2.3, this is symbolized by "R". Altogether, the base pairs and the phosphate-backbone form the DNA molecule, which has a width of around 2 nm.

2.2.2   DNA damage and DNA repair

(a) Cell cycle distribution, normal culture.

(b) Cell cycle distribution, after irradiation. Relative to the G1 peak, G2 became larger.

Figure 2.2: Cell cycle analysis of T24 cells using Flow Cytometry Analysis (FACS): Histogram of DNA content with typically two peaks: First peak (= one DNA replicate) indicates G1 phase. Second peak (= two DNA replica) indicates G2/M phase. The histogram entries between the two peaks indicate the S phase, where the second copy of DNA is getting synthesized. (a): normal, heterogeneous cell culture, where most cells are in G1 phase. (b) after irradiation: cells accumulate in G2/M.

DNA damage

In order to understand DNA damage caused by ionizing irradiation, different timescales have to be considered. When a cell is hit by radiation, radiation energy is absorbed in ionization or excitation events of the molecules present in the cell. In particular, when the DNA is hit directly by ionizing radiation, Single Strand Break (SSB)s or Double Strand Break (DSB)s can occur. These are damages to the sugar-phosphate backbone of the DNA molecule. Also, an indirect type of radiation damage is possible. In fact, the most abundant molecule in cells, H_2O, can be ionized or excited:

$$H_2O \xrightarrow{\gamma} H_2O^{\bullet+} + e^- \tag{2.10}$$

$$e^- + nH_2O \longrightarrow e_{aq}^- \tag{2.11}$$

$$H_2O \xrightarrow{\gamma} H_2O^* \tag{2.12}$$

$$H_2O^* \longrightarrow H^\bullet + OH^\bullet \tag{2.13}$$

$$O_2 + e_{aq}^- \longrightarrow O_2^{\bullet-} \tag{2.14}$$

These initial ionization or excitation events are assigned to the physical and physiochemical stage, which lasts typically 10^{-15} s and 10^{-12} s, respectively[24]. Thereby, excited water molecules can be generated, which subsequently undergo radiolytic
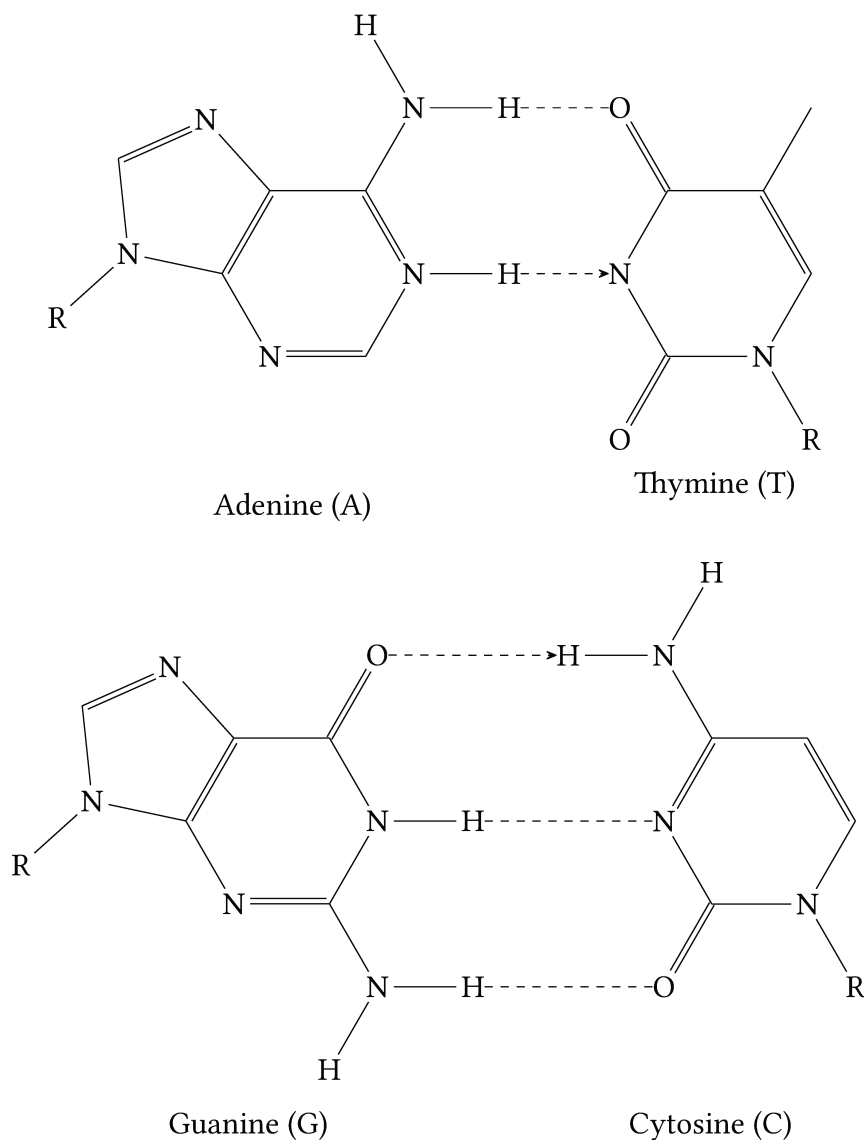
Figure 2.3: Chemical structure of the base pairs thymine-adenine and guanine-cytosine. A-T are connected via two hydrogen bonds, whereas C-G are connected via three hydrogen bonds.

processes, leading to a variety of different radicals. Further details on radiolysis of water including oxygen effects will be explained in Section 3.1.3.

The most important ROS including radicals and non-radical species causing DNA damage are $O_2^{\bullet-}$, H_2O_2, $OH^{\bullet}$ and the water-solvated electron e_{aq}^-. These radicals are built during the chemical phase which happens 10^{-12} – 10^{-6} s after irradiation starts. The chemical phase is then followed by the biological phase, which is crucial for DNA damage. The aforementioned ROS $O_2^{\bullet-}$, H_2O_2, $OH^{\bullet}$ and e_{aq}^- are usually scavenged by cell-internal scavenging systems (see Section 2.3.1) but if the scaveng-

ing systems are saturated, a condition called oxidative stress can be established. in this context, the excess of radicals can interact with the DNA itself and cause DNA damage. Hereby, OH$^\bullet$ radicals can destroy the hydrogen bonds between the DNA bases (see Figure 2.3), or a direct reaction between OH$^\bullet$ and the pyrimidines cytosine or thymine can occur. Subsequently, radicals of pyrimidine are produced which can further react with oxygen thus inducing the formation of thyminglycol (TG), a highly toxic base modification[25,26].

Furthermore, reactive oxygen species can lead to SSBs/DSBs. In this case, the desoxyribose reacts with, among other radicals, OH$^\bullet$ causing desoxyribose radicals[27]. This is most likely to happen locally in the hydrate shell of the DNA, as OH$^\bullet$ cannot diffuse far due to their high reactivity[28]. H_2O_2 instead has a longer life time and can also be damaging to the DNA, although being less reactive than OH$^\bullet$.

The deoxyribose is likely to be damaged by irradiation in a ways that O_2 is either uptaken, or released. Additionally, $O_2^{\bullet-}$ can be released and further converted to O_2 or H_2O_2 by the later mentioned mechanisms (see Section 2.3.1) involving Superoxide Dismutase (SOD) and Catalase (CAT) enzymes[29,30]. DNA damage can also be produced by the formation of peroxyl radicals (ROO$^\bullet$), stemming from lipids in the phospholipid membranes. Although not present close to the DNA, these radicals can still be harmful due to their relatively long life-times of more than $10\,s$[31,32]. R$^\bullet$ radicals react with O_2 to form ROO$^\bullet$. However, this does not apply to purine-base-derived radicals[33]. Electron holes generated by radicals on the DNA-backbone can undergo charge-transport, causing DNA-base-damage eventually[34].

Typically, X-ray radiation of $1\,Gy$ causes around 1000 SSBs and base damages but only 30-40 DSBs per cell[25]. Increasing LET leads to a higher number of DSBs[35], caused by a higher number of OH$^-$ radicals. Also, the number of DSBs as a function of dose is highly linear for doses between $1\,mGy$ and $100\,Gy$[36]. DSBs are critical for the DNA, as DSB repair is much more complex than the repair of SSBs. Therefore, DSBs are seen as the main reason for radiation induced cell death.

DNA repair

DSBs typically involve damages to both ends of the desoxyribose backbone, loss of base pairs and hence unmatching strands. For the repair of these damages, three main repair pathways are available: The Non-Homologous End Joining (NHEJ), Homologous Recombination (HR) and Microhomology-Mediated End Joining (MMEJ). NHEJ works as a rapid repair technique in which two free ends of DNA are joined and processed in order to remove damaged bases before combining the two strands into their original DNA strucure[37]. In contrast to other DNA repair mechanisms, this method is accessible in all phases of the cell cycle, providing a quick and complete repair. However, this method is error prone and can lead to mutations[38,39].

HR is present in the late S phase and the G2 phase, as it needs duplicated DNA for repairing: HR can repair DSBs by cutting the 5' ends of the damages strand[40]. The leftover, 3' end of the sister chromatid serves as a blueprint for synthezising parts of the genome nucletide sequences. HR is a lot more accurate that NHEJ, but takes longer and is not permanently present throughput cell cycle. From a DNA-damage point of view, this is the reason for a higher cell survival at late S phase and G2 phase.

MMEJ is a mechanism used as backup-repair process and is of only minor importance. MMEJ uses both DSB ends to match DNA in short sections of around 10 base pairs. The advantage of MMEJ is its speed and flexibility; however, it is error prone[41].

Cells with DSBs tend to stop their cell cycle in the G2 phase to allow for more repair time[42]. Despite all repair mechanisms, cells still tend to fail repairing all damage, leading to apoptosis and cell death.

2.2.3 Linear Quadratic Model

The effect of ionizing radiation onto *in vitro* cell culture can be measured by determining the amount of cells which survived a given amount of dose and were able to build a colony 5-10 days after irradiation. This number of colony building cells is a fraction of the initial number of cells, and is hence described by the survival fraction *SF*[43]. The most common model to describe cellular survival of *in vitro* experiments is the Linear Quadratic Model (LQM), where the survival fraction *SF* is given as a function of dose *d* by:

$$SF = e^{-\alpha d - \beta d^2} \tag{2.15}$$

with α and β as empirical parameters. Accordingly to the exponent, α is given in unit $\frac{1}{\text{Gy}}$ and β in $\frac{1}{\text{Gy}^2}$, respectively. On a logarithmic scale, the α-term leads to a linear shape and the β-term to a quadratic shape. The LQM has an empirical basis, i.e. the meaning of the parameters α and β are not derived from any other theory. However, various studies have shown, that the α-term correlates with single-strand-breaks of the DNA and the β-term correlates with double-strand-breaks. Additionally, the $\frac{\alpha}{\beta}$ ratio depends on many factors such as radiation type (LET), oxygenation status of the cells, dose rate[44], temperature and cell cycle phase. However, it is not possible to fully parameterize these effects into the LQM[45]. Figure 2.4 shows exemplarily two survival curves with different $\frac{\alpha}{\beta}$ ratios. The LQM is only valid for doses up to ~10 Gy; for doses exceeding this level, the LQM systematically underestimates the survival.
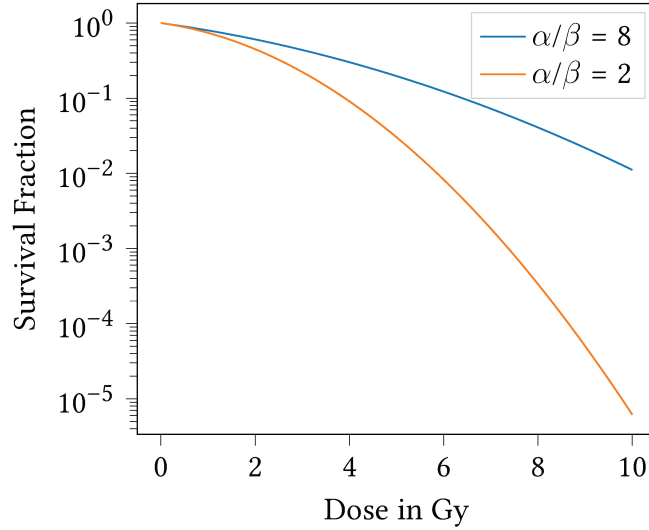
Figure 2.4: LQM for different α/β values. A high α/β value either indicate a stronger repair capability of the cells, or less damage at similar doses due to low-LET radiation, hypoxia, or other causes.

2.2.4   Relative Biological Effectiveness

The effect of radiation on cells is strongly influenced by the beam's LET. This is due to complex changes in radical production depending on LET (see Section 3.1.3 and 3.1.2) and hence complex changes in DNA damage. To quantify this effect on a cell survival level following the LQM, the quantity of RBE has been defined. Typically, low-LET radiation is used for reference, like 250 kV X-rays or ^{60}Co-γ-rays with 1.17-1.33 MeV. RBE is then defined as the ratio between the doses d that are needed for the reference radiation and the radiation of interest to reach the same survival fraction SF in a cell culture (see Equation 2.2.4).

Since α and β are the only free parameters in the LQM, they depend empirically on the type of irradiation. In the stated formula, the index γ describes the dependence of α and β on photon radiation whereas *ir* represents the dependence on the radiation of interest.

$$RBE(SF) = \frac{d_\gamma(SF)}{d_{ir}(SF)} = \frac{\sqrt{\alpha_\gamma^2 - 4\beta_\gamma \ln SF} - \alpha_\gamma}{\sqrt{\alpha_{ir}^2 - 4\beta_{ir} \ln SF} - \alpha_{ir}} \cdot \frac{\beta_{ir}}{\beta_\gamma} \tag{2.16}$$

An interesting aspect of RBE is its dependence on LET: RBE increases with LET, peaks around 100-200 keV/μm and decreases for higher LET. This phenomenon is referred to as "overkill-effect".

2.2.5 Oxygen Enhancement Ratio

The level of molecular oxygen (i.e. O_2) in cells affects directly the cells' radio-sensitivity, leading to increased survival for decreased O_2-levels. Phenomenologically, this effect can be described by the Oxygen Enhancement Ratio (OER), which is defined as the ratio of the doses *d* needed for two different *in vitro* cell cultures with different oxygen levels $p(O_2)$ to reach the same biological endpoint (e.g. survival fraction *SF*). As a derivation from the LQM, the OER can be described as[46]:

$$OER(SF) = \frac{d(p(O_2), SF)}{d(SF)} = \frac{\sqrt{\alpha^2(p(O_2)) - 4\beta(p(O_2))\ln SF} - \alpha(p(O_2))}{\sqrt{\alpha^2 - 4\beta \ln SF} - \alpha} \cdot \frac{\beta}{\beta(p(O_2))} \tag{2.17}$$

The reason for this observed difference is most likely a combination of altered DNA-repair mechanisms in hypoxia, but also a changed production of radiation-induced radicals in the cytoplasm: DNA-damaging radicals are produced during radiolysis and their abundance is highly dependent on oxygen levels (see Section 3.1.3). Interestingly, the OER is also highly LET dependent: For low LET radiation and $p(O_2) = 0$, the OER is around 2.7, whereas it reaches a value of 1 for high LET radiation[47]. It is known from simulation studies of radiolysis in water, that the beam's LET has a high impact on radical production, leading to less O_2 dependent radical production for higher LETs[48]. This implies, that the observed differences in OER as a function of LET are mostly of radiolytic nature.

Another approach to describe the OER was given by Alper and Howard-Flanders in 1956, where they described the oxygen-dependent radio-sensitivity in photon radiation with the shape of a Michaelis-Menten-kinetic[49]:

$$\frac{SF}{SF_H} = \frac{m \cdot p(O_2) + K}{p(O_2) + K} \tag{2.18}$$

where *SF* indicates the survival fraction under normoxic conditions, SF_H is the survival fraction in complete hypoxia (i.e. $p(O_2) = 0\,\%$) and $p(O_2)$ again the oxygen percentage. *K* and *m* are constants. *m* was observed to fit well with a value of around 2.7 which can be interpreted nowadays as the maximum OER value possible.

2.3 Oxygen - Its Role in Tumor Cells and Hypoxia as a Special Case

Besides oxygen acting as a radio-sensitizer, it plays a critical role in cellular respiration, in which glucose ($C_6H_{12}O_6$) gets oxidized to carbon dioxide (CO_2) and oxygen (O_2) gets reduced to water (H_2O), via glycolysis and the citric acid cycle. The brutto

equation for the amount of oxygen being consumed is given by:

$$C_6H_{12}O_6 + 6\,O_2 \longrightarrow 6\,CO_2 + 6\,H_2O + \text{Energy} \qquad (2.19)$$
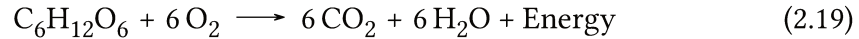
The produced energy is then used for the synthesis of Adenosine Triphosphate (ATP), a molecule which is highly involved in many energy-using cellular processes. If not enough oxygen is available in the cells, anaerobic cellular respiration becomes more dominant, leading to lactic acid as end product.

In physiological oxygen conditions, the so-called *physoxia*, the oxygen partial pressure lays between 3 % and 7.4 %[50], depending on the tissue type. Lung alveoli cells show higher levels of oxygen of around 13.5 %, due to their direct exposure to air with 21 % O_2. In *in vitro* experiments, a level of 21 % O_2 is referred to as *normoxic*. In both *in vivo* and *in vitro* experiments, a level below 3 % O_2 is called *hypoxia*[50].

Hypoxic regions within a tumor can occur due to increased cell proliferation and a simultaneously reduced vascular architecture, which leads to an under-supply of oxygen[51]. Hereby, a distinction is made in acute and chronic hypoxia. Chronic hypoxia occurs in tumors, if the diffusion of oxygen is limited and it can last several hours up to days[52,53]. In contrast, acute hypoxia is a shorter, more temporal state[54]. As stated above, the absence of oxygen has a high impact on the cells' ability to generate ATP, as it forces the cell into anaerobic metabolic processes. In cancer cells, it was observed that the cellular metabolism is mainly anaerobic, even if enough oxygen is available to provide aerobic respiration. This effect is referred to as Warburg-effect, named after Otto Warburg, who describes this phenomenon for the first time in 1920. He called the observed effect "aerobic glycolysis". Cells in this state have a highly inefficient energy metabolism, leading to the typically observed enlarged glucose metabolism of cancer cells[55]. Since glycolysis-related substances like pyruvate or lactate are also present in radical scavenging processes, cancer cells show different radio-response already based on their metabolism[56].

On a genetic and functional level, cellular response to hypoxia is coordinated via activation of the transcription factor Hypoxia-inducible Factor 1 (HIF1), encoded by the corresponding gene HIF1. An upregulation of HIF1 causes upregulation of several other genes responsible for increased survival under hypoxic conditions. Genes affected by hypoxia are, first of all, genes involved in metabolic pathways but also in DNA repair pathways such as HR and NHEJ[57]. Hence, the understanding of the hypoxic state of cells is of critical importance as hypoxic cells behave systematically different under irradiation when compared to their normoxic counterparts, leading to a highly increased radio-resistance by a factor of 2-3 (see Section 2.2.5).

## 2.3.1 ROS Abundance and Cellular ROS Scavenging Systems

For the understanding of oxygen-related cellular processes leading to altered radioresponse, the following section will cover the role of ROS. ROS, from a chemical point of view, are highly reactive species stemming from O_2, like superoxide ($O_2^{\bullet-}$), peroxides (R_2O_2), hydroperoxyl (HO_2), hydroxyl ($OH^{\bullet}$) or singlet oxygen (O_2 at lowest excited state, with all electrons being spin paired).

ROS can be generated by various reactions, e.g. as byproducts of cellular metabolic mechanisms, or through radiolysis of the cytoplasmic water (see Section 3.1.3). Due to ROS' high reactivity, they can cause macromolecular damages being harmful to cells. Therefore, cells have various ROS scavenging systems to protect themselves. In the following, the production and elimination of two important ROS, superoxide ($O_2^{\bullet-}$) and hydrogenperoxide (H_2O_2) will be described. $O_2^{\bullet-}$ is formed due to the reaction of O_2 with another electron. O_2 comes naturally with two unpaired electrons, leaving the superoxide $O_2^{\bullet-}$ with one unpaired electron and negative net charge (see Equation 2.20). In cells, superoxide is processed to O_2 and H_2O_2 through dismutation via the SOD-enzyme (see Equation 2.21).

$$e_{aq}^- + O_2 \longrightarrow O_2^{\bullet-} \tag{2.20}$$

$$2\,O_2^{\bullet-} + 2\,H^+ \xrightarrow{\text{SOD}} H_2O_2 + O_2 \tag{2.21}$$
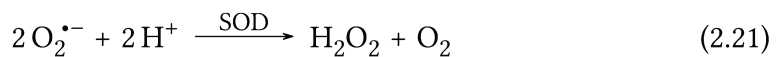
Hereby, three kinds of SOD exist in eukaryotic cells, each of the SOD enzymes being able to bind to a metal co-factor: Cu,ZnSOD (encoded by the gene SOD1), MnSOD (encoded by SOD2) and extracellular Cu,ZnSOD (SOD3)[58]. Cu,ZnSOD is located in the cytosol, whereas MnSOD is located in mitochondria and peroxisomes. However, Cu,ZnSOD can also relocate into the nucleus[59].

Since the produced H_2O_2 is highly toxic to cells, H_2O_2 is then further processed via either CAT or by means of Glutathione (GSH) via Glutathione Peroxidase (GPX) enzymes to H_2O and O_2:

$$2\,H_2O_2 \xrightarrow{\text{CAT}} O_2 + 2\,H_2O \tag{2.22}$$

$$2\,GSH + H_2O_2 \xrightarrow{\text{GPX}} GSSG + 2\,H_2O \tag{2.23}$$
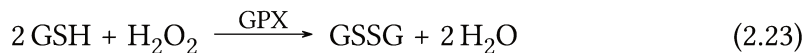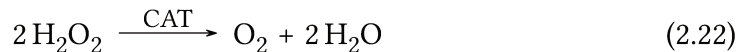
In humans, CAT consists of 4 sub-units, each containing a hem-group and a NADPH binding site[60]. CAT is one of the fastest enzymes present.

GPX are a family of enzymes with the ability to reduce hydroperoxides (i.e. molecules of the form $ROOR^{\bullet}$) in general, but also H_2O_2 as a special case. It is hence not as specific as CAT regarding H_2O_2 reduction to water.

The radical and antioxidant scavenging enzymes CAT, SOD and GPX play a crucial role in cells' ROS defense.

State of the Art: Oxygen in Radiotherapy and FLASH-RT

3.1   FLASH Radiotherapy - A New Treatment

In radiotherapy, in general, the aim is to irradiate a tumor to kill cancerous cells or to induce arrest of cell division. These treatments are done by either using photon, electron, proton or heavier ion radiation, including a usually fractionated radiation scheme of around 2 Gy applied per fraction and the dose being delivered at a rate of around 0.05-0.40 Gy/s[61]. These treatment plans are typically optimized in order to achieve maximal tumor control probability while simultaneously keeping healthy tissue complications as low as possible.

In 1966, first experiments were conducted at high dose rates. Hereby, it was unexpectedly found, that mice showed less killing when irradiated with X-rays at high dose rates of 500 Gy/min[62]. In 2014, Favaudon et al. established the technique of irradiating at high dose rates (= FLASH irradiation) on lung cancer tissue using 15 Gy of very high pulse dose rates of 10^6 - 10^7 Gy/s and average dose rate of around 40 Gy/s using electron beams[63]. Interestingly, it could be observed that FLASH radiation increased the survival of healthy tissue but gave similar tumor control results, when compared to conventional radiotherapy. This behavior of protecting the healthy tissue has been since referred to as "FLASH effect". This FLASH effect was also observed in other animal irradiation, for example in minipigs[64], zebrafish

embryos[65] and lately even in humans[66].

From the findings so far, it can be conducted, that FLASH radiotherapy has the potential to open the therapeutic window as it increases the differential effect of radiation onto healthy and cancerous tissue. Therefore, FLASH radiotherapy has been intensively investigated during the last years. However, the underlying mechanisms for the FLASH effect are not entirely understood yet. So far, it is known, that FLASH-effects are highly oxygen-dependent in both *in vivo* and cell culture experiments. It has been observed that cells with high O_2 levels, i.e. 21 % O_2, showed almost no altered response between FLASH and conventional radiotherapy. The same applies to cells with anoxia, i.e. 0 % O_2. In both cases, FLASH and conventional radiotherapy lead to the same response[67]. Only for an intermediate range of low, but not too low O_2, FLASH irradiation seemed to make a difference[68]. *In-vivo*, it was shown that FLASH effects in mice treatment vanished when mice breathed carbogen[69], supporting that FLASH effects only occur at lower O_2 levels.

From these studies, it is clear, that oxygen plays a role in FLASH radiotherapy, which leads to two prominent hypotheses:

1. Oxygen depletion in irradiated volume, causing a radiation induced hypoxia (see Section 3.1.1)

2. Biological differences within the targeted, either caused by radiation itself via different ROS levels being produced, or as response to ROS (see Section 3.1.4)

In addition, recent studies mention the self-annihilation of radicals as a reason of FLASH mechanisms[61]. In this thesis, this aspect will be treated as part of in-depth radiolysis studies in Section 3.1.3. Current research focus on the delivery of beams at high dose rates, the dosimetry, and the biochemical mechanisms as well as immune-response involved in the FLASH effect[70]

3.1.1 Oxygen Depletion Hypothesis

The oxygen depletion hypothesis was one of the dominant theories of the past years to explain FLASH effects. It focuses around the idea that in general, ionizing radiation in water or cytoplasm causes radiolysis and subsequently a reduction of O_2 molecules leading to a radiation-induced decrease of O_2. At higher dose rates, it was postulated that more O_2 gets depleted[71], causing an hypoxic environment. In combination with the well-known radio-resistance of hypoxic tissue as part of the OER (see Section 2.2.5), FLASH radiation could cause the same tissue reaction as hypoxia. Since most tumors are hypoxic (see Section 2.3), FLASH radiation would not have any impact on the oxygen level present. However, in healthy tissue, FLASH

radiation would cause a local hypoxia protecting the health tissue from radiation damage. The oxygen depletion hypothesis was the basis hypothesis to be tested in Publication I, hence the following sections describe both the radiolytic FLASH components as well as the biochemical contributions in detail.

3.1.2 Physical FLASH Mechanisms: A Closer Look Into Radiolysis of H_2O

In order to understand the biological effect of FLASH, the differences between FLASH and conventional radiotherapy with regard to the formation of radicals must be examined more closely. In the simplest case, the radiolysis, i.e. the process of water molecules getting ionized due to ionizing irradiation, can be described. In that process, and especially under the presence of O_2 solved in the water, many radicals are produced (see Section 3.1.3). In cells, the same process happens in the cytoplasm, and the radicals produced there are responsible for DNA damage, when they diffuse to the DNA and react with the backbone or the bases itself (see Section 2.2.2).
Hence, the production of radicals is a critical aspect in understanding the effect of dose rate in radiation. For simplification and cells being mostly constituted of water, only the production of radicals in water will be described here.

3.1.3 Radiolysis

In both FLASH and conventional radiotherapy, the production of radicals due to radiolysis plays a critical role, as radicals are the main cause of cellular (DNA-) damage. In addition to the reactions which were already mentioned in Section 2.2.2, this section will give a detailed overview on radiolytic processes and their role in FLASH radiation.
The processes following radiation impact on water can be subdivided in four timescales: The physical, the physio-chemical, the chemical and the biological timescale. After the physical and physio-chemical stage, which lasts typically 10^{-15} s and 10^{-12} s respectively, many initial radicals due to ionization of H_2O have been produced, like e_{aq}^-, $H^\bullet$, $OH^\bullet$, H_3O^+ or $HO_2^\bullet$. These initially produced radicals can then undergo a variety of reactions with H_2O molecules, O_2 present in water, or the radicals itself. These processes take place during the chemical phase, which ends around 10^{-6} s after the radiation. An overview on possible reactions in the chemical phase are shown in Table 3.1. In that, k represents the reaction velocity. The number of radicals produced as well as the following reactions between the radicals depends directly on energy and LET of the incoming radiation. It is described by the *G*-value, which represents the number of molecules produced per 100 eV energy deposited by radiation. Hence, for each radical species produced due to radiolysis, a *G*-value can be defined.

Number	Educts	Products	k in $10^{10} \frac{dm^3}{mol\ s}$
a)	$e_{aq}^- + e_{aq}^- + H_2O + H_2O$	$\longrightarrow H_2 + OH^- + OH^-$	0.55
b)	$e_{aq}^- + H^\bullet + H_2O$	$\longrightarrow H_2 + OH^-$	2.5
c)	$e_{aq}^- + H_3O^+$	$\longrightarrow H^\bullet + H_2O$	1.7
d)	$e_{aq}^- + H_2O_2$	$\longrightarrow OH^\bullet + OH^-$	1.0
e)	$e_{aq}^- + O_2$	$\longrightarrow O_2^{\bullet-}$	1.9
f)	$e_{aq}^- + HO_2^\bullet$	$\longrightarrow HO_2^-$	2.0
g)	$e_{aq}^- + O_2^{\bullet-}$	$\longrightarrow OH^- + HO_2^-$	1.3
h)	$H^\bullet + H^\bullet$	$\longrightarrow H_2$	1.0
i)	$H^\bullet + H_2O_2$	$\longrightarrow OH^\bullet + H_2O$	0.01
j)	$H^\bullet + OH^-$	$\longrightarrow e_{aq}^- + H_2O$	0.002
k)	$H^\bullet + O_2$	$\longrightarrow HO_2^\bullet$	2.0
l)	$H^\bullet + HO_2^\bullet$	$\longrightarrow H_2O_2$	2.0
m)	$H^\bullet + O_2^{\bullet-}$	$\longrightarrow HO_2^-$	2.0
n)	$OH^\bullet + OH^\bullet$	$\longrightarrow H_2O_2$	0.6
o)	$OH^\bullet + e_{aq}^-$	$\longrightarrow OH^-$	2.2
p)	$OH^\bullet + H^\bullet$	$\longrightarrow H_2O$	2.0
q)	$OH^\bullet + H_2$	$\longrightarrow H^\bullet + H_2O$	0.0045
r)	$OH^\bullet + H_2O_2$	$\longrightarrow HO_2^\bullet + H_2O$	0.0023
s)	$OH^\bullet + HO_2^\bullet$	$\longrightarrow O_2$	1.0
t)	$OH^\bullet + O_2^{\bullet-}$	$\longrightarrow O_2 + OH^-$	0.9
u)	$OH^\bullet + HO_2^-$	$\longrightarrow HO_2^\bullet + OH^-$	0.5
v)	$H_3O^+ + OH^-$	$\longrightarrow H_2O + H_2O$	10
w)	$H_3O^+ + O_2^{\bullet-}$	$\longrightarrow HO_2^\bullet$	3
x)	$H_3O^+ + HO_2^-$	$\longrightarrow H_2O_2$	2.0
y)	$HO_2^\bullet + HO_2^\bullet$	$\longrightarrow H_2O_2 + O_2$	0.000076
z)	$HO_2^\bullet + O_2^{\bullet-}$	$\longrightarrow O_2 + HO_2^-$	0.0085

Table 3.1: Overview on radiolytic processes in the physio-chemical stage. Reprinted from Boscolo et al.[48].

When considering the case of water mixed with O_2, the presence of O_2 has also a direct influence on the production of oxygen-related radicals, as shown in Figure 3.1.

For having a closer look into the oxygen depletion hypothesis as a cause for biological FLASH effects, the *G*-values play a crucial role in calculating the expected number of oxygen molecules produced or depleted in the (physio-)chemical stage. In detail, the *G*-values of radicals present in reactions producing or consuming oxy-
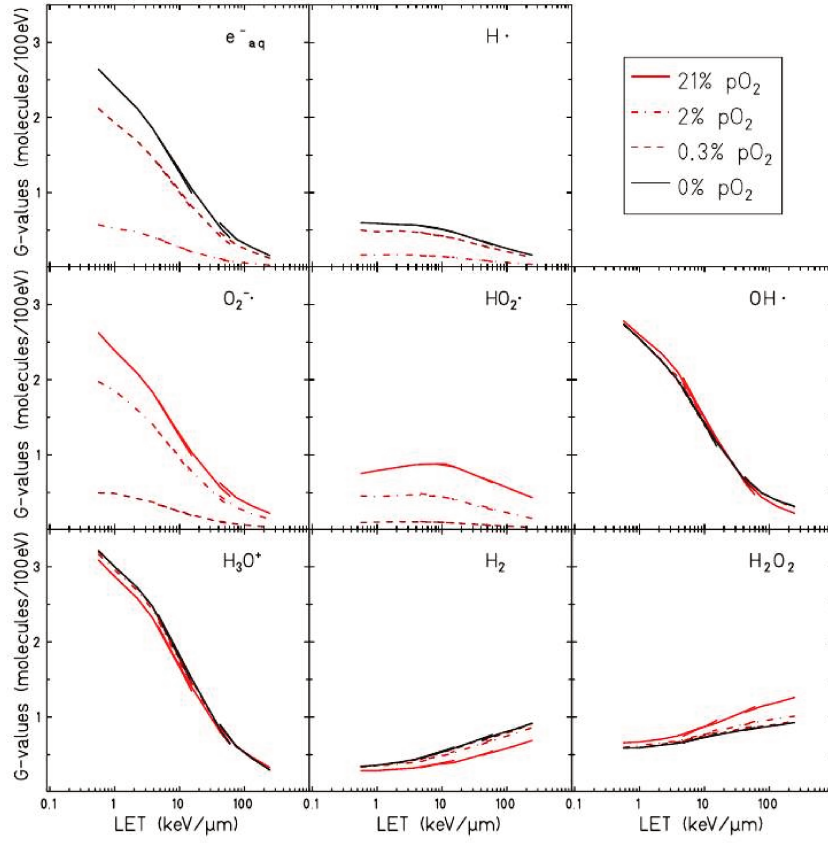
Figure 3.1: Overview of radicals produced due to radiolysis of H_2O, dependent on the LET of the incoming radiation. G-values are calculated using TRAXChem and the values cacluated for $1\,\mu s$ after irradiation are depicted. Figure reprinted from Boscolo et al.[48].

gen are of greater importance, as seen in Table 3.1. In this table, lines s), t) and z) show O_2 producing reactions and e) and k) show O_2 consuming reactions. In total, more O_2 is consumed than produced. With the help of G-values, the amount of depleted O_2 during radiation can be calculated (Equation 3.1). $c_{O_2}(D)$ describes the O_2-concentration as a function of dose D. The integral can be approximated by the sum over the amount of molecules produced per dose unit D_i with $N \cdot D_i = D$.

$$c_{O_2}(D) = c_{O_2}(D = 0) - \int_0^D G\,dD' \approx c_{O_2}(D = 0) - \sum_{i=1}^N G \cdot D_i \qquad (3.1)$$

A depiction of G-values as function of oxygen for consuming, producing and netto O_2 processes can be found in Figure 3.2 (a). The obtained G-values were fitted using a Michaelis-Menten-fit (Equation A.1). The representation of oxygen depletion as a function of dose rate can be done by replacing D by $\dot{D} \cdot t$ in Equation 3.1, which gives
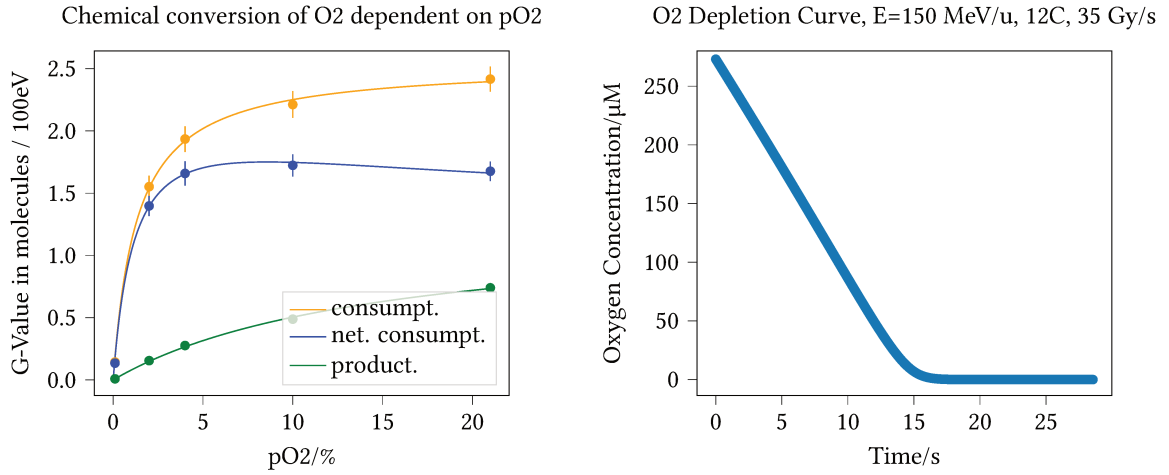
(a) *G*-values for O_2 consumption and production of as a function of O_2.

(b) Iterative determination of O_2 concentration as function of radiation time.

Figure 3.2: $G(O_2)$ for ^{12}C ions with 150 MeV/u at 1 μs after radiation. Simulation done using TRAXChem MC simulation[72]. Figure reprinted[73].

a time- and dose-rate dependent depletion of oxygen concentration. An application of Equation 3.1 can be found in Figure 3.2 (b). Here, the *G*-value for O_2 is exemplarily calculated for 1 μs after irradiation of a water sample with 150 MeV ^{12}C ions, as they were used in Publication I. Figure 3.2 was part of a master thesis supervised by me. A study of calculated oxygen depletion that was also performed by Boscolo et al.[74]. In the equation and calculations above, the amount of radicals produced per dose (i.e. the *G*-value) itself is independent from the dose rate. Following this theory, the dose rate would have no impact on the depletion of oxygen. In contrast, other theories postulate an increased oxygen depletion at irradiation with high dose rates[75,76].

Following Labarbe et al.[77], even a decrease of radicals being produced was postulated. Since this interpretation was also drawn in Publication I, it will be described in detail here: His work centered around the production of peroxyl (ROO$^\bullet$) radicals, which are known to play an important role in DNA damage. Hence, cell effects can be linked with the concentration of radicals:

$$celleffects = \int_0^T [\text{ROO}^\bullet](t)\mathrm{d}t \tag{3.2}$$

The production rate R of radicals is proportional to the dose rate $\frac{\mathrm{d}D}{\mathrm{d}t}$:

$$R(t) = \rho \cdot G(t) \cdot \frac{\mathrm{d}D}{\mathrm{d}t} \tag{3.3}$$

Normalized amount of cell effects (i.e. being between 0 % and 100 %) "area under the curve" (*AUC*) depends on the dose rate in a square-root-dependence as found by Mihaljevic et al.[78]:

$$AUC_{norm}\left(D, \frac{\mathrm{d}D}{\mathrm{d}t}\right) = a(D) + b(D) \cdot \left(\frac{\mathrm{d}D}{\mathrm{d}t}\right)^{-0.5} \tag{3.4}$$

Regarding ROO$^{\bullet}$ radicals, it was hence postulated that higher dose rates could cause less radicals due to radical-radical-recombination and hence chain termination.

In Publication I, this approach of Labarbe and Mihaljevic was used directly for the determination of the amount of O_2 depleted per dose, as it was assumed that radicals responsible for O_2 depletion can self-interact before reacting with O_2. Equation 3.4 implies that oxygen depletion does not occur linearly with dose, but follows a square-root shape. Hence, less O_2 was expected to be depleted at higher dose rates. However, Wardman[79] stated that the radiation doses are most likely not high enough to create such dense tracks that there is an overlap of radicals originating from two individual particles. Also, it is postulated that the radiation chemistry in terms of *G*-values remains similar when comparing FLASH and conventional dose rate on timescales of around 1 µs after irradiation suggesting that for chemical kinetic calculations, known *G*-values at 1 µs could be used.

Impact of beam structure

In addition to open questions regarding radiolysis' contribution to the FLASH effect, it is known that also the beam structure influences the FLASH effects[10]. Following experimental results, it is known that FLASH effects are observed if the dose rate is above 40 Gy/s and they are maximal for dose rates around 100 Gy/s[80]. However, for pulsed beams, it is not clear, which role the interplay of pulse dose rate and average dose rates has with respect to radical production. Exemplarily, in biological samples, the impact of pulse dose rate and beam structure was reported in micronuclei induction in human blood lymphocyte[81]. These pulse dose rate effects will be further addressed in Appendix A.1 and B.1.

3.1.4 Biological FLASH Mechanisms

From a biological point of view, a FLASH effect is visible in two ways: First, *in vivo*, when irradiated at high dose rates, tumor tissue reacts similarly compared to conventional radiotherapy, but healthy tissue is more spared. Hence, the therapeutic window gets broader due to an increased differential effect between tumor and

cancerous tissue. Second, *in vitro*, cancer cells also show increased survival after high-dose rate irradiation compared to conventional irradiation[68]. For both effects, the Dose Modifying Factor (DMF), can be determined, i.e. the factor in dose needed to obtain the same biological result with FLASH and with conventional radiation and lays around 1.4 - 1.8 *in vivo*[69,77,82] and is potentially lower *in vitro*[83].

It is not clear yet, if both FLASH effects stem from the same underlying mechanism, or if it is, in fact, two separate mechanisms.

To explain the *in vivo* FLASH effect, different aspects could play a role: One assumption would be that healthy tissue and cancerous tissue show significantly different levels of enzymes scavenging radicals induced by radiation. It is known, for example, that cancer tissue has higher levels of SOD which converts $O_2^{-\bullet}$ to H_2O_2 (see Section 2.3.1) leading to potentially altered radiochemical yields. Another cause could be the immune system reacting differently towards healthy and cancerous tissue via lower levels of the immune-modulating factor TGF-β, as observed in mice[63]. In sum, *in vivo*, either intrinsic differences between healthy and tumor tissue play a role, or the reaction of the immune system.

In vitro, immune cells and the micro-environment of a tumor cannot play a role. However, a decrease in TGF-β after FLASH irradiation was also shown in an *in vitro* study using proton FLASH on human lung fibroblasts[84] implying a potentially decreased inflammatory response after radiation.

Many studies stress the importance of phospholipid damage[77] as a cause of chain propagations through peroxyl radicals which then subsequently damage the DNA directly (see Section 2.2.2). It is an open question currently, whether these reactions play a role in FLASH as their reaction equilibrium could be disturbed by higher dose rates[61].

The presence of a FLASH effect *in vitro*, onto the same cells, would imply that either repair mechanisms are triggered differently[85] or that the difference between FLASH and conventional radiation is earlier, i.e. not only on a biological level, but already on physical and chemical timescales. In that cases, FLASH effects can also be studied in water alone, on a radiochemical level, as done in Publication I presented in this thesis.

Publications

This thesis is written in cumulative format according to the regulations of the Faculty of Physics and Astronomy of Ruprecht-Karls-University Heidelberg. Three peer reviewed publications, which are published in international journals, are presented in this thesis. They will be referred to as Publication I, II and III. All of the publications were conducted during my PhD project and have not been presented in other theses. I am first author of Publication I and II, the latter being a shared first authorship. I contributed to Publication III as a co-author. Detailed descriptions of author contributions are given in the overview preceding each publication. In addition to the published papers, further and ongoing research is presented in Appendices A.1, B.1 and B.2, with B being abstracts accepted at FRPT conference 2021.

Overview of Publications

This section provides an overview of the publications presented in this thesis and places them into the scientific context. A graphical overview is shown in Figure 4.1.

Publication I: Radiochemcial oxygen effects
Measurement of oxygen depletion in water during radiation at various dose rates.
Less oxygen is depleted at higher dose rates.

Publication II: Genetic oxygen effects
Oxygen effects in gene expression patterns in 4 cell lines for hypoxia and normoxia after 6 Gy photon radiation.
Supression of cell line features successful using self-developed analysis pathways.
Immune-response genes show switching behavior after 6Gy depnending on O_2.

Appendix A: Impact of beam pulse structure on oxygen depletion
Radical production strongly depends on beam pulse structure

Appendix B.1: Oxygen measurements in biological samples
Feasibility study in zebrafish embryos

Appendix B.2: Cell survival studies in FLASH radiation under O2 monitoring
FLASH effect measurable in normoxia

Publication III: Mechanistic oxygen effects
FeL and CuL compounds in glioma mimic for Superoxide Dismutase and reduces invasion
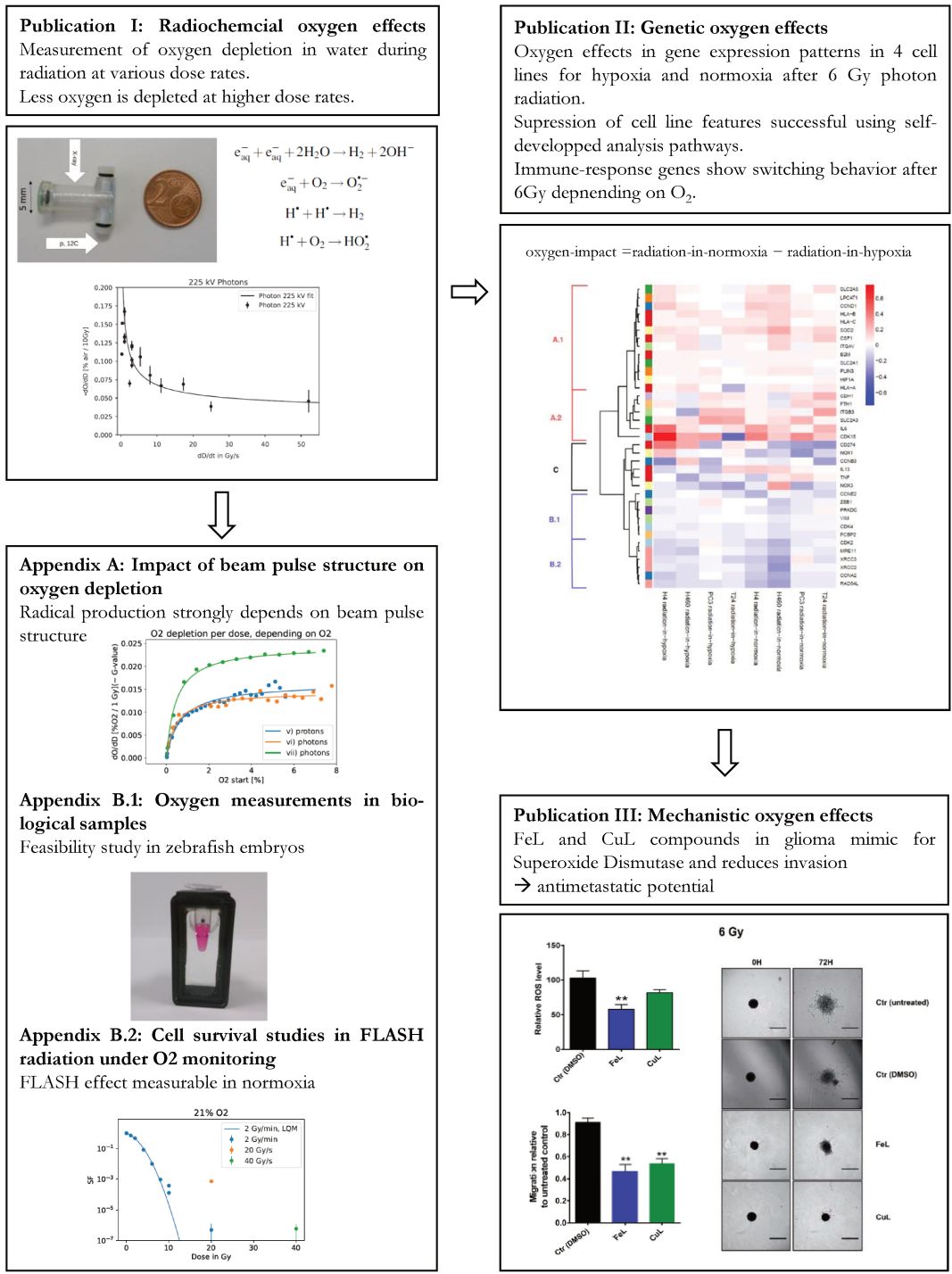→ antimetastatic potential

Figure 4.1: Overview of the thematic aspects presented in this thesis and their linkage.

It is well known that oxygen plays a major role in radiotherapy, on physical, chemical, and biological level. The three publications presented in this thesis show oxygen effects in radiotherapy on three levels: (i) On a radiochemical level conducted in water studies in Publication I, (ii) on a genetic level in various cancer cell lines under hypoxic and normoxic conditions after photon irradiation in Publication II and (iii) on an enzymatic, mechanistic level, where oxygen-related scavenging systems were actively modified by chemical compounds and their effect was tested in radiation treatment in Publication III. In addition, the impact of pulse structure on oxygen depletion was investigated (Appendix A.1), and the feasibility of oxygen measurements in zebrafish-embryos was tested (Appendix B.1). Furthermore, cell survival studies were conducted under close oxygen monitoring in FLASH radiation conditions (Appendix B.2).

Radiochemical oxygen effects

As an important prerequisite for further investigations, a measurement technique was developed to access the amount of oxygen present in water. Since water makes up for about 70-80 % of the cells' cytoplasm, measurements of oxygen in water during radiation can already hint towards processes that can also happen in the cytoplasm. For these oxygen measurements in water, a plastic phantom including an oxygen sensor was designed and irradiated with photons, protons and carbon ions (Publication I). In this paper, the main idea was to investigate whether the oxygen depletion hypothesis (see Section 3.1.1) could actually play a role in the FLASH mechanism. At first, the effect of different irradiation volumes on oxygen depletion was tested but no differences were found. In addition, an important result was, that oxygen was depleted almost continually during irradiation, in contrast to what most hypotheses postulated[71]. Oxygen was depleted during FLASH radiation, but not enough to explain the FLASH affect by radiation induced hypoxia alone, especially since less oxygen was depleted at higher dose rates. The study was able to successfully measure oxygen levels and oxygen depletion in water on-line, but more research needs to be done on what this means at the tissue level. In Appendix B.1, first trials with a measurement technique of oxygen measurements in living tissue such as zebra fish embryos were performed, leading to a successful on-line measurement of oxygen depletion also in biological environment under FLASH conditions. In addition, the effect of pulse structure of the radiation beam on oxygen depletion has not been understood yet (see Section 3.1.3). Therefore, in Appendix A.1, oxygen depletion at different dose rates and applying different beam pulse structures was tested.

From the findings of Publication I and Appendix A.1, it is clear, that the amount of oxygen measured after irradiation gives a hint towards the amount of radicals produced during radiation, since O_2 vanished due to radiolytic reactions.

Genetic oxygen effects

In order to investigate the impact of oxygen during irradiation on a genetic level (Publication II), the genetic fingerprint of four cancer cell lines in normoxic and hypoxic conditions was analyzed, with and without irradiation. A novel analysis method was developed in the study to detangle the usually intertwined effects of radiation and hypoxia. The method was applied on the gene expression data sets of the following cell lines: Non-small-cell lung cancer (H460), brain neuroglioma (H4), urinary bladder carcinoma (T24) and prostate adenocarcinoma (PC3). For each cell line, one cell set was kept at normoxic and one at hypoxic (0.3 % O_2) conditions in order to ensure a change in metabolism towards chronic hypoxia (see Section 2.3) prior to radiation with X-rays, at a dose of 6 Gy. Three days after irradiation, when most repair processes are completed, the cell pellets were obtained and a gene analysis was performed.

Since usually the cell line dependent gene expression patterns are significantly stronger than the change caused by radiation or hypoxia, a suppression of cell line dependencies was successfully implemented in the novel analysis method. This was validated by a Principal Component Analysis (PCA), an analysis method which searches for largest variance within the data set and performs a coordinate transformation onto the components with the largest variance. In this way, data showing similarities are clustered together. Furthermore, a hierarchical cluster analysis was applied, which clusters a set of objects based on mathematical similarities, leading to the assignment of similar objects to the same group. In contrast to a PCA, it does not transform the data into another coordinate system. After removing cell line dependent features from the datasets, especially the genes involved in inflammation and oxidative stress processes, IL-13, CD274, NOX1 and TNF, were found to be altered by radiation in hypoxia. Also, genes involved in metastatic processes, i.e. Epithelial-To-Mesenchymal-Transition (EMT)-related genes were found to be significantly changed.

Mechanistic oxygen effects

Since radicals and ROS caused by radiation or hypoxia critically influence cells' survival and EMT (i.e. potential metastasis formation) processes, cells have developed many radical scavenging systems. Two main scavenging systems hereby are SOD, which dismutases $O_2^{\bullet-}$ to H_2O_2, and CAT, which reacts H_2O_2 to O_2 (see Section 2.3.1). Hence, in Publication III, the effect of these two systems on cell migration was investigated on a mechanistic level in brain neuroglioma cells (H4) by adding copper(II) (CuL) and iron(III) (FeL) complexes to cells prior to irradiation. In the study, the effect of CuL and FeL on cells was tested with regard to their SOD-mimicking potential and subsequently their impact on cell growth after irradiation. This was investigated in both mono-layer-cell culture and in spheroids: The mono-layer stud-

ies showed that after treatment with CuL and FeL, the cell cycle of the cells was changed, leading to a build-up in G2/M phase with this effect being more prominent for CuL treatment. In spheroid studies, where cells were grown in a 3D-culture in a matrigel, the invasiveness of the spheroids was tested with and without CuL/FeL-compounds. Interestingly, less invasiveness, i.e. less metastatic potential was found for cells treated with CuL hinting towards the critical role which SOD as a ROS scavenger has in metastasis formation.

Oxygen effects in FLASH radiotherapy

In addition, the role of oxygen in FLASH radiotherapy was further investigated in Publication I, where oxygen depletion was measured in water phantoms over a large range of dose rates up to 340 Gy/s. This study was advanced in Appendix A.1 towards Ultra High Dose Rate (UHDR) up to 10^9 Gy/s produced by laser accelerated protons. These results were compared to UHDR-electrons. Furthermore, different beam pulse structures were tested in order to investigate the effect of beam pulse micro- and macro-structures on the oxygen depletion in water. Hereby, it was found that the pulse structure itself plays a major role in oxygen depletion, besides common influence by the dose rate and LET of the radiation.

Studies were also conducted as a combined irradiation of „oxygen sensor + cells" (see Appendix B.2) and „oxygen sensor + zebrafish embryos" (see Appendix B.1) in order to link the measurable changes in oxygen during conventional and FLASH radiotherapy to biological responses or, vice versa, modulating the FLASH effect by actively changing oxygen (see Appendix B.2). The studies shown in Appendix A.1, B.1 and B.2 lay the foundation for the combined measurement of the oxygen effects under FLASH conditions on a biological and radio-chemical level.

P.I: Does FLASH deplete Oxygen? Experimental Evaluation for Photons, Protons and Carbon Ions.

Authors:	**Jeannette Jansen**, Jan Knoll, Elke Beyreuther, Jörg Pawelke, Raphael Skuza, Rachel Hanley, Stephan Brons, Francesca Pagliari, Joao Seco
Status:	Published
Journal:	Medical Physics
Copyright:	Open Access, License: CC BY
DOI:	10.1002/mp.14917
Contributions:	**JJ** and **JS** came up with the idea of measuring oxygen depletion during radiation. **JJ** designed and conducted experiments for all relevant irradiation modalities. Pre-tests with the equipment was done by **JJ**, RH and FP. For the experiments with photons and carbon ions, **JJ** was supported by RS and JK. SB supported for carbon ion experiments. For proton experiments, **JJ** was supported by JP and EB from Oncoray, Dresden. Data evaluation and analysis was performed by **JJ**, with the used algorithm being developed by **JJ** as well. The results were interpreted by **JJ** and JS. **JJ** drafted and revised the manuscript with critical review by all co-authors.

Does FLASH deplete oxygen? Experimental evaluation for photons, protons, and carbon ions

Jeannette Jansen and Jan Knoll
Division of Biomedical Physics in Radiation Oncology, German Cancer Research Center (DKFZ), Heidelberg, Germany
Faculty of Physics and Astronomy, Ruprecht-Karls-University, Heidelberg, Germany

Elke Beyreuther
OncoRay–National Center for Radiation Research in Oncology, Faculty of Medicine and University Hospital Carl Gustav Carus,
Technische Universität Dresden, Helmholtz-Zentrum Dresden–Rossendorf, Dresden, Germany
Helmholtz-Zentrum Dresden–Rossendorf (HZDR), Institute of Radiation Physics, Dresden, Germany

Jörg Pawelke
OncoRay–National Center for Radiation Research in Oncology, Faculty of Medicine and University Hospital Carl Gustav Carus,
Technische Universität Dresden, Helmholtz-Zentrum Dresden–Rossendorf, Dresden, Germany
Helmholtz-Zentrum Dresden–Rossendorf (HZDR), Institute of Radiooncology-OncoRay, Dresden, Germany

Raphael Skuza and Rachel Hanley
Division of Biomedical Physics in Radiation Oncology, German Cancer Research Center (DKFZ), Heidelberg, Germany
Faculty of Physics and Astronomy, Ruprecht-Karls-University, Heidelberg, Germany

Stephan Brons
Heidelberg Ion-Beam Therapy Center (HIT), Heidelberg, Germany

Francesca Pagliari
Division of Biomedical Physics in Radiation Oncology, German Cancer Research Center (DKFZ), Heidelberg, Germany

Joao Seco[a]
Division of Biomedical Physics in Radiation Oncology, German Cancer Research Center (DKFZ), Heidelberg, Germany
Faculty of Physics and Astronomy, Ruprecht-Karls-University, Heidelberg, Germany

Purpose: To investigate experimentally, if FLASH irradiation depletes oxygen within water for different radiation types such as photons, protons, and carbon ions.
Methods: This study presents measurements of the oxygen consumption in sealed, 3D-printed water phantoms during irradiation with x-rays, protons, and carbon ions at varying dose rates up to 340 Gy/s. The oxygen measurement was performed using an optical sensor allowing for noninvasive measurements.
Results: Oxygen consumption in water only depends on dose, dose rate, and linear energy transfer (LET) of the irradiation. The total amount of oxygen depleted per 10 Gy was found to be 0.04% atm - 0.18% atm for 225 kV photons, 0.04% atm - 0.25% atm for 224 MeV protons, and 0.09% atm - 0.17% atm for carbon ions. Consumption depends on dose rate by an inverse power law and saturates for higher dose rates because of self-interactions of radicals. Higher dose rates yield lower oxygen consumption. No total depletion of oxygen was found for clinical doses.
Conclusions: FLASH irradiation does consume oxygen, but not enough to deplete all the oxygen present. For higher dose rates, less oxygen was consumed than at standard radiotherapy dose rates. No total depletion was found for any of the analyzed radiation types for 10 Gy dose delivery using FLASH. © *2021 The Authors. Medical Physics published by Wiley Periodicals LLC on behalf of American Association of Physicists in Medicine.* [https://doi.org/10.1002/mp.14917]

1. INTRODUCTION

Over the last years, research on the irradiation with high dose rates (i.e., FLASH irradiation) became increasingly important. *In vivo*, studies showed a radio-protective effect in healthy tissue when irradiated with electrons at high dose rates ($>$ 40 Gy/s) whereas the tumor control probability remained comparable to usual (clinical) dose rates of around 2 Gy/min.[1] Applied to a clinical setup, FLASH dose rate irradiation could therefore enlarge the therapeutic window, that is, healthy tissue is protected and irradiation with higher doses in the tumor is made possible.

Although this differential effect of radio-protection of the normal tissue has been studied and confirmed already *in vivo*,[2] the mechanism behind the FLASH effect still remains unknown.[3] It is believed that dissolved oxygen in the cellular cytoplasm plays a major role: Early findings in the 1960s and 1970s showed a hypoxic-like cell survival behavior when Escherichia coli bacteria were irradiated with ultra-high dose rates of x-rays.[4] Oxygen measurements for the same

experimental setup showed a decrease in oxygen during irradiation. Similar results were obtained in HeLa cells[5] and Chinese hamster cells.[6] One of the possible mechanisms to explain the FLASH effect nowadays is that oxygen is depleted during irradiation which causes a hypoxic environment in the irradiated volume. Hypoxic tissues are known to be two to three times more radio-resistant than normoxic tissues.[7] As tumors are mostly hypoxic (i.e., the O_2 concentration is lower than 0.5% atm) and healthy tissue (with an O_2 concentration of 1–11%[8]) is not, the oxygen depletion theory is of current interest as it could explain the observed radio-protective effect.

In this case, the consumption of oxygen, which can lead to complete depletion, is due to radiolysis. This process creates various radicals which then react with oxygen and result in a decrease in molecular oxygen.

1.A. Radiolysis

Ionizing radiation causes radiolysis of water molecules producing a range of reactive species (see Table I). On short timescales after irradiation (until 10^{-12} s), a high production of e^-_{aq} and $H^.$ is observable. In the presence of molecular oxygen dissolved in water, these species can interact with O_2 which leads to the production of superoxide ($O_2^{.-}$) and $HO_2^.$. These products react further with each other on timescales until up to 10^{-6} s. After 10^{-6} seconds, the production of most radicals is in a stable regime and will not cause further reactions.[3] For the studies presented, those reactions, which have O_2 as direct product or educt, are of main interest, that is, reactions in which O_2 is directly consumed or produced (see Tables II and III).

For deeper understanding, it is crucial to quantify the amount of oxygen that is consumed as a result of irradiation. This amount is given by G-values, describing the amount of molecules produced per 100 eV imparted in the water (Table I).

Various simulation studies have been published to date,[3,11,12] but there is a lack of measurement data and systems that not only measure oxygen consumption before and after irradiation, but can also be used *in-vitro* (i.e., together with cell culture) and online. The aim of this work is therefore to investigate experimentally the oxygen consumption in pure water as a potential mechanism of FLASH using an online oxygen meter. Thereby, the study is designed to cover

TABLE II. Reactions consuming oxygen.[3]

Reaction	Reaction rate k $[10^{10}\mathrm{dm^3mol^{-1}s^{-1}}]$
$e^-_{aq} + O_2 \rightarrow O_2^{.-}$	1.9
$H^. + O_2 \rightarrow HO_2^.$	2.0

TABLE III. Reactions producing oxygen.[3]

Reaction	Reaction rate k $[10^{10}\mathrm{dm^3mol^{-1}s^{-1}}]$
$OH^. + HO_2^. \rightarrow O_2 + H_2O$	1.0
$OH^. + O_2^{.-} \rightarrow O_2 + OH^-$	0.9
$HO_2^. + HO_2^. \rightarrow H_2O_2 + O_2$	0.000076
$HO_2^. + O_2^{.-} \rightarrow O_2 + HO_2^-$	0.0085

a broad range of radiation types (x-ray, p, and ¹²C radiation) and dose rates (2 Gy/min–340 Gy/s).

2. MATERIALS AND METHODS

2.A. Preparation of oxygen meter for measuring dissolved oxygen

For the experimental part of the study, radiolysis of water and the resulting oxygen consumption were investigated using the solid optical sensors TROXSP5 from PyroScience GmbH in a 3D-printed water phantom.

The water phantoms suitable for this study had to be airtight, preparable in different geometries to adapt to different irradiation beam setups and transparent to read the sensor optically. To fulfill these requirements, phantoms were 3D-printed out of the material VeroClear (Stratasys Ltd., Israel), a rigid, colorless, and transparent material. The optical sensor was glued with silicone into the phantom and the phantom was filled with de-ionized water. The oxygen dissolved in water was measured via a fluorescent layer in the sensor, which was read-out with the purchased system FireStingO2 (FSO2-4, PyroScience GmbH). With the FireStingO2, the sensor is excited at 650 nm wavelength and emits light in the near infrared regime. This signal is then further processed in the FireStingO2. Time resolution of around 400 ms can be achieved.

Since the read-out is performed optically, it was possible to measure the changes in oxygen concentration inside a water phantom noninvasively. This is the main advantage

TABLE I. G-values in molecules/100 eV of primary radicals for photon radiation[9] and for ion radiation[10] in water at 25 °C and pH 7.

G value of:	Photons (1.2 MeV)	Protons (1 keV/μ m)	¹²C		
			10 keV/μ m	15 keV/μ m	20 keV/μ m
$^.OH$	2.7	2.5	1.7	1.5	1.3
e^-_{aq}	2.6	2.3	1.5	1.3	1.1
H_2O_2	0.70	0.68	0.83	0.87	0.89
$H^.$	0.60	0.63	0.69	0.67	0.65
H_2	0.45	0.49	0.62	0.68	0.71

over studies with other commonly used oxygen probes where measurements are usually an invasive process.

The phantom itself was 20 mm long, of cylindrical shape and produced for multiple beam diameters, to achieve a uniform dose distribution within the phantom. Hence, the phantom's diameter was constructed significantly smaller than the FWHM of the respective beam used for irradiation. For the present study, phantoms of 5 mm (Fig. 1) in diameter were applied for photon radiation, and phantoms of 2 mm in diameter were applied for proton and ^{12}C radiation.

2.B. Photons, protons, and carbon ion beams

To investigate the oxygen consumption as a function of dose and dose rate (i.e., the amount of dose deposited per time interval), the water phantom with the sensor was irradiated at different dose rates with vertical beams of 225 kV photons (Faxitron MultiRad225, Faxitron Bioptics, LLC). Irradiations with carbon ions were performed at Heidelberg Ion beam Therapy facility HIT, Germany at up to 9.5 Gy/s peak dose rate using the horizontal beam line in the QS room of HIT. Irradiations with protons were performed at OncoRay, Dresden, Germany at dose rates up to 340 Gy/s using the horizontal beam line in the experimental room of the University Proton Therapy facility. The applied beam parameters can be found in Table IV. For both proton and carbon ion setups, the phantom was irradiated with high energy particles, that is, in the plateau region of the depth-dose curve of the beam.

2.C. Measurement setup

For measuring oxygen consumption, the phantom was filled entirely with pure, double-deionized water, without air bubbles, and closed with plastic screws. The oxygen content of the water was changed using a Sci-Tive hypoxic chamber (Baker Ruskinn), in which N$_2$ is used as air substitute. The
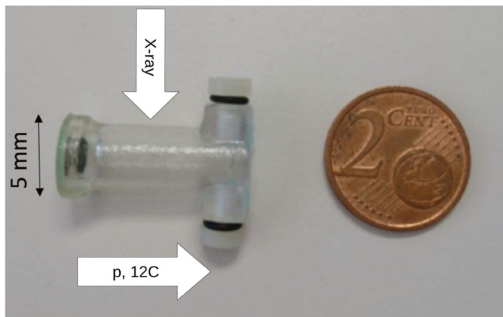

FIG. 1. Three-dimensional-printed water phantom of 5 mm inner diameter. O$_2$ sensor (black) is placed on the inside on the left end, facing away from the beam. At this side, the optical fiber can be coupled to the phantom. On the right, facing the beam, two openings for filling the phantom are visible, which can be closed with plastic screws. O-rings were used between the screws and the phantom for additional air tightness. The white arrows show the beam's direction for the respective beam types. [Color figure can be viewed at wileyonlinelibrary.com]

TABLE IV. Beam parameters used for irradiation. Linear energy transfer (LET) was calculated using ICRU49[13] and ICRU73[14]. Photon LET was estimated[15].

	Energy	LET$_{H2O}$ [keV/μ m]	Av. DR [Gy/s]	Spill DR [Gy/s]	Beam Structure
X-ray	225 kV	~1.7	0.03–52	-	continuous
p	224 MeV/u	0.42	0.03–340	-	2 ns beam-on + 8 ns beam-off
^{12}C	400 MeV/u	10.89	0.06–2.4	0.12–5.1	1.5 s–4.9 s on + 4 s–5 s off
^{12}C	150 MeV/u	19.47	0.04–1.8	0.06–9.5	1.5 s–4.9 s on + 4 s–5 s off

pure water was placed in the hypoxic chamber for 2 days until the desired O$_2$ level was reached and the phantoms were then filled with hypoxic water inside the chamber. Then, the phantom was placed at the beam's central beam axis. For proton and carbon ion measurements, the phantom's cylinder axis was placed on the beam axis. For photon measurements, the phantom was placed perpendicular to the beam instead. By that, the phantoms were always positioned horizontally to ensure homogeneous water composition. On the sensor's side of the phantom, a fiber holder was placed to connect the phantom's sensor to the FireStingO2 meter with a 2 m long optical fiber of 2.2 mm diameter. The FireStingO2 meter was then connected to the laptop for data acquisition. The obtained values for O$_2$ concentration are in a range of 0% - 20.95% (air saturated). Figure 2 shows a photograph of the experimental setup for proton radiation.

2.D. Beam microstructure

For defining the dose rate, recent studies have raised the importance to distinguish continuous wave (CW) and spilled (pulsed) beams.[16] In order to achieve the same average dose rate in a spilled beam compared to a CW beam, a much higher dose rate would be required in each pulse of a spilled beam to compensate for the beam pauses. Hence, for spilled beams, it is crucial to take both the pulse dose rate (i.e., the dose rate obtained in one spill) and the average dose rate into account.[17]

In this study, clear CW structure was obtained in x-rays. Protons at OncoRay show a quasi-continuous structure: 2 ns beam-on time is followed by 8 ns beam-off. At HIT, the beam shows a spill-like structure: A continuous beam during spill duration of 1.5-4.9 s and a time between two spills of around 4-5 s in which no particles and hence no dose is delivered. The study presented here shows both the oxygen consumption in pulsed beams and in CW beams.

2.E. Dosimetry

The dosimetry at phantom site for photon irradiation was carried out using a Semiflex ionization chamber (IC, type number TM31010, PTW, Germany). For carbon ion
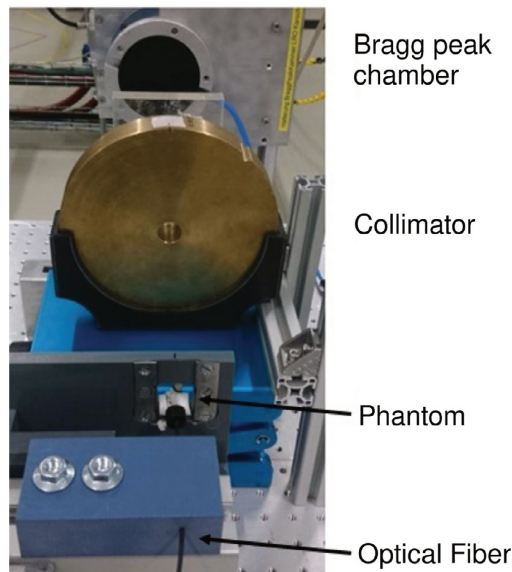
FIG. 2. Experimental setup at OncoRay, Dresden for irradiation with 224 MeV protons. The beam passed a Bragg peak chamber (model T34070-2.5 from PTW) for dose monitoring and was shaped with a scatterer of 24 mm PMMA equivalent thickness and a 20 mm thick brass collimator to deliver a homogenous beam spot. The phantom was held in place with a sample holder. [Color figure can be viewed at wileyonlinelibrary.com]

irradiation, a PinPoint chamber (type number TM31015, PTW, Germany) was used and both, respectively, coupled to a Unidos electrometer (PTW, Germany). Proton dosimetry was achieved using an Advanced Markus IC (type number: 34045, PTW), coupled to an Unidos electrometer as well. For the maximum dose rate of 340 Gy/s applied, a small

saturation correction k_{sat} of 1.01 was determined for the Markus IC.[18] Therefore, recombination effects can be neglected and no dose rate dependent saturation correction was applied.

In the experiments with photons presented in this study, it was possible to take additional advantage of the beam's geometry: The beam is conically shaped (as schematically shown in Fig. S-1a) and the dose is hence inversely proportional to the squared distance from the source, that is, $D \sim 1/r^2$. Accordingly, the same must apply to the dose rate, that is, $\dot{D} \sim 1/r^2$. Therefore, irradiating the phantom at different distances from the source automatically leads to a $1/r^2$-dependent dose rate (see Fig. S-1b) that can be used for further measurements. In the experiments with protons and carbon ions, dose rate and dose was changed by setting the beam current and irradiation time in the beam control system.

3. RESULTS

3.A. Oxygen consumption for varying water phantom volumes

At first, different phantoms with 80 μl, 583 μl, 6.138 ml, and 6.876 ml water volume were irradiated at a constant dose rate of 0.0799 Gy/s with 225 kV photons and the concentration of O$_2$ was measured during irradiation until the concentration of O$_2$ reached zero. The results of this study are displayed in Fig. 3(a). It was observed that the rate of oxygen removal (i.e., dO/dt) was mostly constant and especially independent on the irradiated volume, as long as the phantoms were irradiated homogeneously. Therefore, due to the observed independence on volume, the phantom's diameter was selected according to the beam's geometries for the following experiments. The stability of O$_2$ over time in the phantom was tested without radiation for different oxygen levels. Even for low O$_2$ levels, no diffusion was visible [see Fig. 3(b)].
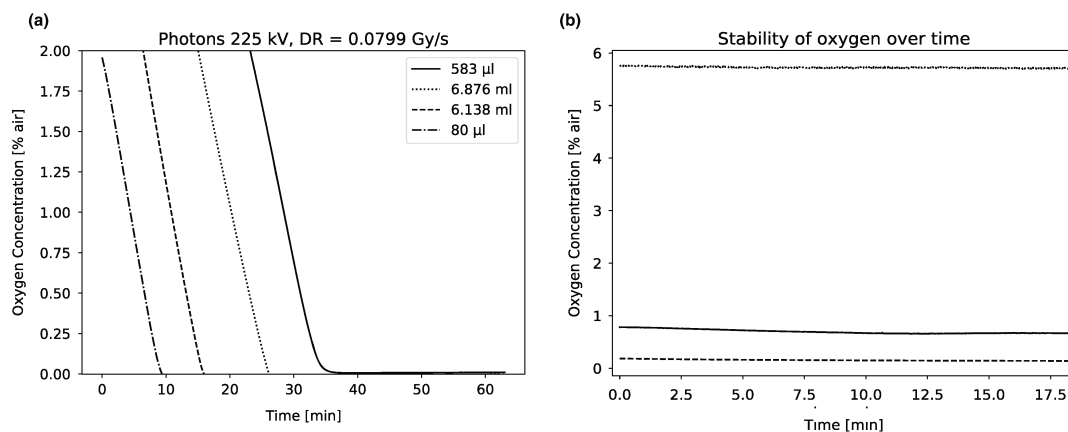

FIG. 3. (a) Oxygen consumption for phantoms with different volumes, irradiated with a dose rate (DR) of 0.0799 Gy/s. For better visibility, the curves are separated with a time-offset. (b) Oxygen stability was checked in phantom prior to irradiation.
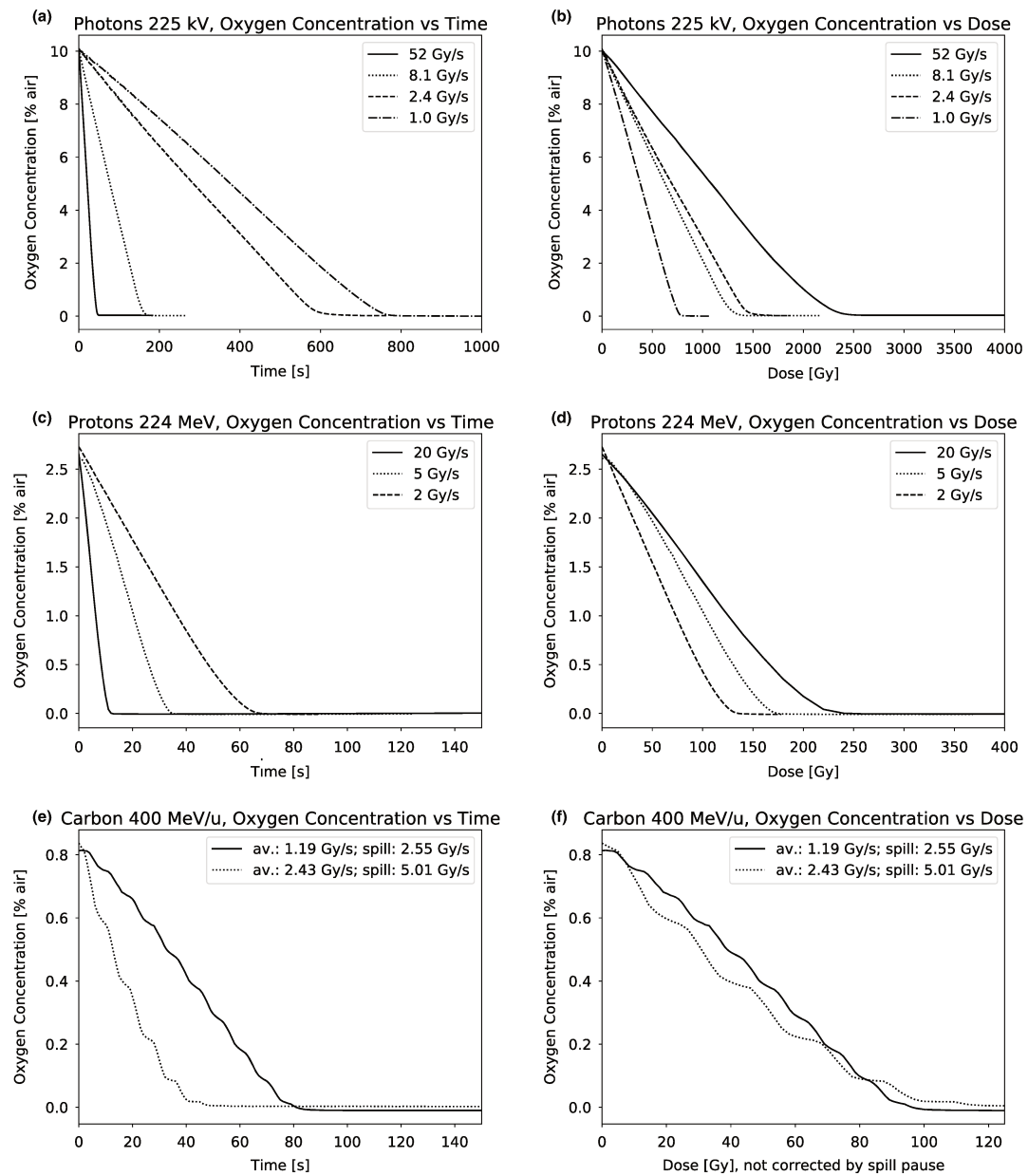
FIG. 4. Oxygen concentration over irradiation time and dose for photon, proton, and carbon irradiation. For better comparison, some curves were shifted in time to match the same initial O$_2$ level

3.B. Oxygen Consumption in Photons, Protons, and Carbon Ion Beams

At all radiation sources, the oxygen consumption in dependence on irradiation time was studied for different dose rates [Figs. 4(a), 4(c), 4(e)]. For photons and protons, the dose-dependent oxygen consumption can be achieved by multiplying the time axis with the dose rate present during irradiation [Figs. 4(b), and 4(d)]. For carbon ions, beam delivery in spills results in a step-wise oxygen consumption

[Figs. 4(e), 4(f)]. For transferring the time axis into a dose axis, the average dose rate was used. For better comparison, curves were shifted in time to match the same oxygen start level, that is, irradiation also happened at $t < 0$. This was a reasonable simplification as the depletion behavior was mostly linear.

All measurements showed that dose rate had an impact on how fast oxygen got consumed and how much dose was needed for total depletion. Furthermore, the curves showed an almost linear behavior, that is, the average consumption per unit dose ($\frac{dO}{dD}$) was extracted via a linear fit.

Subsequently, a broader analysis over multiple measurements was carried out to extract the average amount of depleted oxygen per unit dose ($\frac{dO}{dD}$) as a function of dose rate. To obtain the average consumption $\frac{dO}{dD}$, the curves from data like exemplarily shown in Figs. 4(b), 4(d) and 4(f) were linearly fitted, beginning from the start of irradiation, and the slope fit parameters ($\frac{dO}{dD}$) were used for further analysis in Fig. 5. The resulting average consumption $\frac{dO}{dD}$ was plotted against the respective dose rate for all radiation types in Fig. 5. For carbon ion data, $\frac{dO}{dD}$ was plotted against the dose

rate within one spill and not the average dose rate. The fit function used in Fig. 5 to describe the amount of consumed oxygen per dose was chosen according to Labarbe et al.[19] and Mihaljevic et al.[20] and is given by a power law, with the parameters $a \leq 0$ and $b > 0$:

$$\frac{dO}{dD} = a + b \cdot \left(\frac{dD}{dt}\right)^{-0.5} \tag{1}$$

Equation (1) was used for ¹²C data, with $\frac{dO}{dD}$ being the average consumption per measurement, derived from average dose rate in the measurement. $\frac{dD}{dt}$ described the peak dose rate. For proton and x-ray measurements, peak dose rate and average dose rate were identical, so it was more convenient to work with $\frac{dO}{dD}$ data directly from measurement. For this purpose, Eq. (1) was multiplied by $\frac{dD}{dt}$ to obtain Eq. (2). In a second step, fit parameters from Eq. (2) were used to generate Figs. 5(a) and 5(b) using Eq. (1).

$$\frac{dO}{dt} = a \cdot \frac{dD}{dt} + b \cdot \left(\frac{dD}{dt}\right)^{+0.5} \tag{2}$$
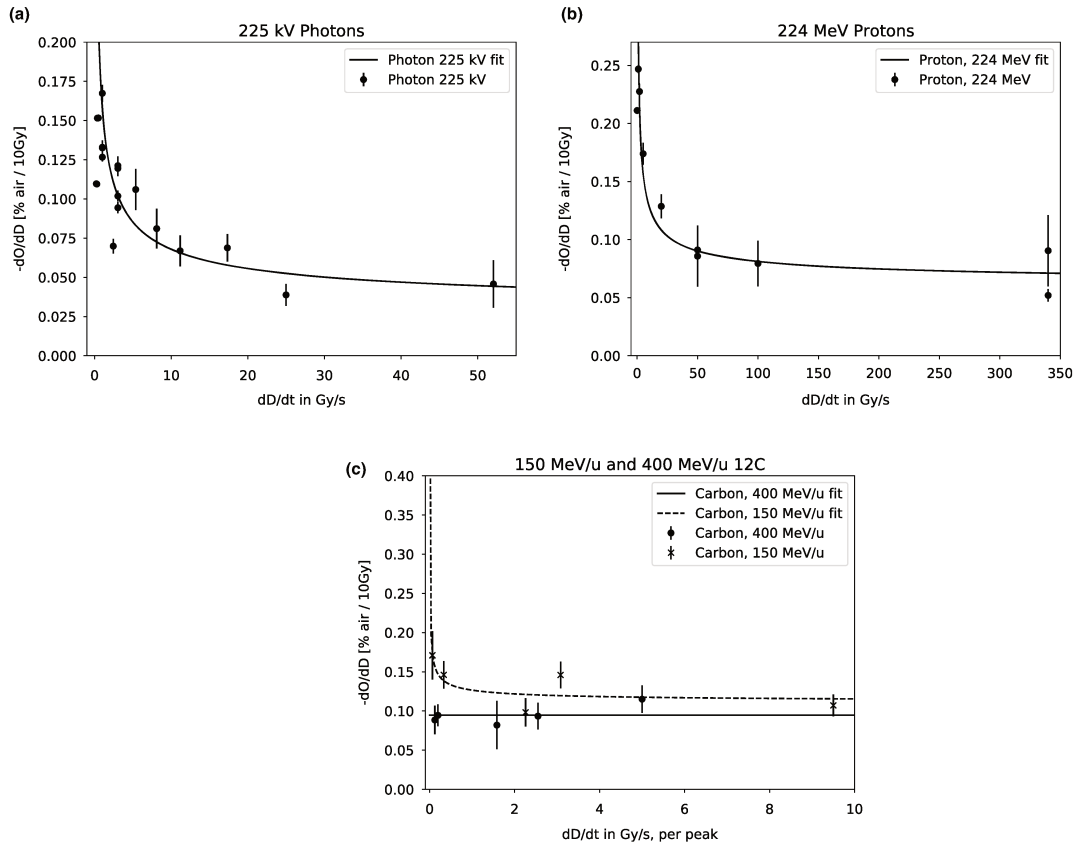

Fig. 5. Average oxygen consumption per 10 Gy ($\frac{dO}{dD}$) as a dependence on dose rate ($\frac{dD}{dt}$) depicted for all measurements in the respective beams types.
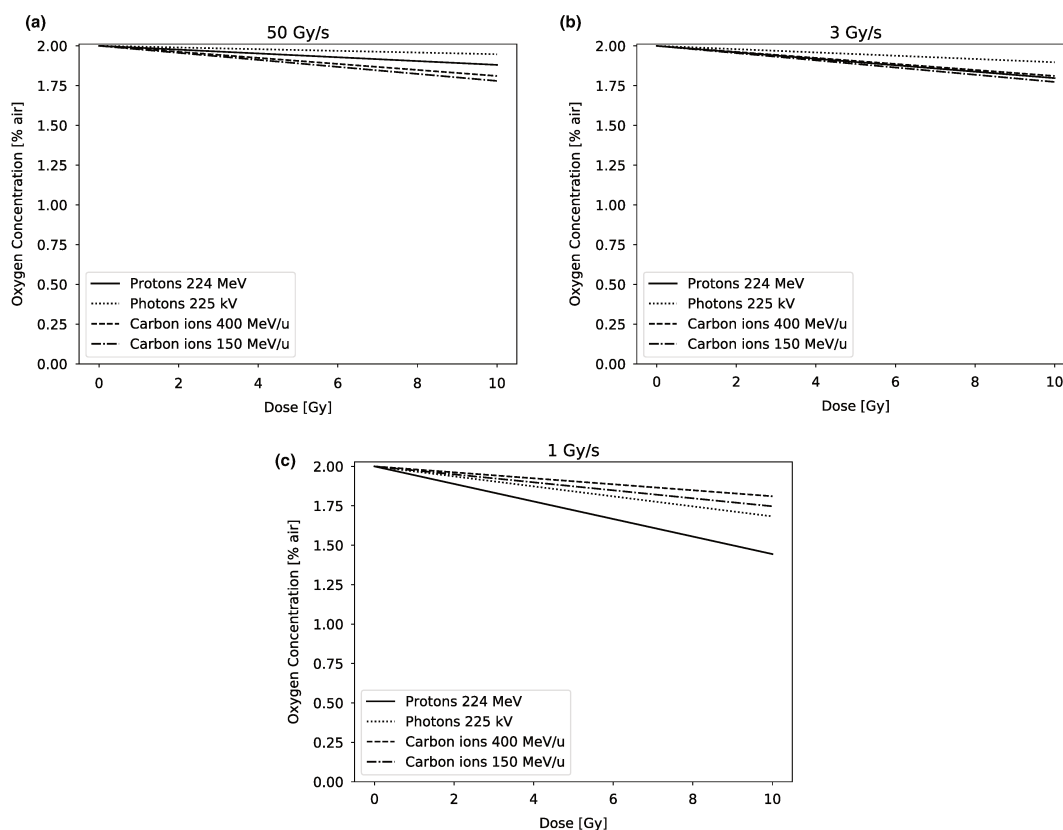
FIG. 6. Linearly extrapolated oxygen consumption starting from 2% atm O₂ for various dose rates. For all settings, large doses (more than 10 Gy) would be needed to deplete all O₂.

It is evident that all depicted curves in Fig. 5 show a similar curvature, meaning that higher dose rates lead to less oxygen consumption. Furthermore, different beam types have an impact on the oxygen consumption. Figures 6(a)–6(c) show the fit results per irradiation type applied to a starting oxygen concentration $O_{initial}$ of 2% atm and extrapolated to different dose rates, assuming a linear depletion (which is in reasonable agreement to the measured data). It was used: $O(D) = O_{initial} - \frac{dO}{dD} \cdot D$ with $\frac{dO}{dD}$ as parametrized in Eq. (1) with fit parameters a and b obtained from fits shown in Fig. 5.

Considering Fig. 6, it is evident that 2% atm O2 cannot be depleted within 10 Gy by any of the used beams.
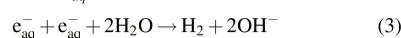
4. DISCUSSION

The aim of the study was to investigate if oxygen depletion occurs during (FLASH-) irradiation, by measuring the oxygen concentration in-vitro during irradiation of water by photons, protons, and carbon ions. For all experiments,

TROXSP5 sensors were used to measure the oxygen concentration during irradiation, with the sensors not being affected by the radiation.

The oxygen consumed during irradiation was found to be linear in time and dose and independent of the initial oxygen concentration [Figs. 4(a)–4(f)]. Oxygen consumption was evaluated per total dose delivered, where we defined $\frac{dO}{dD}$ to represent the total oxygen removed per unit dose [Figs. 4(b), 4(d), 4(f)]. The $\frac{dO}{dD}$ represents also the total amount of radicals produced per total dose delivered, which have reacted with the diluted oxygen to create a reactive oxygen species (ROS). The $\frac{dO}{dD}$ as a function of dose rate [Figs. 5(a)–5(c)] follows the same nonlinear behavior as described by Labarbe et al.[19] in organic environments, and given by the expression $a + b \cdot \left(\frac{dD}{dt}\right)^{-0.5}$. The nonlinearity was described in Labarbe et al. as the self-interaction of ROO. molecules, part of the termination reaction. In the present study, experiments were carried out with only pure water and therefore without the presence of any RH or R. molecules. However, in pure water, self-interactions of the radicals play a major role in removing

the radicals that could potentially react with oxygen. This applies especially to e_{aq}^- and $H^{\cdot}$ as described in the following:

$$e_{aq}^- + e_{aq}^- + 2H_2O \rightarrow H_2 + 2OH^- \qquad (3)$$

$$e_{aq}^- + O_2 \rightarrow O_2^{\cdot -} \qquad (4)$$

$$H^{\bullet} + H^{\bullet} \rightarrow H_2 \qquad (5)$$

$$H^{\bullet} + O_2 \rightarrow HO_2^{\bullet} \qquad (6)$$

The presence or absence of e_{aq}^- yields directly a change in O$_2$ as described in the reaction (4). Therefore one would expect that an increased dose rate should yield a higher O$_2$ consumption because of the higher production of e_{aq}^- per second. However, because of the competing reaction (3), e_{aq}^- is removed faster with increased dose rate yielding a lower steady state of e_{aq}^-. The lower steady state of e_{aq}^- means there is less of e_{aq}^- available to react with O$_2$ via reaction (4). The same process applies to $H^{\cdot}$, as described in reactions (5) and (6).

The amount of radicals produced is given by $G \cdot C \cdot \frac{dD}{dt} \cdot t$ with G being the G-value, C is a constant $(1.04 \times 10^{-7} \frac{mol}{dm^3} s \times [G]^{-1} (Gy/s)^{-1})$,[9] $\frac{dD}{dt}$ is the dose rate and t is the irradiation time. In order to understand if radicals can self-interact we need to check the mean free path length of the radicals. The radicals will diffuse for an average path length R_{rms} of $2.26 \cdot \sqrt{D_{diff} \cdot t_{\frac{1}{2}}}$[21] with $t_{\frac{1}{2}}$ being the half-life and D_{diff} being the diffusion constant. Typical values for e_{aq}^- are $D_{diff} = 4.5 \times 10^{-9} \frac{m}{s^2}$, and $t_{\frac{1}{2}} = 47 \mu s$.[21-23] From these values, a mean free path length of $: 1 \mu m$ can be estimated. Hence, it becomes clear that the solvated electrons e_{aq}^- diffuse far enough to interact with each other, ultimately reducing the steady state's concentration. Therefore, O$_2$ consumption is reduced with increasing dose rate as observed in our experiments.

The study presented here showed that for FLASH dose rates, radical recombinations, via reaction (3) and (5), reduce the oxygen consumption within the medium. In addition, we observed experimentally that the amount of oxygen consumed by radiation depends also on the particle type and its LET but further investigation would be needed. For the case of 10 Gy dose delivery, the amount of oxygen consumed was 0.04% atm - 0.18% atm for 225 kV photons, 0.04% atm - 0.25% atm for 224 MeV protons, and 0.09% atm - 0.17% atm for carbon ions, dependent on the dose rate [Figs. 5(a)–5(c)]. The obtained experimental values are in good agreement with other published results of experiments in water, where oxygen consumption was between 0.26% atm and 0.42% atm[4,24-27] for photon radiation. Recent modeling studies also yielded oxygen consumption between 0.05% atm and 0.27% atm[9,3,11] for photon, proton, and carbon ion beams. In addition, a theoretical prediction by Petersson et al.[12] yields an oxygen consumption in the range of 0.1% atm to 2% atm for total delivered dose of 10 Gy with FLASH. Applying the experimental findings and curves of Figs. 5(a)–5(c) onto an exemplary case of a water phantom with 2% atm O$_2$ content, it is evident that 10 Gy radiation of any analyzed radiation type cannot deplete oxygen completely in water [Figs. 6(a)–6(c)]. It can be concluded, that for higher FLASH dose rates, less oxygen depletion per dose was observed.

5. CONCLUSION

This study showed that TROXSP5 sensors are a suitable sensor type to measure oxygen consumption during radiation noninvasively in water phantoms. No total depletion of oxygen was observed for 10 Gy delivery by FLASH irradiation for photons, protons, and carbon ions. Hence, oxygen depletion is not a suitable mechanism to explain the FLASH effect alone but rather a reduction of oxygen consumption was found for higher dose rates which was related to the lower steady state values of e_{aq}^- radicals. The results presented here are in good agreement with previous data and recent radiochemical models but the outcome stresses **nonlinear dose rate dependence** of the oxygen consumption, even without the presence of organic molecules, which is to date not implemented in current models.

CONFLICT OF INTEREST

The authors declare no conflict of interest.

a)Author to whom correspondence should be addressed. Electronic mail: j.seco@dkfz-heidelberg.de.

REFERENCES

1. Vincent F, Laura C, Virginie M, et al. Ultrahigh dose-rate FLASH irradiation increases the differential response between normal and tumor tissue in mice. *Sci Trans Med*. 2014;6:1–10.
2. Vozenin M-C, De Fornel P, Petersson K, et al. The advantage of FLASH radiotherapy confirmed in mini-pig and cat-cancer patients. *Clin Cancer Res*. 2019;25:35–42.
3. Daria B, Michael K. Fuss MC, Durante M. Scifoni Emanuele. Impact of target oxygenation on the chemical track evolution of ion and electron radiation. *Int J Mol Sci*. 2020;21:424.
4. Weiss H, Epp ER, Heslin JM, Ling CC, Santomasso A. Oxygen depletion in cells irradiated at ultra-high dose-rates and at conventional dose-rates. *Int J Radiat Biol*. 1974;26:17–29.

5. Town CD. Effect of high dose rates on survival of mammalian cells. *Nature*. 1967;215:847–848.
6. Berry RJ, Hall EJ, Forster DW, Storr TH, Goodman MJ. Survival of mammalian cells exposed to x rays at ultra-high dose-rates. *Br J Radiol* 1969;42:102–107.
7. Walter T, Marco D, Ryoichi H, et al. Kill-painting of hypoxic tumours in charged particle therapy. *Sci Rep*. 2015;5:1–13.
8. Aude C, El H-R, Agata M, Catherine G, Claudine K. Why is the partial oxygen pressure of human tissues a crucial parameter? Small molecules and hypoxia. *J Cell Mol Med*. 2011;15:1239–1253.
9. Joseph Jiju M, Seon CB, Pam Y, Clara WJ. A combined experimental and model analysis on the effect of pH and O$_2$ (aq) on γ-radiolytically produced H$_2$ and H$_2$O$_2$. *Radiat Phys Chem*. 2008;77:1009–1020.
10. Jintana M, Jean-Paul J-G. High-LET radiolysis of liquid water with. 1H+, 4He2+, 12C6+, and 20Ne9+ ions: effects of multiple ionization. *J Phys Chem A*. 2005;109:6406–6419.
11. Guillem P, Kapp DS. A computational model of radiolytic oxygen depletion during FLASH irradiation and its effect on the oxygen enhancement ratio. *Phys Med Biol*. 2019;64:185005.
12. Kristoffer P, Gabriel A, Karl B, McMahon SJ. A quantitative analysis of the role of oxygen tension in FLASH radiotherapy. *Int J Radiat Oncol Biol Phys*. 2020;107(3):539–547.
13. Berger MJ, Inokuti M, Andersen HH, et al. Report 49. *J Int Commiss Radiat Units Measur*. 2016;os25:NP.
14. Peter S, Andreas S, Helmut P. Errata and Addenda for ICRU Report 73. Stopping of ions heavier than helium. *J ICRU*. 2009;5:1–10.
15. L'Annunziata MF. Nuclear radiation, its interaction with matter and radioisotope decay in Handbook of Radioactivity Analysis (Second Edition) (L'Annunziata MF, ed.):1 - 121San Diego: Academic Presssecond edition ed. 2003.
16. Wilson JD, Hammond EM, Higgins GS, Kristoffer P. Ultra-high dose rate (FLASH) radiotherapy: silver bullet or fool's gold? *Front Oncol*. 2020;9:1563.
17. Matthew EN, Mendonca Marc S, Magdalena B-C. Physics and biology of ultrahigh dose-rate (FLASH) radiotherapy: a topical review. *Phys Med Biol*. 2020;65(23):23TR03.
18. Leonhard K. Derivation of a formula describing the saturation correction of plane-parallel ionization chambers in pulsed fields with arbitrary repetition rate. *Phys Med Biol*. 2016;61:3222.
19. Rudi L, Lucian H, Julie B, Vincent F. A physicochemical model of reaction kinetics supports peroxyl radical recombination as the main determinant of the FLASH effect. *Radiother. Oncol*. 2020;153:303–310.
20. Mihaljević B, Tartaro I, Ferreri C, Chatgilialoglu C. Linoleic acid peroxidation vs. isomerization: a biomimetic model of free radical reactivity in the presence of thiols. *Organ Biomol Chem*. 2011;9:3541–3548.
21. Ruth R, Shigefumi O. Estimation of life times and diffusion distances of radicals involved in x-ray-induced DNA strand breaks or killing of mammalian cells. *Radiat Res*. 1975;64:306–320.
22. Riccardo DB, Tobias B, Fuss MC, Krämer M, Seco J. Proposal of a chemical mechanism for mini-beam and micro-beam efficacy. *Front Phys*. 2020;8:452.
23. Walker DC. The hydrated electron. *Q. Rev. Chem. Soc*. 1967;21:79–108.
24. Evans NTS. Removal of dissolved oxygen from aqueous media by ionizing radiations. *Radiat Eff*. 1969;1:19–22.
25. Day MJ. Stein G. Chemical measurement of ionizing radiations. *Nature*. 1949;164:671–672.
26. Whillans DW, Rauth AM. An experimental and analytical study of oxygen depletion in stirred cell suspensions. *Radiat Res*. 1980;84:97–114.
27. Michaels HB. Oxygen depletion in irradiated aqueous solutions containing electron affinic hypoxic cell radiosensitizers. *Int J Radiat Oncol Biol Phys*. 1986;12:1055–1058.

SUPPORTING INFORMATION

Additional supporting information may be found online in the Supporting Information section at the end of the article.

Fig S1. (a) Schematic of the conically shaped beam in Faxitron225. (b) Dose rate depends proportionally on $1/r^2$, r being the distance to the beam source. Fit curve in (b) was used to determine dose rates close to source.

P.II: A Novel Analysis Method for Evaluating the Interplay of Oxygen and Ionizing Radiation at the Gene Level

Authors: **Jeannette Jansen**, Patricia Vieten, Francesca Pagliari, Rachel Hanley, Maria Grazia Marafioti, Luca Tirinato, Joao Seco

Status: Published

Journal: Frontiers in Genetics

Contributions: **JJ** and PV contributed equally to this publication. In order to understand the interplay of oxygen and ionizing radiation on the gene level, LT, FP and JS came up with the idea to investigate 4 different cell lines in different states of oxygenation and to compare the genetic fingerprints with and without photon irradiation. **JJ** performed the irradiation experiments with support from FP, RH and LT. For cell cycle analysis, **JJ** acquired additional samples to monitor the change of cell phases due to radiation. **JJ** prepared samples for analyzing the gene expression, and MM performed a qPCR analysis on them. The data analysis of the qPCR data was done by **JJ**. The DKFZ core facility performed a whole genome analysis on the samples and provided the authors with the raw data. On these data, **JJ** developed a novel data analysis method for evaluating the interplay of the normally intertwined conditions "oxygen" and "radiation". JS guided through this process. **JJ** tested this new data analysis method on four data sets. PV supported on these tests. In the end, **JJ** connected the results from the new analysis method with results from the cell cycle analysis. The draft of the manuscript was written by **JJ**, PV, LT and FP and revised by all co-authors.

A Novel Analysis Method for Evaluating the Interplay of Oxygen and Ionizing Radiation at the Gene Level

Jeannette Jansen[1,2†], Patricia Vieten[1,2†], Francesca Pagliari[1], Rachel Hanley[1,2], Maria Grazia Marafioti[1], Luca Tirinato[1,3*] and Joao Seco[1,2*]

[1] Department of Biomedical Physics in Radiooncology, German Cancer Research Center, Heidelberg, Germany, [2] Department for Physics and Astronomy, Ruprecht-Karls-University Heidelberg, Heidelberg, Germany, [3] BioNEM Lab, Department of Experimental and Clinical Medicine, Magna Graecia University, Catanzaro, Italy

Whilst the impact of hypoxia and ionizing radiations on gene expression is well-understood, the interplay of these two effects is not. To better investigate this aspect at the gene level human bladder, brain, lung and prostate cancer cell lines were irradiated with photons (6 Gy, 6 MV LINAC) in hypoxic and normoxic conditions and prepared for the whole genome analysis at 72 h post-irradiation. The analysis was performed on the obtained 20,000 genes per cell line using PCA and hierarchical cluster algorithms to extract the most dominant genes altered by radiation and hypoxia. With the help of the introduced novel radiation-in-hypoxia and oxygen-impact profiles, it was possible to overcome cell line specific gene regulation patterns. Based on that, 37 genes were found to be consistently regulated over all studied cell lines. All DNA-repair related genes were down-regulated after irradiation, independently of the oxygen state. Cell cycle-dependent genes showed up-regulation consistent with an observed change in cell population in the S and G2/M phases of the cell cycle after irradiation. Genes behaving oppositely in their regulation behavior when changing the oxygen concentration and being irradiated, were immunoresponse and inflammation related genes. The novel analysis method, and by consequence, the results presented here have shown how it is important to consider the two effects together (oxygen and radiation) when analyzing gene response upon cancer radiation treatment. This approach might help to unrevel new gene patterns responsible for cancer radioresistance in patients.

Keywords: hypoxia, whole genome analysis, cluster analysis, immune response, radiation, principal component analysis

1. INTRODUCTION

Cancer remains a major global health challenge, as it is estimated that the number of deaths caused by cancer might increase to over 13 million deaths per year in 2030 (World Health Organisation, 2021). Radiotherapy is one of the main methods to treat a variety of cancer types in patients and is also widely exercised in combination with other treatment modalities. To improve the therapeutic performance of radiation therapy it is indispensable to research the genetic "fingerprint" of cancer cells and to understand which molecular mechanisms can be modified to increase radiosensitivity. The oxygenation status

of a tumor has a large impact on the tissue's radio-response following photon radiation (Gray et al., 1953; Zölzer and Streffer, 2002; Dewhirst et al., 2008). Hypoxic (i.e., oxygen levels below 5% O_2) cancer cells are known to be more radioresistant while normoxic conditions enhance radiation efficiency (Liu et al., 2015). The increased radioresistance of hypoxic regions within a tumor are very critical in clinical treatments since a 2- to 3-fold higher dose is needed to reach the aimed tumor kill, when compared to the normoxic regions. Although this effect has been observed *in vitro* and *in vivo*, there are still many open questions regarding the influence of oxygen on the genetic alteration of cancer cells which would give an insight into why hypoxic cancer cells are less sensitive to radiation in comparison to normoxic cancer cells (Liu et al., 2015). Furthermore, it is known that cells surviving X-ray treatment show altered genetic expression levels especially related to DNA repair, cell cycle, inflammation and immune response (McKelvey et al., 2018). As these cells show an increased radioresistance, it is crucial to understand the effect of hypoxia in radiation treatment.

This manuscript aims to investigate the gene expression levels of different cancer cell lines [lung (H460), prostate(PC3), brain (H4), and bladder (T24)] after irradiation with 6 Gy photons in hypoxic and normoxic environment with a special focus given to DNA repair, cell cycle, inflammation and immune response genes by using a novel analysis method. Hereby, the main interest is to investigate hypoxia's influence on cells pre- and post-irradiation and how this affects the cells' repair processes in normoxia. In this work, an oxygen level of 0.3% was set for hypoxic experiments, as levels below 1% O_2 are usually considered hypoxic (McKeown, 2014). 0.3% was chosen to be in a clearly hypoxic regime while still allowing for the cells to proliferate (Carmeliet et al., 1998; Zheng et al., 2019).

2. MATERIALS AND METHODS

2.1. Sample Preparation for Irradiation

The cell lines used for the presented study were human brain neuroglioma cells (H4), human lung (pleural effusion) carcinoma cells (H460), human prostate adenocarcinoma cells (PC3), and human urinary bladder carcinoma cells (T24), all purchased from ATCC. H4 cells were cultivated in Dulbecco's Modified Eagle Medium (Thermo Fisher Scientific), H460 cells in Gibco RPMI Medium (Thermo Fisher Scientific), PC3 in Ham's F-12K (Kaighn's) Medium (Thermo Fisher Scientific) and T24 cells in McCoy's 5A (Modified) Medium (Thermo Fisher Scientific). All media were supplemented with 10% Fetal Bovine Serum (FBS) (Thermo Fisher Scientific) and 1% PenStrep [(10,000 U/mL), Thermo Fisher Scientific]. Additionally, 1% HEPES Buffer (1M) (Thermo Fisher Scientific) was added to T24 medium. For each cell line, the cells were divided into a normoxic and a hypoxic group. The normoxic group was incubated at 37°C and 5% of CO_2 at an atmospheric O_2 concentration ($\approx$21%), whereas the hypoxic group was incubated for 3 days in a Sci-Tive hypoxic chamber (Baker Ruskinn), 0.3% O_2 concentration, and N_2 as an oxygen substitute for the cells to enter a state of chronic hypoxia. These two groups were then divided further into two subgroups in which one group experienced no irradiation,

while the other subgroup experienced a dose of 6 Gy. 6 Gy was chosen because a significant DNA damage is expected at this dose whereas the amount of surviving cells is still large enough to analyze (Tang et al., 2015). The dose was delivered using a 6 MV linear accelerator (LINAC) with a field size of 20 by 20 cm. After 3 days under normoxic conditions during which the medium was changed daily, only surviving cells were collected and prepared for gene expression analysis via Affymetrix Microarrays. This radioresistant cell subpopulation was chosen for a better investigation of the DNA repair mechanisms and their interplay with the above reported genes (Kraus et al., 2002; Suzuki et al., 2003; Tang et al., 2015). In total, 16 samples were obtained.

2.2. Cell Cycle Staining With Propidium Iodide (PI)

From each sample, $1 \cdot 10^6$ cells were harvested and fixed in 1 ml of 70% ethanol. After 24 h, the ethanol was removed and the cells were treated with 100 units/ml RNase A. After an incubation time of 30 min, the RNase was washed out with PBS and the samples were stained with $1\,\mu g$ PI per 1 ml PBS. The cell cycle spectra were acquired using a BD FACS Canto II (Becton Dickinson).

2.3. Sample Preparation for DNA Microarrays and Gene Expression Analysis

Total RNA was extracted from all 16 samples using the High Pure RNA isolation kit (Roche) according to the manufacturer's instructions. All RNA samples were treated with DNase-1. The purity and the amount of RNA was checked spectroscopically. $50\,\text{ng}/\mu l$ of RNA from each sample were hybridized onto Affymetrix Gene Chip for genome wide gene expression and analysis which were performed on Affymetrix Human Genome U133 Plus 2.0 Arrays (Affymetrix). The obtained data (20,000 genes per sample) was later on processed for gene expression studies using R, version 3.6.0 (2019-04-26). Datasets were background reduced and normalized among each other using the *rma* algorithm out of the *oligo* package from Bioconductor (Irizarry et al., 2003; Carvalho and Irizarry, 2010).

2.4. Definition of Gene Expression Profiles

Analyzing gene regulation under the influence of radiation and oxygen faces the difficulty that activated response pathways are strongly correlated and cannot be clearly separated from each other. From an experimental point of view, it is not possible to investigate the gene expression response to oxygen and irradiation separately. Therefore, the separation of these effects can be obtained by the definition of two expression ratios which will be called profiles because they describe the cellular response caused by different conditions on a gene regulation level. The first profile is defined as:

$$\text{radiation-in-hypoxia} = \log_2\left(\frac{\text{expr}(6\,\text{Gy hyp})}{\text{expr}(0\,\text{Gy hyp})}\right). \quad (1)$$

This "radiation-in-hypoxia" profile calculates the gene expression alteration resulting from an irradiation with 6 Gy and simultaneously eliminates the genetic alteration due to the

absence of oxygen. In addition to that, Equation (2) defines the so-called "oxygen-impact" profile:

$$
\begin{aligned}
\text{oxygen-impact} &= \text{radiation-in-normoxia} - \text{radiation-in-hypoxia}\\
&= \log_2\left(\frac{\text{expr}(6\,\text{Gy norm})}{\text{expr}(0\,\text{Gy norm})}\right) - \log_2\left(\frac{\text{expr}(6\,\text{Gy hyp})}{\text{expr}(0\,\text{Gy hyp})}\right)\\
&= \log_2\left(\frac{\text{expr}(6\,\text{Gy norm})/\text{expr}(0\,\text{Gy norm})}{\text{expr}(6\,\text{Gy hyp})/\text{expr}(0\,\text{Gy hyp})}\right).
\end{aligned}
\tag{2}
$$

Equation (2) describes the difference between the two expression ratios "radiation-in-normoxia" and "radiation-in-hypoxia." Hereby, "radiation-in-normoxia," is constructed equivalently to Equation (1), but uses the expression values measured in normoxia. Subtracting those ratios from each other provides a quantity which describes the difference of gene regulation response to irradiation in the absence and presence of oxygen. This can therefore be used to characterize the influence of oxygen on gene regulation following irradiation treatment with a dose of 6 Gy. According to the definition of the profile, genes with positive profile values will be stated as "up-regulated" and genes with negative values as "down-regulated."

3. RESULTS AND DISCUSSION

3.1. Principal Component Analysis Shows Ability of Profiles to Reduce Cell Line Dependence

To obtain a first insight into the connecting patterns in the four samples of the investigated cell lines, a Principal Component Analysis (PCA) was performed on the normalized expression values. A PCA allows for dimension reduction via coordinate transformation into a new coordinate system with coordinates (components) representing variation. In the study presented here, the goal is to investigate, which factors (e.g. cell line, oxygen condition, radiation condition) contribute most to the overall gene expression pattern by showing the first three components, as they describe around 60% of the observed variation. PCA was done using the function *prcomp* from the *stats* package in the statistical software R. Data was scaled to unit variance beforehand. A projection onto the first and second component is shown in **Figure 1A**, and onto the first and third in **Figure 1B**. In both cases, a clear clustering of the four cell lines was visible, with *H4* and *T24* being separated from *H460* and *PC3*. It was evident that the strongest relating factor in the expression data set was the cell line to which the sample belongs.

Calculating the radiation-in-hypoxia and oxygen-impact profile as well as performing a PCA, gave a cell line independent separation of the two profiles, which is shown in **Figures 1C,D**. A clear separation of the two profiles across all four cell lines was evident when projecting the profiles on the first and third component shown in **Figure 1D**. Although the separation was weak in comparison to the distinct clustering in **Figures 1A,B**, it was clearly visible that clusters were formed based on the introduced profiles, which was most dominant in the third principal component. This confirmed that the profiles can be

used to describe an underlying mechanism which is common for multiple gene groups.

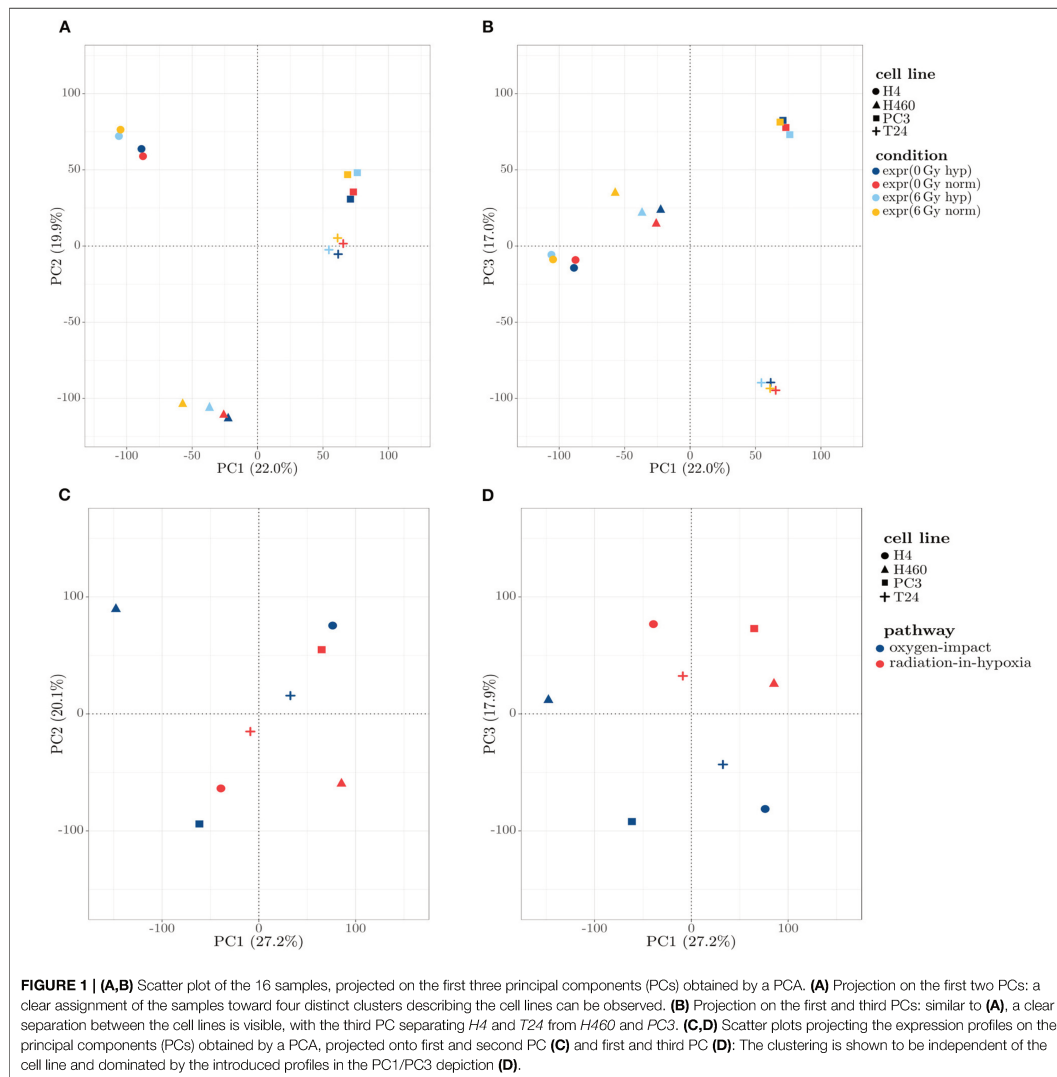### 3.2. Hierarchical Cluster Analysis Shows That Profiles Overcome Cell Line Dependence

To support the results obtained by the PCA, an unsupervised hierarchical cluster analysis was performed on the raw data and then on the profile data for a similarity check. The heatmaps shown in **Figure 2** were created by using the Euclidean distance and the complete linkage method. Both, rows (genes) and columns (samples) were hierarchically clustered. The created dendrogram at the top of the heatmap as well as the stepwise coloring in **Figure 2A** implied that the samples were more similar within one cell line in comparison to the other samples obtained from other types of tissue. This was clearly shown as the dendrogram formed four big branches, one for each cell line, which remained in accordance to the findings of the PCA. Considering the two big branches on the right for the cell lines *H4* and *H460*, it could be observed that the clustering was dividing the irradiated samples from the non-irradiated ones, which implied that radiation has a more profound effect on the clustering of *H4* and *H460* than oxygen. However, when looking at the two big branches on the left for the cell lines *T24* and *PC3*, the clustering was weak as the branches are relatively close and, therefore, did not allow for further interpretation. Nonetheless, the genes were visibly assigned to five branches, also divided by color.

3.2.1. Application of "Radiation-in-Normoxia" and "Radiation-in-Hypoxia" Profiles

The separation of the two profiles was observed in the PCA to occur only in the third principal component. Therefore, further analyses were carried out to test if other effects had a greater influence on the expression set or if the two profiles were similar across all cell lines when applying a hierarchical cluster analysis. The obtained heatmap is shown in **Figure 2B**.

Examining the dendrogram at the top of the heatmap, it was evident that two big clusters are formed, with each containing all four samples of the same profile. It can be summarized that using the expression profiles defined before, it was possible to show that within the same profile there is a strong similarity across all four cell lines. Furthermore, the *H4* and *T24* cells shared even more similarity in the genetic expression pattern compared to *PC3* and *H460*.
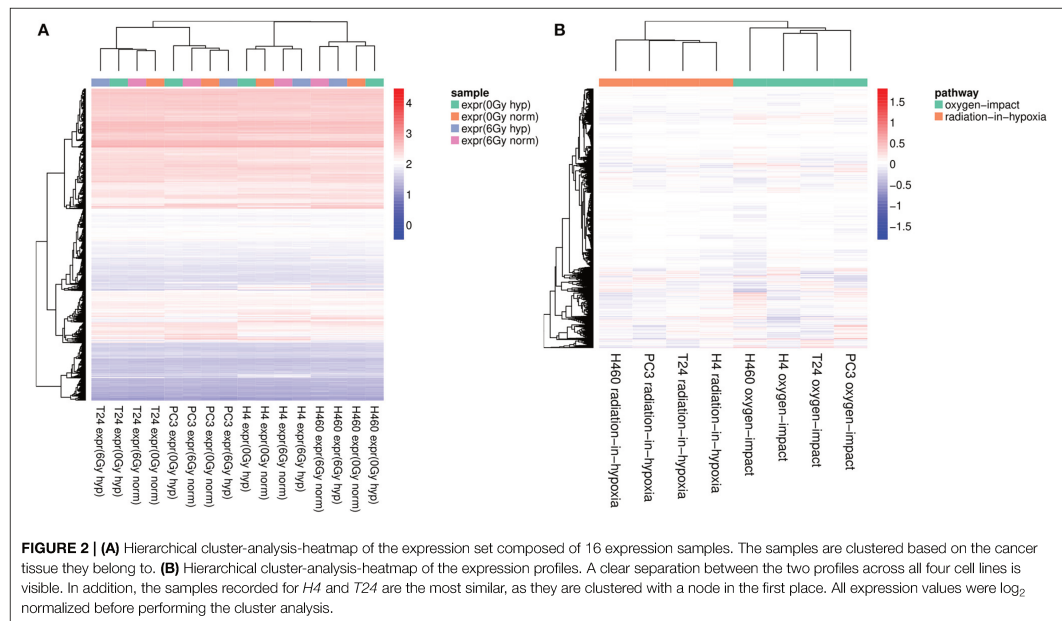
As a first conclusion, it can be summarized that a PCA (**Figures 1A,B**) and a cluster analysis (**Figure 2A**) assigned the expression data to the cell line to which they belong rather than to the samples' condition. **Figures 2A,B** shows this relatively strong cell line dependency, which is indicated by its inclusion in each of the first three principal components. Based on the clusters formed in **Figure 2A**, it was shown that for both cell lines H4 and H460, the radiative condition prevails the oxidative one. The two defined profiles, radiation-in-hypoxia and

FIGURE 1 | (A,B) Scatter plot of the 16 samples, projected on the first three principal components (PCs) obtained by a PCA. **(A)** Projection on the first two PCs: a clear assignment of the samples toward four distinct clusters describing the cell lines can be observed. **(B)** Projection on the first and third PCs: similar to **(A)**, a clear separation between the cell lines is visible, with the third PC separating *H4* and *T24* from *H460* and *PC3*. **(C,D)** Scatter plots projecting the expression profiles on the principal components (PCs) obtained by a PCA, projected onto first and second PC **(C)** and first and third PC **(D)**: The clustering is shown to be independent of the cell line and dominated by the introduced profiles in the PC1/PC3 depiction **(D)**.

oxygen-impact, were able to suppress the previous observed cell line dependency: a categorization was found, in which all four cell lines behave accordingly when analyzing the whole gene set, as shown in **Figures 1D**, **2B**. Both the radiation-in-hypoxia and oxygen-impact profiles were fully divided by a hierarchical cluster analysis. The radiation-in-hypoxia and oxygen-impact profiles were interdependent. This intrinsic dependence is the reason why it was expected that the two profiles would be separated for each cell line individually. However, the profiles are in fact separated for all investigated cell lines. Hence,

it can be extracted that across a multitude of genes, the radiation-in-hypoxia and oxygen-impact profiles describe a similar process, which is evident for all four studied cancer cell lines.

After answering the question whether there is an oxygen dependent alteration of gene expression, the actual regulation of genes of interest caused by photon irradiation of 6 Gy in absence and presence of oxygen was investigated further using the radiation-in-hypoxia and radiation-in-normoxia profiles.

FIGURE 2 | (A) Hierarchical cluster-analysis-heatmap of the expression set composed of 16 expression samples. The samples are clustered based on the cancer tissue they belong to. **(B)** Hierarchical cluster-analysis-heatmap of the expression profiles. A clear separation between the two profiles across all four cell lines is visible. In addition, the samples recorded for *H4* and *T24* are the most similar, as they are clustered with a node in the first place. All expression values were $\log_2$ normalized before performing the cluster analysis.

3.3. Gene Regulation Study

Applying the radiation-in-hypoxia and radiation-in-normoxia profiles, a hierarchical cluster analysis was performed on the behavior of a chosen group of genes involved in varying biological profiles related to DNA repair, cell cycle, inflammation and immune response. The obtained heatmap shown in **Figure 3** depicts the expression profiles of 37 genes (rows) out of the initially found 20,000. The 37 genes were specifically extracted based on their constant behavior across a majority of cell lines. The heatmap was created using the Euclidean distance and the ward linkage method. Examining the dendrogram at the left and the heatmap's coloring, the genes were clustered into three distinct groups:

A first group of genes (A), at the top of the heatmap, was characterized by positive profile values visualized by the color red. Those genes were measured to be up-regulated 3 days after irradiation with a physical dose of 6 Gy in comparison to their expression when not irradiated across the majority of cancer cell lines, according to the radiation-in-hypoxia and radiation-in-normoxia profiles' definition. This up-regulation was evident after irradiation in hypoxia as well as in normoxia.
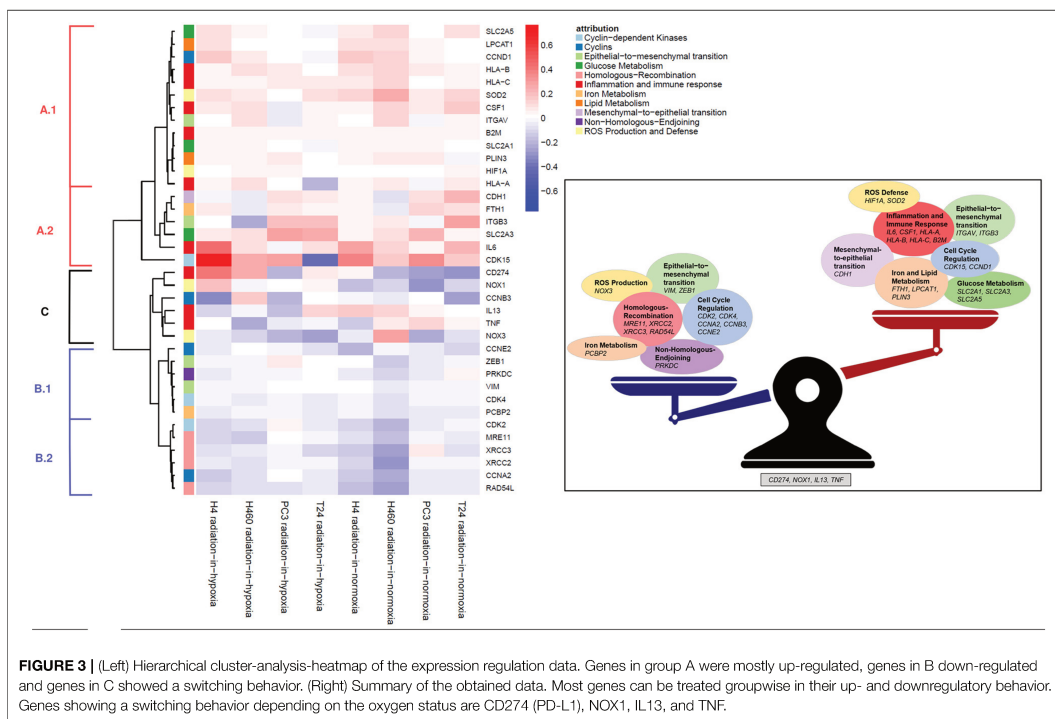
Group (B), at the bottom of the heatmap, showed down-regulation after irradiation independent from the oxygen condition. The remaining group, in the middle part of the heatmap [group (C)], showed an up-regulation after irradiation in hypoxia and a down-regulation after irradiation in normoxia or vice versa. The three groups (A–C) were analyzed according to the dendrogram at the left of the heatmap.

Additionally, to confirm the correct assignment to the groups, qPCR analysis was performed on several genes (see **Supplementary Figure 1**).

3.3.1. Inflammation and Immune Response Genes Are More Distinct After Irradiation

The first subgroup (A.1) was composed of the following genes: glucose metabolism (*SLC2A1*, *SLC2A5*), lipid metabolism (*LPCAT1*, *PLIN3*), cell cycle regulating cyclin (*CCND1*), inflammation and immune response (*HLA-A*, *HLA-B*, *HLA-C*, *B2M*, and *CSF1*), Reactive Oxygen Species (ROS) defense (*SOD2* and *HIF1A*), as well as *ITGAV* involved in epithelial-to-mesenchymal transition (EMT).

SLC2A1 and *SLC2A5* are genes encoding for GLUT1 and GLUT5 proteins, which are glucose transporters involved in its transmembrane transport (Kim et al., 2019). *LPCAT1* encodes a member of the 1-acyl-sn-glycerol-3-phosphate acyltransferase family of proteins involved in phospholipid metabolism (Stanca et al., 2013; Wu et al., 2015). CyclinD encoded by *CCND1* is active throughout the whole cell cycle and regulates the activity of the cyclin-dependent Kinases, CDK4 and CDK6, which are necessary for the initiation of the G1 phase and the G1/S phase transition (Musgrove et al., 2011). *HLA-A* and its paralogs *HLA-B* and *HLA-C* genes belong to the HLA class I heavy chain paralogs. Together with *B2M* they form the class I major histocompatibility complex (MHC-1), which is heavily involved in the presentation of foreign antigens to the immune system (Janeway et al., 2001). The gene *CSF1* encodes

FIGURE 3 | (Left) Hierarchical cluster-analysis-heatmap of the expression regulation data. Genes in group A were mostly up-regulated, genes in B down-regulated and genes in C showed a switching behavior. (Right) Summary of the obtained data. Most genes can be treated groupwise in their up- and downregulatory behavior. Genes showing a switching behavior depending on the oxygen status are CD274 (PD-L1), NOX1, IL13, and TNF.

for a protein that is a cytokine active in innate immunity and in inflammatory processes which promotes the release of proinflammatory chemokines (Hume and Macdonald, 2012; Sauter et al., 2016). Directly clustered together with *CSF1* was *ITGAV*, which belongs to the integrin alpha chain family and forms together with integrin beta-3 encoded by *ITGB3* the vitronectin receptor (αvβ3) which regulates angiogenesis and cancer progression (Antonov et al., 2011). *SOD2* encodes the antioxidant defense enzyme manganese-dependent SOD (MnSOD) that is active in the mitochondria. MnSOD plays a critical role in protection against ionizing radiation which has been indicated by numerous studies as it scavenges superoxide anion radicals which are toxic to biological systems (Miao and St. Clair, 2009; Hosoki et al., 2012). *HIF1A* encodes the alpha subunit of the transcription factor hypoxia-inducible factor-1 (HIF-1), which is also an oxidative stress defense protein (Smith et al., 2008; Anam et al., 2015).

All described genes were slightly up-regulated after irradiation in both oxidative conditions. In the case of *SLC2A5*, *LPCAT1*, *CCND1*, *HLA-B*, *HLA-C*, *SOD2*, *CSF1*, and *ITGAV* (upper part of group A1), however, this up-regulation seemed to be enhanced by irradiation in normoxia compared to irradiation in hypoxia. It can hence be concluded here that inflammation and immune response genes were more profoundly altered after irradiation. This effect was seen to be correlated with HIF1A and SOD2.

The next subgroup (A.2) of genes is characterized by a slightly more prominent up-regulation post-irradiation in comparison to no irradiation. This group was composed of the gene *CDH1* involved in mesenchymal-to-epithelial transition (MET), the iron metabolism gene *FTH1*, the already mentioned EMT gene *ITGB3*, the glucose metabolism gene *SLC2A3* encoding the glucose transporter GLUT3, and *IL6* involved in inflammation and immune response. The gene *IL6* (Interleukin 6) encodes a cytokine with a wide variety of biological functions that is active in regard to inflammation and maturation of B cells (Fuster and Walsh, 2014; Tanaka et al., 2014). It is known to act as a pro-inflammatory cytokine.

The gene *CDK15* (Cyclin Dependent Kinase 15) encoding CDK15 which is known to act as an anti-apoptotic protein (Park et al., 2014) was strongly up-regulated after irradiation in hypoxia and normoxia. Together, these data of the first analyzed group A indicated that a 6 Gy irradiation induced, even if slightly, a consistent up-regulation of genes involved in inflammation and immune response, together with *SOD2* and *HIF1A*.

3.3.2. DNA Repair Genes Are Less Expressed After Irradiation

The second group of genes (B) was characterized by negative profile values (blue) defining them to be down-regulated: the

subgroup (B.1) of genes which were slightly down-regulated post-irradiation was composed of the cell cycle dependent genes *CCNE2* and *CDK4*, two EMT genes (*ZEB1*, *VIM*), the gene *PRKDC* involved in the Non-Homologous End Joining-DNA-repair pathway (NHEJ), and the iron metabolism related gene *PCBP2*. *CCNE2* and *CDK4* are essential for the control of the cell cycle and responsible for regulating the G1/S phase transition as well as the progression through the G1 phase. The gene *ZEB1* encodes a zinc finger transcription factor which acts as a transcriptional repressor among others repressing *CDH1* promoter (Larsen et al., 2016). *VIM* encodes a structural type III intermediate filament protein expressed in various non-epithelial cells, especially mesenchymal cells and it is used as a marker of cells undergoing EMT (Liu et al., 2015). Therefore, the observed down-regulation of *ZEB1* and *VIM* shows, together with the aforementioned up-regulation of *CDH1* 72 h post-irradiation with 6 Gy, that cell migration is potentially inhibited (McInroy and Määttä, 2007). The gene *PRKDC* (Protein Kinase, DNA-Activated, Catalytic Subunit) encodes the catalytic subunit of the DNA-dependent protein kinase (DNA-PK) which is a protein acting as a molecular sensor of DNA damage and is involved in the ligation step of NHEJ pathway of DNA double strand break (DSB) repair (Davis and Chen, 2013).

The subgroup (B.2) characterized by a stronger down-regulation after irradiation in normoxia compared to their down-regulation in hypoxia was composed of the cell cycle dependent genes *CDK2* and *CCNA2*, and four genes involved in the homologous-recombination pathway: *MRE11*, *XRCC3*, *XRCC2*, and *RAD54L*. *CCNA2* binds and activates CDK2 and therefore promotes the G1/S phase and G2/M phase transition. The proteins encoded by *MRE11* (MRE11 Homolog, Double Strand Break Repair Nuclease), *XRCC3* (X-Ray Repair Cross Complementing 3), *XRCC2* (X-Ray Repair Cross Complementing 2), and *RAD54L* (DNA Repair And Recombination Protein RAD54-Like) are heavily involved in the homologous-recombination (HR) pathway of DNA DSB repair and are dominantly active throughout the S phase (Li and Heyer, 2008; Zhao et al., 2017). The downregulation of the genes mentioned in this group appeared to be correlated with the cell cycle profiles in the next section, where the percentage of cells shifts from G1 to G2/M after irradiation and this effect was seen to be stronger in normoxia. This effect will be discussed more detailed later.

3.3.3. Oxygen Dependent Response After Irradiation

There were only few genes which exhibit an oxygen dependent behavior across all four types of tissue supporting the already discussed weakness of the oxygen effect. However, analyzing the remaining group of genes (C), it was evident that post-irradiation the immune response gene *CD274* and the ROS gene *NOX1* were mostly up-regulated in hypoxia and down-regulated in normoxia in comparison to their expression without irradiation. On the other hand, the inflammation and immune response related genes, *IL13* (Interleukin 13) and *TNF* (Tumor Necrosis Factor), were mostly down-regulated in hypoxia and up-regulated in normoxia following irradiation. The cyclinB encoding gene *CCNB3* and the ROS gene *NOX3* were mostly down-regulated

after irradiation in comparison to their expression after no irradiation. *CD274* encodes for PDL1 which is an immune inhibitory receptor ligand expressed by various types of tumor cells (Huang et al., 2018). The ligand plays a critical role in induction and maintenance of immune tolerance and therefore in facilitating tumor survival by maintaining homeostasis of the immune response. *IL13* encodes an immunoregulatory cytokine which is critical in regulating inflammatory and immune responses (Minty et al., 1993; Iii et al., 2019). It inhibits the production of pro-inflammatory cytokines and chemokines. The multifunctional proinflammatory cytokine TNF encoded by *TNF* is involved in the regulation of cell proliferation, differentiation, apoptosis, lipid metabolism and coagulation (Benihoud et al., 2007; Jiang et al., 2019). *NOX1* and *NOX3* genes encode for two enzymes responsible for the catalytic one-electron transfer of oxygen to generate superoxide or H_2O_2 and therefore catalyze the production of endogenous ROS (Eun et al., 2017). The gene *CCNB3* encodes for cyclinB which is involved in regulating the G2/M transition.

It can be concluded here that the previously discussed genes in group C (and only those genes) showed an oxygen dependent response toward radiation. Moreover, especially *CD274* and *IL13* encode for proteins which are well-known to play crucial roles in immunotherapy.

3.4. Cross Check With Propidium Iodide: Buildup in G2/M Phase

Since several affected genes are known to have a cell cycle dependence, the distribution of cells in their different phases was analyzed to confirm the findings of the profile-analysis. This was reached by staining cells with propidium iodide and the obtained spectra are shown in **Figure 4**. Applying the cell cycle analysis method provided by Watson et al. (1987), the G1 and G2/M peaks were fitted with a gaussian and the total amount of cells per phase could be hence obtained. The percentage of cells per phase are shown in **Table 1**.
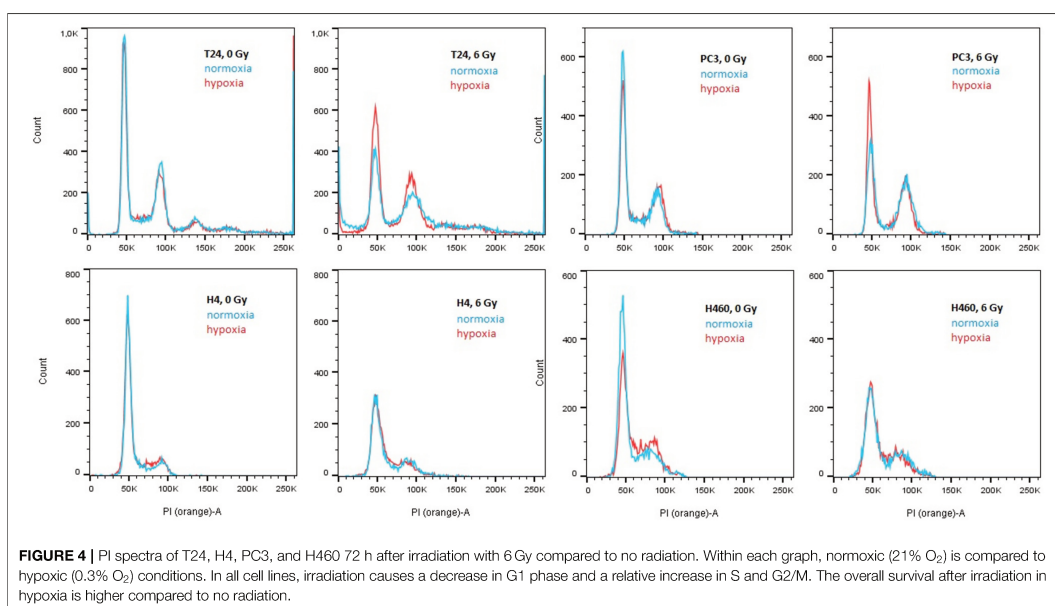
The previously mentioned upregulation of CCND1 together with the downregulation of CCNE2, CCNB3, and CCNA2 after irradiation can be explained in a relative arrest of cells in the G2/M phase (see **Figure 4**): a decrease of cells in G1 and S phase was visible in both hypoxic and normoxic conditions, whereas cells accumulated in G2. This effect was found to be stronger after irradiation in normoxia compared to hypoxia, which can be explained by the Oxygen Enhancement Ratio (OER) due to which hypoxic cells show a higher resistance toward radiation (Thoday and Read, 1947). Hence, the result of the cell cycle analysis using PI are in accordance with the findings in gene expression using the novel "radiation-in-hypoxia" and "radiation-in-normoxia" analysis.

4. CONCLUSION

In the last decades, our observations about the gene role and complexity upon ionizing radiations (IR) have made great strides. Today we know a wide number of signaling pathways, sensors, and relative transcription factors modulated by

TABLE 1 | Percentage of cells per cell phase, obtained using the Watson algorithm on the spectra from **Figure 4**.

Cell line	Oxygen in % atm	Dose in Gy	% of cells in G1	% of cells in S	% of cells in G2
T24	0.3	0	52.3 ± 5.8	31.2	12.8 ± 1.2
T24	0.3	6	46.2 ± 6.1	17.6	26.2 ± 3.1
T24	21	0	55.0 ± 4.5	29.8	14.1 ± 1.0
T24	21	6	31.1 ± 4.3	18.7	24.2 ± 3.3
H460	0.3	0	35.2 ± 4.1	45.7	13.3 ± 1.4
H460	0.3	6	48.3 ± 8.4	35.0	15.1 ± 2.6
H460	21	0	52.2 ± 7.4	29.8	12.1 ± 1.7
H460	21	6	43.6 ± 6.9	33.1	19.8 ± 3.1
PC3	0.3	0	42.2 ± 3.7	28.5	25.2 ± 2.2
PC3	0.3	6	39.9 ± 3.2	21.7	31.1 ± 2.5
PC3	21	0	50.7 ± 4.6	23.7	20.3 ± 1.6
PC3	21	6	39.6 ± 4.9	22.5	34.7 ± 3.6
H4	0.3	0	61.6 ± 6.0	28.7	5.6 ± 0.42
H4	0.3	6	41.4 ± 5.4	41.2	10.5 ± 1.4
H4	21	0	62.0 ± 5.4	26.3	6.9 ± 0.6
H4	21	6	45.9 ± 6.1	32.1	15.2 ± 2.0

FIGURE 4 | PI spectra of T24, H4, PC3, and H460 72 h after irradiation with 6 Gy compared to no radiation. Within each graph, normoxic (21% O_2) is compared to hypoxic (0.3% O_2) conditions. In all cell lines, irradiation causes a decrease in G1 phase and a relative increase in S and G2/M. The overall survival after irradiation in hypoxia is higher compared to no radiation.

IR and this allowed us to estimate the radiation outcome of most of the treated patients. Indeed, in accordance with what already showed in the past, the study presented here confirms on a genetic level, in *in vitro* conditions, that IR has a profound impact on multiple gene groups. Unfortunately, this is not enough when we consider the environmental role, with the tumor oxygenation state above all.

This need brought us to try to investigate the interplay between IR and oxygen not as two independent parameters but as a couple of dancers instead, where the two entities are moving together forming a new and single new being.

In light of it, we decided to develop and apply a novel mathematical method able to take into consideration the two studied parameters (radiation and oxygen content) per time, "radiation in normoxia" and "radiation in hypoxia," respectively.

After X-ray irradiation at 6 Gy in both normoxia and very hypoxic conditions (0.3%), these new two profiles have been introduced and tested on four different tumor cell lines (brain neuroglioma, lung carcinoma, prostate adenocarcinoma and urinary bladder carcinoma) by means of PCA.

The clustering analysis based on these two new profiles were able to suppress cell line dependent features and highlight only those gene variations derived from "radiation-in-normoxia" and "radiation-in-hypoxia." From the 20,000 genes analyzed, only 37 have shown an important modulation along our mathematical profiles.

These 37 genes included those involved in the immune response and inflammation, ROS defense mechanisms, cell cycle regulation, glucose metabolism and genes involved in the ability to metastatsize (EMT and MET). All of the 37 genes belonging to these groups showed a positive value in both the "radiation in hypoxia" and the "radiation in normoxia" profile. This means that these genes are more likely to experience an up-regulation after irradiation, regardless of the oxygen content, compared to non-irradiated samples. A possible interpretation of this finding is that cells surviving 6 Gy radiation treatment had reduced metastatic potential but showed more resistance. This observation is in accordance to the findings of Ogata et al. (2005). Together with the observed increased immunoresponse, this study stresses the interplay of known metabolic and systemic processes not only in hypoxia or in radiation alone, but also in the combination of those two conditions.

A downregulation in the profiles after irradiation in both oxygen conditions was observed in DNA repair pathways, such as HR and NHEJ. Together with the observed upregulation of SOD2 and HIF1, this leads to the conclusion that cells post-irradiation have to deal with a higher concentration of ROS, which results in the upregulation of SOD2 a well-known ROS scavenging enzyme.

An interesting finding in the presented mathematical profile analysis is that the genes CD274, NOX1, TNF and IL13 showed a clear oxygen dependence: their trend of up- or downregulation after irradiation changed completely depending on the presence or absence of oxygen. As all these genes are involved in immunoresponse, inflammation and cell death, the finding of the mathematical profiles stress the importance of the interplay of both radiation and hypoxia especially with respect to distinct genetic groups.

Regarding cell cycle related genes, the findings presented in the profile study were in accordance with the cell cycle changes checked with propidium iodide after irradiation. This methodical cross check was hence successful.

To conclude, although many questions are still open about the regulation of the 37 genes which came up by using the two novel mathematical profiles, as well as the need to move this kind of study in a mouse model or more complex physiological settings, this study provides a strong evidence about the tight connection, at the gene level, between IR and oxygen in four different cancer cell lines. New gene patterns were reported here regarding the oxygen dependent response of genes after IR. By consequence, new potential gene targets might be used for improving the patient treatment and outcome. Following this way, a much better understanding of the IR response can be reached in the near future.

DATA AVAILABILITY STATEMENT

The datasets presented in this study can be found in online repositories. The names of the repository/repositories and accession number(s) can be found at: EMBL-EBI ArrayExpress [accession: E-MTAB-9571].

AUTHOR CONTRIBUTIONS

The manuscript was written by JJ, PV, LT, and FP. JJ, RH, FP, and LT prepared the experimental samples. MG prepared the samples for genome analysis. JJ performed the cell cycle analysis. The data analysis was done by JJ and PV. The conceptual work was done by JS and JJ. All authors reviewed the manuscript.

FUNDING

ACKNOWLEDGMENTS

SUPPLEMENTARY MATERIAL

The Supplementary Material for this article can be found online at: https://www.frontiersin.org/articles/10.3389/fgene.2021.597635/full#supplementary-material

Supplementary Figure 1 | Boxplot of genes analyzed with qPCR. The expression pattern within the 'radiation-in-normoxia' and 'radiation-in-hypoxia'-profiles is comparable to the pattern found in the whole genome.

REFERENCES

Anam, T., Ishika, A., and Hossain, B. (2015). A meta-analysis of hypoxia inducible factor association with cancers. *Biomarker Res.* 3:29. doi: 10.1186/s40364-015-0054-z

Antonov, A. S., Antonova, G. N., Munn, D. H., Mivechi, N., Lucas, R., Catravas, J. D., et al. (2011). αVβ3 integrin regulates macrophage inflammatory responses via PI3 kinase/Akt-dependent NF-κB activation. *J. Cell Physiol.* 226, 469–476. doi: 10.1002/jcp.22356

Benihoud, K., Esselin, S., Descamps, D., Jullienne, B., Salone, B., Bobe, P., et al. (2007). Respective roles of TNF-a and IL-6 in the immune response-elicited by adenovirus-mediated gene transfer in mice. *Gene Ther.* 14, 533–544. doi: 10.1038/sj.gt.33 02885

Carmeliet, P., Dor, Y., Herbert, J. M., Fukumura, D., Brusselmans, K., Dewerchin, M., et al. (1998). Role of hif-1α in hypoxia-mediated apoptosis, cell proliferation and tumour angiogenesis. *Nature* 394, 485–490. doi: 10.1038/28867

Carvalho, B. S., and Irizarry, R. A. (2010). A framework for oligonucleotide microarray preprocessing. *Bioinformatics* 26, 2363–2367. doi: 10.1093/bioinformatics/btq431

Davis, A. J., and Chen, D. J. (2013). DNA double strand break repair via non-homologous end-joining. *Transl. Cancer Res.* 2, 130–143. doi: 10.3978/j.issn.2218-676X.2013.04.02

Dewhirst, M. W., Cao, Y., and Moeller, B. (2008). Cycling hypoxia and free radicals regulate angiogenesis and radiotherapy response. *Nat. Rev. Cancer* 8, 425–437. doi: 10.1038/nrc2397

Eun, H. S., Cho, S. Y., Joo, J. S., Kang, S. H., Moon, H. S., Lee, E. S., et al. (2017). Gene expression of NOX family members and their clinical significance in hepatocellular carcinoma. *Sci. Rep.* 7:11060. doi: 10.1038/s41598-017-11280-3

Fuster, J. J., and Walsh, K. (2014). The good, the bad, and the ugly of interleukin-6 signaling. *EMBO J.* 33, 1425–1427. doi: 10.15252/embj.201488856

Gray, L., Conger, A., Ebert, M., Hornsey, S., and Scott, O. (1953). The concentration of oxygen dissolved in tissue at the time of irradiation as a factor in radiotherapy. *Br. Inst. Radiol.* 26, 638–648. doi: 10.1259/0007-1285-26-312-638

Hosoki, A., Yonekura, S. I., Zhao, Q. L., Wei, Z. L., Takasaki, I., Tabuchi, Y., et al. (2012). Mitochondria-targeted superoxide dismutase (SOD2) regulates radiation resistance and radiation stress response in HeLa cells. *J. Radiat. Res.* 53, 58–71. doi: 10.1269/jrr.11034

Huang, C. Y., Chiang, S. F., Ke, T. W., Chen, T. W., You, Y. S., Chen, W. T. L., et al. (2018). Clinical significance of programmed infiltration in stage II–III colorectal cancer. *Sci. Rep.* 8:15658. doi: 10.1038/s41598-018-33927-5

Hume, D. A., and Macdonald, K. P. A. (2012). Therapeutic applications of macrophage colony-stimulating factor-1 (CSF-1) and antagonists of CSF-1 receptor (CSF-1R) signaling. *Blood* 119, 1810–1820. doi: 10.1182/blood-2011-09-379214

Iii, R. L. G., Ramalingam, T. R., Hart, K. M., Vannella, K. M., Cantu, D. A., Lu, W., et al. (2019). Interleukin-13 activates distinct cellular pathways leading to ductular reaction, steatosis, and fibrosis. *Immunity* 45, 145–158. doi: 10.1016/j.immuni.2016.06.009

Irizarry, R. A., Hobbs, B., Collin, F., Beazer-Barclay, Y. D., Antonellis, K. J., Scherf, U., et al. (2003). Exploration, normalization, and summaries of high density oligonucleotide array probe level data. *Biostatistics* 4, 249–264. doi: 10.1093/biostatistics/4.2.249

Janeway, C. J., Travers, P., Walport, M., and Shlomchik, M. (2001). *Immunobiology: The Immune System in Health and Disease: The Major Histocompatibility Complex and Its Functions.* New York, NY: Garland Science.

Jiang, Y., Chen, J., Bi, E., Zhao, Y., Qin, T., Wang, Y., et al. (2019). TNF-α enhances Th9 cell differentiation and antitumor immunity via TNFR2-dependent pathways. *J. Immunother. Cancer* 7, 1–12. doi: 10.1186/s40425-018-0494-8

Kim, E., Jung, S., Park, W. S., Lee, J., Shin, R., Heo, S. C., et al. (2019). Upregulation of SLC2A3 gene and prognosis in colorectal carcinoma: analysis of TCGA data. *BMC Cancer* 19:302. doi: 10.1186/s12885-019-5475-x

Kraus, A. C., Ferber, I., Bachmann, S. O., Specht, H., Wimmel, A., Gross, M. W., et al. (2002). *In vitro* chemo-and radio-resistance in small cell lung cancer correlates with cell adhesion and constitutive activation of akt and map kinase pathways. *Oncogene* 21, 8683–8695. doi: 10.1038/sj.onc.1205939

Larsen, J. E., Nathan, V., Osborne, J. K., Farrow, R. K., Deb, D., Sullivan, J. P., et al. (2016). ZEB1 drives epithelial-to-mesenchymal transition in lung cancer. *J. Clin. Invest.* 126, 3219–3235. doi: 10.1172/JCI76725

Li, X., and Heyer, W. D. (2008). Homologous recombination in DNA reapir and DNA. *Cell Res.* 18, 99–113. doi: 10.1038/cr.2008.1

Liu, C., Lin, Q., and Yun, Z. (2015). Cellular and molecular mechanisms underlying oxygen-dependent radiosensitivity. *Radiat. Res.* 183, 487–496. doi: 10.1667/RR13959.1

McInroy, L., and Määttä, A. (2007). Down-regulation of vimentin expression inhibits carcinoma cell migration and adhesion. *Biochem. Biophys. Res. Commun.* 360, 109–114. doi: 10.1016/j.bbrc.2007.06.036

McKelvey, K. J., Hudson, A. L., Back, M., Eade, T., and Diakos, C. I. (2018). Radiation, inflammation and the immune response in cancer. *Mammal. Genome* 29, 843–865. doi: 10.1007/s00335-018-9777-0

McKeown, S. (2014). Defining normoxia, physoxia and hypoxia in tumours—implications for treatment response. *Br. J. Radiol.* 87:20130676. doi: 10.1259/bjr.20130676

Miao, L., and St. Clair, D. K. (2009). Regulation of superoxide dismutase genes: implications in disease. *Free Radic. Biol. Med.* 47, 344–356. doi: 10.1016/j.freeradbiomed.2009.05.018

Minty, A., Chalon, P., Derocq, J. M., Dumont, X., Guillemot, J. C., Kaghad, M., et al. (1993). lnterleukin-13 is a new human lymphokine regulating inflammatory and immune responses. *Nature* 362, 248–250. doi: 10.1038/362248a0

Musgrove, E. A., Caldon, C. E., Barraclough, J., Stone, A., and Sutherland, R. L. (2011). Cyclin D as a therapeutic target in cancer. *Nat. Rev. Cancer* 11, 558–572. doi: 10.1038/nrc3090

Ogata, T., Teshima, T., Kagawa, K., Hishikawa, Y., Takahashi, Y., Kawaguchi, A., et al. (2005). Particle irradiation suppresses metastatic potential of cancer cells. *Cancer Res.* 65, 113–121.

Park, M. H., Kim, S. Y., Kim, Y. J., and Chung, Y. H. (2014). ALS2CR7 (CDK15) attenuates TRAIL induced apoptosis by inducing phosphorylation of survivin Thr34. *Biochem. Biophys. Res. Commun.* 450, 129–134. doi: 10.1016/j.bbrc.2014.05.070

Sauter, K. A., Waddell, L. A., Lisowski, Z. M., Young, R., Lefevre, L., Davis, G. M., et al. (2016). Macrophage colony-stimulating factor (CSF1) controls monocyte production and maturation and the steady-state size of the liver in pigs. *Am. J. Physiol. Gastrointest. Liver Physiol.* 311, G533–G547. doi: 10.1152/ajpgi.00116.2016

Smith, T. G., Robbins, P. A., and Ratcliffe, P. J. (2008). The human side of hypoxia-inducible factor. *Br. J. Haematol.* 141, 325–334. doi: 10.1111/j.1365-2141.2008.07029.x

Stanca, E., Serviddio, G., Bellanti, F., Vendemiale, G., Siculella, L., and Maria, A. (2013). Down-regulation of LPCAT expression increases platelet-activating factor level in cirrhotic rat liver: potential antiinflammatory effect of silybin Eleonora. *Biochim. Biophys. Acta* 1832, 2019–2026. doi: 10.1016/j.bbadis.2013.07.005

Suzuki, K., Ojima, M., Kodama, S., and Watanabe, M. (2003). Radiation-induced dna damage and delayed induced genomic instability. *Oncogene* 22, 6988–6993. doi: 10.1038/sj.onc.1206881

Tanaka, T., Narazaki, M., and Kishimoto, T. (2014). IL-6 in inflammation, immunity, and disease. *Cold Spring Harbor Perspect. Biol.* 6:a016295. doi: 10.1101/cshperspect.a016295

Tang, Y., Geng, Y., Luo, J., Shen, W., Zhu, W., Meng, C., et al. (2015). Downregulation of ubiquitin inhibits the proliferation and radioresistance of non-small cell lung cancer cells *in vitro* and *in vivo*. *Sci. Rep.* 5:9476. doi: 10.1038/srep09476

Thoday, J., and Read, J. (1947). Effect of oxygen on the frequency of chromosome aberrations produced by X-rays. *Nature* 160, 608–608. doi: 10.1038/160608a0

Watson, J. V., Chambers, S. H., and Smith, P. J. (1987). A pragmatic approach to the analysis of DNA histograms with a definable G1 peak. *Cytometry* 8, 1–8. doi: 10.1002/cyto.990080101

World Health Organization (2021). *Key Statistics.* Available online at: https://www.who.int/cancer/resources/keyfacts/en/ (accessed March 18, 2021).

Wu, J., Wang, H. T., Huang, X. F., Lei, X. L., Lu, Q. K., and Jin, Z. B. (2015). Molecular screening of the LPCAT1 gene in patients with retinitis pigmentosa without defined mutations in known retinitis pigmentosa genes. *Mol. Med. Rep.* 12, 5983–5988. doi: 10.3892/mmr.2015.4204

Zhao, X., Wei, C., Li, J., Xing, P., Li, J., Zheng, S., et al. (2017). Cell cycle-dependent control of homologous recombination. *Acta Biochim. Biophys. Sin.* 49, 655–668. doi: 10.1093/abbs/gmx055

Zheng, W., Gu, X., Sun, X., and Hu, D. (2019). Effects of hypoxia-inducible factor-1α on the proliferation and apoptosis of human synovial mesenchymal stem cells. *Mol. Med. Rep.* 20, 4315–4322. doi: 10.3892/mmr.2019.10656

Zölzer, F., and Streffer, C. (2002). Increased radiosensitivity with chronic hypoxia in four human tumor cell lines. *Int. J. Radiat. Oncol. Biol. Phys.* 54, 910–920. doi: 10.1016/S0360-3016(02)02963-2

Conflict of Interest: The authors declare that the research was conducted in the absence of any commercial or financial relationships that could be construed as a potential conflict of interest.

P.III: Iron and copper complexes with antioxidant activity as inhibitors of the metastatic potential of glioma cells

Authors: Joana Guerreiro, Marco António Gomes, Francesca Pagliari, **Jeannette Jansen**, Maria Grazia Marafioti, Clelia Nisticò, Rachel Hanley, Rafael Costa, Sarah Ferreira, Filipa Mendes, Christiane Fernandes, Adolfo Horn, Luca Tirinato, Joao Seco

Contributions: JG and MG contributed equally. CAT and SOD mimicking compounds were developed by MG. The necessary experiments were performed by **JJ** together with JG, FP, MM, CN and RH. One critical aspect of the effect of the compounds was to determine if and how the distribution of the cells in the cell cycle had changed. This step was performed by **JJ**, including sample preparation, data acquisition, processing, analysis and interpretation.

Check for updates

Iron and copper complexes with antioxidant activity as inhibitors of the metastatic potential of glioma cells†

Joana F. Guerreiro, ‡[ab] Marco Antônio G. B. Gomes, ‡[a] Francesca Pagliari, *[a] Jeannette Jansen, [ac] Maria G. Marafioti,[a] Clelia Nistico, [a] Rachel Hanley, [ac] Rafael O. Costa, [d] Sarah S. Ferreira,[e] Filipa Mendes,[b] Christiane Fernandes, [f] Adolfo Horn,[f] Luca Tirinato [ag] and Joao Seco *[ac]

Gliomas are the most common type of primary brain tumors, presenting high mortality and recurrence rates that highlight the need for the development of more efficient therapies. In that context, we investigated iron(III) (FeL) and copper(II) (CuL) complexes containing the tetradentate ligand 2-{[(3-chloro-2-hydroxy-propyl)-pyridin-2-ylmethyl-amino]-methyl}-phenol (L) as potential antimetastatic compounds in glioma cells. These complexes were designed to act as mimetics of antioxidant metalloenzymes (catalases and superoxide dismutase) and thus interfere with the production of reactive oxygen species (ROS), important signaling molecules that have been linked to the induction of Epithelial–Mesenchymal Transition (EMT) in cancer cells, a process associated with cancer invasion and aggressiveness. The results obtained have revealed that, *in vitro*, both compounds act as superoxide dismutase or catalase mimetics, and this translated in glioma cells into a decrease in ROS levels in FeL-treated cells. In addition, both complexes were found to inhibit the migration of monolayer-grown H4 cells and lead to decreased expression of EMT markers. More importantly, this behavior was recapitulated in 3D spheroids models, where CuL in particular was found to completely inhibit the invasion ability of glioma cells, with or without cellular irradiation with X-rays, which is suggestive of these compounds' potential to be used in combination with radiotherapy. Overall, the results herein obtained describe the novel use of these complexes as agents that are able to interfere with regulation of EMT and the invasive behavior of glioma cells, an application that deserves to be further explored.

[a]Biomedical Physics in Radiation Oncology, German Cancer Research Center (DKFZ), Im Neuenheimer Feld 223, 69120 Heidelberg, Germany. E-mail: f.pagliari@dkfz-heidelberg.de/j.seco@dkfz-heidelberg.de; Tel: +49 6221 42 2554

[b]Departamento de Engenharia e Ciências Nucleares e Centro de Ciências e Tecnologias Nucleares, Instituto Superior Técnico, Universidade de Lisboa, Estrada Nacional 10 (km 139.7), 2695-066 Bobadela LRS, Portugal

[c]Department of Physics and Astronomy, Heidelberg University, Im Neuenheimer Feld 227, 69120 Heidelberg, Germany

[d]Laboratório de Ciências Química, Universidade Estadual do Norte Fluminense (UENF), Av. Alberto Lamego, 2000, Campos dos Goytacazes, RJ, 28013602, Brazil

[e]Instituto Federal Fluminense (IFF), R. Dr Siqueira, 273, Campos dos Goytacazes, RJ CEP 28030-130, Brazil

[f]Departamento de Química, Universidade Federal de Santa Catarina (UFSC), Campus Universitário Trindade, 88040900 Florianópolis, SC, Brazil

[g]BioNEM Laboratory, Department of Experimental and Clinical Medicine, Magna Graecia University of Catanzaro, 88100 Catanzaro, Italy

† Electronic supplementary information (ESI) available. See DOI: 10.1039/d0ra00166j

‡ Equally contributing authors.

Introduction

The most common primary malignant brain tumors in adults are gliomas, which correspond to about 80% of all the malignant brain tumors diagnosed.[1] The treatment of gliomas varies according to the degree of the disease and the patient's condition, but the current standard of treatment includes surgery for maximum resection of the tumor, followed by radiotherapy and chemotherapy.[1] However, achieving complete resection of the tumor is often impossible due to its highly infiltrating nature and inaccessible location, leading to recurrence of the disease in the great majority of cases.[1] In addition, while metastases outside of the central nervous system are uncommon, when present, they often exhibit increased resistance to treatment, similarly to what is observed for relapsed tumors, leading to a very poor prognosis for these patients.[1–3] As such, it is necessary to develop more efficient therapeutic tools that can improve the patients' outcome.

Research exploring metal based compounds as chemotherapeutic drugs for the treatment of cancer has increased since the discovery of cisplatin-based chemotherapy.[4,5] Metal

complexes present many versatile characteristics, such as their redox activity, diverse reactivity with organic substrates, and different coordination modes that make them attractive tools to be explored in the design of new chemotherapeutic drugs.[4,5] In addition to the development of cytotoxic chemotherapeutic drugs, the interest on metal complexes that can be used as metastasis inhibitors has also increased in recent years.[5-7] For this purpose, most of the studies done so far have largely been focused on promising ruthenium-based compounds,[6,8-10] even though complexes containing other metals have also been described.[11,12] Currently, however, only two ruthenium compounds have advanced into clinical trials, although they've failed to show the desired therapeutic efficacy that would make them viable alternative to the therapies currently in use.[13]

Antimetastatic complexes can target different cellular pathways or processes, but have mainly been designed to modulate or interfere with key features necessary for cancer migration or invasion. One such feature is the modulation of the Epithelial–Mesenchymal Transition (EMT) phenomenon,[9] a physiological process involved in the cellular developmental program and tissue repair, but which has been also strongly linked to the metastatic process in cancer.[14] Namely, during EMT, cancer cells undergo a series of changes (biochemical, morphologic and genetic) that allow them to have a more mesenchymal-like phenotype that is thought to be necessary to promote cancer cell migration and invasion, and their escape from the primary tumor.[14] Despite the fact that the search for compounds able to interfere with the EMT process has been increasing in the past years, it is still mainly based in the use of natural compounds isolated from plants,[15] while the use of metal-based compounds in this branch of medicinal chemistry remains poorly researched. In addition to targeting EMT, several of these metal-based compounds also aim to affect Reactive Oxygen Species (ROS) equilibrium[8,11,12,16] since ROS can act as signaling molecules in many cellular pathways, including those involved in tumor progression.[17] Interestingly, the EMT process seems to be connected to cellular ROS levels and different metals have been shown to induce EMT in different cancers through a ROS-dependent mechanism.[18-21] As such, modulation of ROS levels in cancer cells has been put forth as another promising strategy to tackle the problem of local invasiveness and metastization of cancer.[22]

One possible strategy to modulate the levels of cellular ROS, and, consequently, the cancer cells metastatic ability, is the use of metal-based compounds that mimic the superoxide dismutase (SOD) and catalase (CAT) enzymes, important cellular antioxidant proteins that are responsible for maintaining the cellular redox balance.[22] For that purpose, in this work, we used two coordination compounds harboring the ligand 2-{[(3-chloro-2-hydroxy-propyl)-pyridin-2-ylmethyl-amino]-methyl}-phenol (L) complexed with iron (FeL)[23,24] and copper (CuL).[25] We thus describe for the first time the application of these compounds in the frontier of chemistry and human oncology, by assessing their antioxidant and antimetastatic potential in glioma (H4) cells. The results obtained have revealed an impressive ability of the compounds under study to inhibit the migration of H4 glioma cells in both 2D and 3D cellular models.

In addition, this effect was maintained after irradiation with X-rays, suggesting that these compounds might be suitable to be used as co-adjuvants for radiotherapeutic treatments.

Results and discussion

Cytotoxicity of FeL and CuL compounds in H4 glioma cells

The synthesis of the ligand 2-{[(3-chloro-2-hydroxy-propyl)-pyridin-2-ylmethyl-amino]-methyl}-phenol (L) and of the iron and copper complexes studied here were described previously by us.[23-26] The ligand contains four coordinating groups (N_2O_2) and its coordination behavior depends on the metal center. For example, it forms dinuclear phenoxo bridge complexes with Ni(II),[27] while with Fe(III), mononuclear and dinuclear (alkoxo bridge) were already described.[23,24] The iron compound described here shows a dinuclear structure (Fig. 1), in which the iron(III) ions are connected by two alkoxo bridges from two ligand molecules. The coordination environment is completed by two nitrogen atoms (the tertiary N atom and one from the pyridyl group), one oxygen from the phenolate unit and a water molecule. It has been shown that this compound is able to promote DNA cleavage.[23] Concerning the copper complex, its molecular structure solved by monocrystal X-ray analysis showed the presence of two distinct species in the crystal, a mononuclear and a dinuclear one,[25] shown in Fig. 1. The dinuclear species may be considered the dimer of the mononuclear one and studies showed that the dinuclear species is transformed in the mononuclear one in solution, and, therefore, only the mononuclear species remains. It has been previously demonstrated that the copper complex shows cytotoxicity on pathogenic bacteria.[25]

In order to determine if the FeL and CuL complexes (Fig. 1A) exhibited significant antitumoral properties, their cytotoxic activity after 24 hours (h) of treatment was determined in H4 glioma cells using the AlamarBlue assay. Both compounds were found to have IC_{50} values in the high micromolar range (85 ± 1 and 82 ± 1 μM for FeL and CuL, respectively; ESI Fig. 1†), indicating that they display only moderate cytotoxicity in glioma cells. In fact, these compounds exhibited about 40% less cytotoxicity than the one previously reported for the reference chemotherapeutic drug cisplatin (50 μM) in this same cancer cell line after 24 h of incubation.[28] Since we were not interested in evaluating the intrinsic cytotoxic activity of the compounds, but how their antioxidant activity may influence other properties of cancer cell development, the lack of cytotoxic effect is of relevance for the present study. As such, we selected a concentration of the compounds that did not induce significant loss of viability (25 μM; Fig. 1B) to further proceed with the evaluation of these compounds as antimetastatic agents, while minimizing potential interference from cytotoxic effects exerted by the drugs. Due to the lack of a proper non-malignant control brain cell line, this study did not consider the effects of the tested compounds on healthy brain cells. Although we acknowledge that this aspect can be of particular interest, it is currently beyond the scope of this study and, therefore, it will be further investigated in the future.
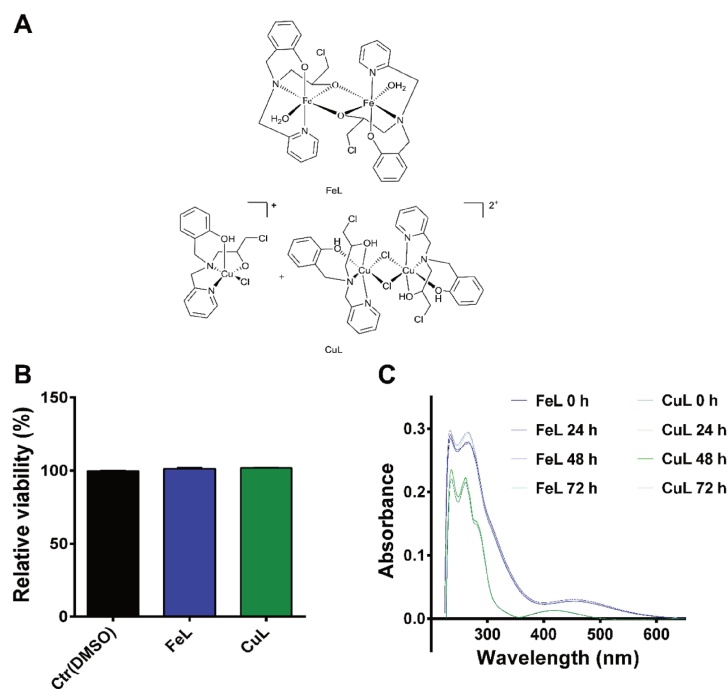
Paper

Fig. 1 FeL and CuL complexes exhibit relatively low cytotoxicity in H4 glioma cells. (A) Chemical structure of the FeL and CuL compounds. (B) Cellular viability of H4 cells after 24 h of incubation with 25 μM of FeL and CuL (and the respective solvent) as compared to the control (Ctr) and determined by propidium iodide flow cytometric assay. The results were calculated from three independent experiments and are given as the mean ± S.E.M. (C) FeL and CuL stability in PBS after 24 h, 48 h, or 72 h of incubation with 25 μM of the compound, determined by UV-VIS spectrometry.

Stability studies by UV-Vis spectrometry indicated that both compounds were stable at the selected concentration in a PBS solution at physiological pH for up to 72 h of incubation (Fig. 1C), the latest time point used for our assays. For the iron compound, it was also possible, using a higher concentration of FeL (50 μM), to visualize through confocal fluorescence microscopy the presence of a fluorescent species in the lysosomes, suggesting that it was indeed entering the cells under these conditions (ESI Fig. 2†). On the other hand, no signal was observed for the copper compound.

In vitro and cellular antioxidant properties of FeL and CuL

Based on the important role that transition metal ions play in cellular redox mechanisms, several studies having metalloenzymes, such as SOD and CAT, as targets for new mimetic compounds have been performed.[29–32] Within this approach, in recent years, our group has developed different ligands and their respective coordination compounds with different transition metals, that exhibit antioxidant properties.[29,33–35] For example, we have shown that copper, iron and manganese complexes with the ligand 1-[bis(pyridin-2-ylmethyl)amino]-3-chloropropan-2-ol (L1), similar to the one reported here, but

with two pyridine groups instead of a pyridine and a phenol group, present protective antioxidant effects on *Saccharomyces cerevisiae* cells subjected to oxidative stress.[33] These results thus prompted us to investigate the antioxidant activity of this set of compounds (FeL and CuL) and evaluate if their antioxidant activity could exert any influence on biological processes, particularly on the migratory ability of cancer cells.

To address if the compounds FeL and CuL displayed antioxidant activities, we first assessed their ability to mimic the SOD enzyme *in vitro*. Both compounds reacted with the superoxide anion (ESI Fig. 3, 4 and Table 1†) as evidenced by the IC_{50} values obtained, which represent the concentration of the compound required to inhibit half of the reduction of nitrobluetetrazolium (NBT) by the superoxide anion generated *in situ* at a constant rate by the enzymatic system xanthine/xanthine oxidase, in comparison to control conditions.

In order to show SOD-like activity, the compounds have to be able to promote the oxidation ($O_2^{\bullet-} \rightarrow O_2 + e^-$) and the reduction ($O_2^{\bullet-} + e^- \rightarrow O_2^{2-}$) of the superoxide anion. This behavior is shown by systems that catalytically induce the superoxide decomposition. If the system promotes only the reduction or only the oxidation of the superoxide anion, they will work as

superoxide reductase or superoxide oxidase, respectively. In light of this, the compounds described here would react only stoichiometrically with the superoxide anion. Thus, considering the difference (71 nmol) between the number of moles of formazan formed in the presence and in the absence of CuL and the number of moles of the copper complex (2.0 nmol) employed in the assay that showed the lower formation of formazan (Fig. 1 ESI†), each molecule of the copper complex was able to react with 35 molecules of superoxide anion after 40 min, clearly suggesting catalytic activity. On the other hand, since the iron complex was less active, the reaction ratio superoxide : FeL was only 1.5 after 40 min. Since this ratio is only a little bit higher than the stoichiometric reaction, at the moment it is not possible to conclude if FeL showed SOD or SOO activity. Therefore, CuL was found to possess a higher reactivity on the superoxide anion (almost 50 times higher) than the FeL compound and due to its catalytic activity it might be considered as presenting SOD-like activity. However, the K_{cat} obtained for CuL is $ca.$ 1.8×10^2 lower than the one observed for the natural SOD. Comparing the data with the complexes synthesized with the ligand L1 (Table 1), the activities obtained here were of the same order of magnitude.

Next, the ability of the complexes to mimic the enzyme CAT was evaluated through a direct reaction with hydrogen peroxide (H_2O_2), which was monitored by measuring H_2O_2 absorption using electronic spectroscopy at 240 nm. The FeL complex showed CAT mimetic activity in phosphate buffer solution (pH 7.8), while the CuL complex exhibited CAT-like activity only when one co-catalyst (piperazine) was added to the reaction (Table 1). Once again, the kinetic parameters calculated for both compounds, in particular the K_{cat}, revealed that CuL possesses higher CAT-like activity than FeL, albeit limited by the need of the addition of the mentioned co-catalyst.

Following the results obtained with the *in vitro* enzymatic assays, we then proceeded to determine the ROS levels in H4 glioma cells incubated with the 2 complexes. For that, we used CM-H_2DCFDA-based flow cytometry which is useful to detect several ROS species, but mainly H_2O_2, the hydroxyl radical (OH$^{\bullet}$) or peroxynitrite.[38] Cellular treatment with FeL for 24 h induced a statistically significant reduction in ROS levels (Fig. 2A). In contrast, CuL led to an evident, but not statistically significant, decrease in ROS levels (Fig. 2A). These results

indicate that the *in vitro* antioxidant activity is not translated in the cellular environment. This behavior has been described previously when the *in vitro* SOD/CAT activity of Fe, Cu and Mn of similar mimetic complexes was not replicated in live cells.[33]

To assess if the complexes antioxidant effects might also be due to indirect instead of direct effects, we assessed the level of expression of several ROS-related genes by qPCR. The vehicle control sample, treated with DMSO, exhibited a clear effect on the expression of some of the genes analysed (Fig. 2B), which is in agreement with the fact that DMSO has been previously described to be a ROS scavenger, able to interfere with several related cellular processes,[39] even if under our experimental conditions we saw no significant changes in ROS levels in DMSO-control cells in the cytometric study (Fig. 2A). From the results obtained, however, it became evident that both treatment with FeL and CuL led to a considerable upregulation of the expression of thiorredoxin (Fig. 2B), Trx1, an important cytosolic detoxifying protein,[40] which suggests that these compounds might have an impact on the homeostasis of cytosolic redox status. Additionally, the FeL compound also led to significant changes in SOD1 and CAT expression levels when compared with DMSO-treated cells (Fig. 2B), which is in accordance to the fact that it induced a significant decrease in ROS levels (Fig. 2A) and might contribute to its apparently higher antioxidant effect when compared with CuL. In addition to having an effect on intracellular ROS levels, we cannot rule out the possibility that the complexes used are also altering extracellular ROS levels. These species have been hypothesized to be extremely relevant players in the tumor microenvironment and different aspects of cancer progression, including the development of metastasis,[41] and, as such, this possibility is worthy of further investigation in the future.

FeL and CuL complexes reduce migration through inhibition of epithelial–mesenchymal transition (EMT) in glioma cells

Since an increase in ROS had been previously implicated in EMT induction in different cells,[18–21] we hypothesized that the reduction in ROS levels induced by the compounds could be leading to changes in the metastatic ability of H4 cells. The effect of FeL and CuL on the migration of H4 cells was thus investigated by the transwell migration assay. The number of

Table 1 Kinetic parameters of iron and copper complexes and natural SOD and CAT enzymes

Compound	SOD activity		CAT activity			Ref.
	IC$_{50}$ (µM)	K_{cat} (M^{-1} s^{-1})	K_{cat} (s^{-1})	K_M (mM)	K_{cat}/K_M (M^{-1} s^{-1})	
FeL^a	8.946 ± 0.345	1.43×10^5	0.080 ± 0.003	23.2 ± 1.2	3.45 ± 0.04	This work
CuL	0.181 ± 0.016	7.07×10^6	0.360 ± 0.125	41.9 ± 15.7	8.25 ± 0.06	This work
FeL1^b	26.8 ± 2.5	1.2×10^5	ND	ND	ND	Ribeiro *et al.*[33]
CuL1^b	0.43 ± 0.2	7.7×10^6	NA	NA	NA	Riberio *et al.*[33]
Cu, Zn-SOD	0.03	1.3×10^9	—	—	—	Weser *et al.*[36]
CAT (human erythrocytes)	—	—	5.87×10^5	80	7.34×10^6	Switala *et al.*[37]

^{a} The kinetic data do not allow to confirm if the compound shows superoxide dismutase or superoxide oxidase activity. ^{b} L = *N*-(2-hydroxybenzyl)-*N*-(2-pyridylmethyl)[(3-chloro)(2-hydroxy)]propylamine; L1 = 1-[bis(pyridin-2-ylmethyl) amino]-3-chloropropan-2-ol; ND = not determined; NA = not active.
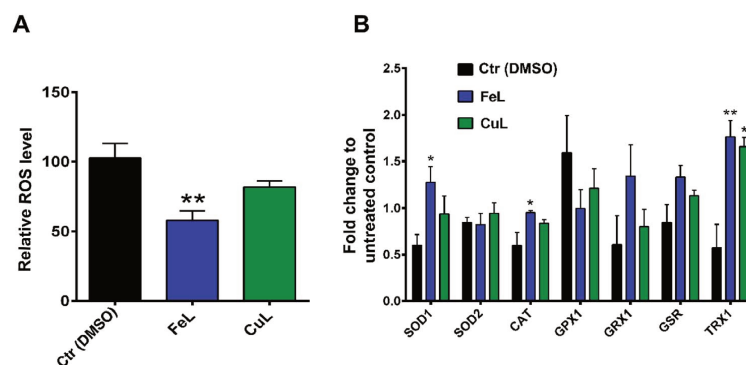
Paper

Fig. 2 FeL and CuL complexes exhibit antioxidant properties in H4 glioma cells. (A) ROS levels in H4 cells after incubation with 25 μM of FeL and CuL (or 0.125% DMSO) for 24 h in relation to a control containing just growth medium. (B) Gene expression of ROS-related genes in H4 cells after incubation with 25 μM of FeL and CuL for 24 h. Results are shown as fold change normalized to the untreated control (Ctr) and represent the mean ± S.E.M of three independent replicas. Statistical significance was calculated using one-way ANOVA, followed by Dunnet's test ($*p \leq 0.05$, $**p \leq 0.01$) in comparison to the DMSO control.

cells migrated to the bottom of the membrane revealed that both complexes can clearly inhibit the migratory ability of H4 cells (Fig. 3A).

To investigate to what extent this observation was related to cell proliferation or cell cycle arrest induction, since ROS has also been shown to be related with regulation of cellular proliferation/cell cycle,[42] the effects of the compounds on the cell cycle of H4 cells were investigated by flow cytometry. While FeL showed no effect on the cell cycle of H4 cells, CuL induced a significant decrease in the G0/G1 phase of the cycle ($*p \leq 0.05$), with a concomitant increase in the % of cells in the S and G2/M phases (of about 7.7 and 6.2%, respectively) that was, however, statistically not significant (Fig. 3B). This suggests that CuL-treated cells might experience a shift in the cell cycle from the G0/G1 phase to the S and G2/M phases, which could either reflect a slight increase in proliferation, or that cells are arrested during DNA duplication or prior to cell division.[43] However, this difference does not seem likely to justify the significant change observed in the migration of glioma cells upon exposure to the complex.

As such, looking for another possible explanation, we next analyzed the expression of several EMT markers in the FeL/CuL treated cells by qPCR. The results evidenced that treatment with the compounds is accompanied by an obvious and statistically significant increase in expression of E-cadherin mRNA, and a slight, but not significant, reduction of Vimentin in the case of CuL (Fig. 3C). The expression of the EMT-related transcription factor Snail was found to also be statistically significantly decreased upon treatment with CuL (Fig. 3C). This gene expression profile is consistent with the hypothesis that cells treated with FeL and CuL had a more epithelial-like phenotype, possibly experiencing an inhibition of the EMT transition process, which should originate cells with a less motile phenotype,[14] and is in accordance with the decreased migratory ability observed in complex-treated cells (Fig. 3A),

demonstrating that the compounds do seem to possess anti-metastatic properties.

FeL and CuL complexes inhibit 3D spheroids invasion

There is mounting evidence that the results obtained in 2D cellular models, where many of the characteristics of the original tumor microenvironment are missing, present several limitations when being transposed into the clinical setting.[44] In that context, several 3D cellular models have been developed that present a level of complexity which is much closer and more representative of several aspects of tumor tissues than the ones shown by monolayer cell cultures.[44] In particular, matrix-embedded 3D cultures have been increasingly applied to investigate tumor migration and invasion.[45]

As such, and in order to try to better estimate the clinical translational potential of the compounds under evaluation, we extended our studies to H4 multicellular spheroids, which are expected to better recapitulate *in vivo* tumor properties. For that purpose, spheroids generated in agarose-coated plates were first treated with FeL or CuL for 24 h or 72 h. Then, cell viability was assessed using the CellTiter-Glo® 3D assay, while spheroid size and growth were accompanied using bright field microscopy. Surprisingly, incubation with FeL increased cellular viability (Fig. 4A), both after 24 h and 72 h of incubation. This increase in viability was accompanied by an increase in spheroid size after 72 h of incubation (Fig. 4B). In contrast, CuL induced a decrease in viability as early as 24 h of incubation, along with a concomitant decrease in spheroid size (Fig. 4A and B).

Next, we observed that both complexes were able to interfere with the invasive behavior exhibited by H4 cells embedded in matrigel (Fig. 4C). CuL, in particular, exhibited very encouraging results, completely eliminating H4 cell ability to invade the matrigel matrix, an effect that cannot be attributed solely to the decrease in viability and growth found to occur following incubation with this compound (around 31% and 19% in terms
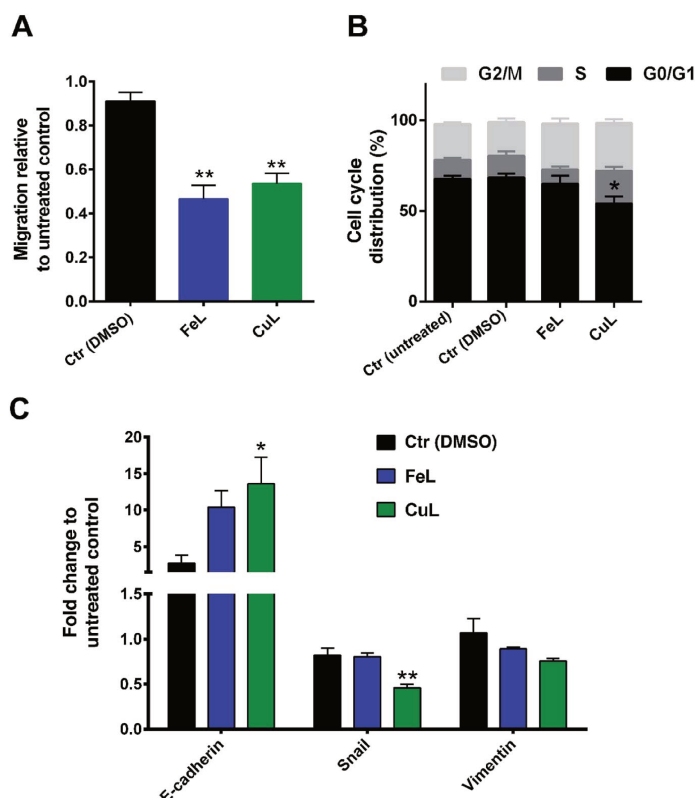
Fig. 3 FeL and CuL complexes reduce migration and inhibit Epithelial–Mesenchymal Transition (EMT) in H4 glioma cells. (A) Migration of H4 cells after 24 h of incubation with 25 μM of FeL and CuL assessed with the transwell migration assay. (B) Cell cycle analysis and (C) expression of EMT marker genes in H4 cells under those same conditions. The results were calculated from three independent experiments and are given as the mean ± S.E.M. Statistical significance was calculated using one-way ANOVA, followed by Dunnet's test (*$p \leq 0.05$, **$p \leq 0.01$) in comparison to the DMSO control.

of cellular viability and growth, respectively). FeL also displayed the ability to inhibit the invasive behavior of H4 cells, an effect that was, however, not as striking as the one found for CuL. However, this can be due to the fact that this compound was found to present a stimulatory effect in cellular viability, as described above (Fig. 4A and B), counteracting the desirable effect it seemed to also have as an anti-metastatic compound.

Notably, the effect of the compounds on H4 spheroids' invasive ability was maintained even when cells were irradiated with X-rays (6 Gy). This is highly relevant in the clinical context, since it has been demonstrated that the use of low linear energy transfer (LET) irradiation, which includes X-rays radiation, might, in patient-specific contexts, increase migration and invasion of glioma cells.[46] In addition, most glioma relapses occur in an area within 2 cm of the area where the primary tumor initially developed, which impairs tumor removal and local radiotherapy.[2] The results obtained in the 3D invasion assays thus clearly demonstrate that both complexes possess an anti-metastatic effect not only in monolayer cells, but also in the more representative spheroids model that has potential to be highly relevant in the clinical context.

FeL and CuL complexes alter glutathione metabolism or oxidative stress in H4 spheroids

Since we had previously observed an apparent decrease in ROS levels in complex-treated cells that could be related to the decreased migration observed in monolayer-cultured cells, we investigated whether the remarkable effect of the compounds on the inhibition of H4 spheroids' invasion in matrigel could be also related with changes in cellular oxidative stress in this 3D cellular model. For that, the antioxidant ability of the complexes was assessed by determining the relative levels of cellular glutathione and the ratio of reduced glutathione (GSH), an important cellular antioxidant and detoxifying agent, and oxidized glutathione (GSSG) using the GSH/GSSG-Glo™ Assay.
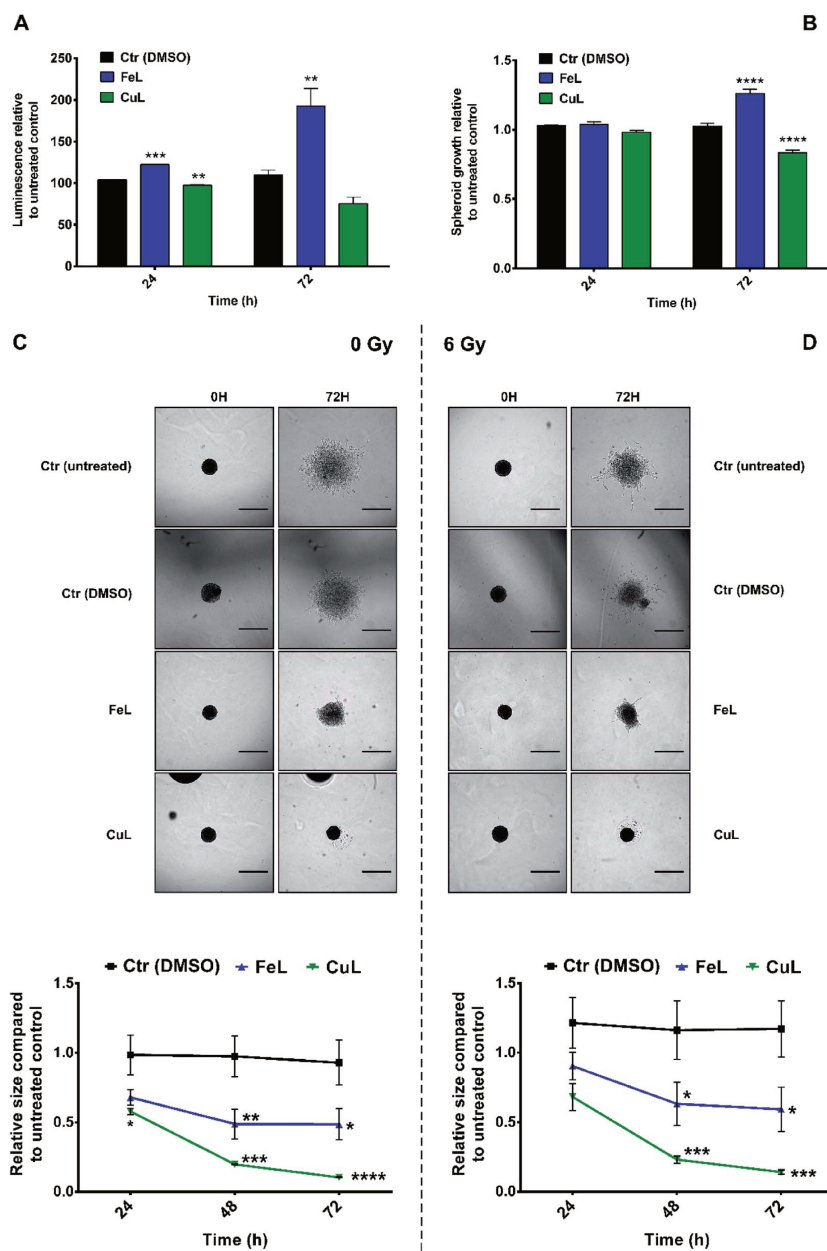
Paper   **RSC Advances**

Fig. 4   FeL and CuL complexes inhibit H4 spheroids invasion. Viability (A) and growth (B) of H4 spheroids after 24 h and 72 h of incubation with 25 μM of FeL and CuL. Representative images and quantification of the invasion of H4 spheroids after 24 h and 72 h of incubation with 25 μM of FeL and CuL without (Ctr) or with irradiation with 6 Gy X-rays (D). Scale bars, 500 μm. Statistical significance was calculated using one-way ANOVA (for (A and B)) or two-way ANOVA (for (C and D)), followed by Dunnet's test ($*p \leq 0.05$, $**p \leq 0.01$, $**p \leq 0.001$, $****p \leq 0.0001$) in comparison to the DMSO control. Experiments were performed in at least duplicates (A and B) or triplicates (C and D), using multiple spheroids per condition in each replicate done.

The results obtained revealed that treatment with FeL induced an increase in GSH levels, while the GSH/GSSG ratio remained unchanged (Fig. 5A and B, respectively). This suggests that this compound did not change the oxidative stress levels in H4 spheroids, but it seemed to affect cellular glutathione metabolism. Contrastingly, cells treated with the CuL complex showed an evident decrease of the GSH/GSSG ratio, compared with the vehicle control sample, which indicates that CuL was inducing oxidative stress under these conditions (Fig. 5B). In addition, the level of total GSH in these cells was also found to be reduced (Fig. 5A).

These observations raise the question of what might be the impact of such metabolic changes on the behavior observed for FeL- and CuL-treated H4 spheroids. One possibility is that the elevated oxidative stress found in CuL-treated cells could underlie the decrease in viability observed under these same conditions (Fig. 4A and B), since several metal-based compounds have been previously described to reduce cancer cell viability through the induction of ROS production.[8,11,12] Moreover, increased GSH levels have also been previously correlated with enhanced cancer metastatic ability.[47] This could, at least partially, explain the difference in performance observed for the FeL and CuL compounds, since the later significantly decreases GSH levels and is much more efficient at reducing the invasive potential of H4 spheroids, while the former actually increased the GSH levels, exhibiting a less pronounced inhibitory effect. Overall, these results are highly encouraging, since modulation of GSH levels have been proposed as a potential way to sensitize tumor cells to treatment modalities such as chemotherapy,[47] and, in particular the CuL complex, seems to be a good candidate to test this goal, while also having been proved herein to have a significant impact on the cell invasive ability.

Conclusion

The highly infiltrative nature of gliomas poses significant therapeutic challenges that result in a high rate of disease recurrence and poor patient prognosis. In this work, we explored the application of two coordination compounds, FeL and CuL in an anticancer therapeutic context. Both complexes showed antioxidant activity (catalase and superoxide dismutase/superoxide oxidase) *in vitro* and, in the case of FeL, also in H4 glioma cells. Although the complexes did not present significant cytotoxic activity at 25 µM, they exhibited anti-migratory properties in 2D cultures and anti-invasive abilities in 3D multicellular spheroids. While the mechanisms underlying these effects have not been fully elucidated, they seem to be related with cellular oxidative stress and/or glutathione metabolism, particularly in 3D cellular models where the best performing complex, CuL, caused a reduction in GSH levels, which has been previously correlated with increased metastatic properties of cancer cells. Importantly, the concentrations of the compounds tested were not cytotoxic in 2D models or only slightly affected the viability in 3D models, which indicates that the occurrence of extensive cell death is not behind the changes in migratory/invasive ability. Additionally, this suggests that they might also be less toxic to healthy cells, which would result in less treatment side-effects. Considering that recent reports have also proposed that glioma therapy needs to be developed in the context of a potential detrimental enhancement of cancer invasion by radiotherapeutic treatments, our complexes also revealed a decrease in H4 cells invasion when combined with irradiation with x-rays. This is highly relevant, as it indicates that they do have high potential to limit the cancer invasive ability and might be used in combination with other anti-proliferative therapies.

Experimental section

Synthesis of complexes, preparation of stock solutions and stability

The ligand 2-{[(3-chloro-2-hydroxy-propyl)-pyridin-2-ylmethyl-amino]-methyl}-phenol (L) and the complexes FeL and CuL used in this work (Fig. 1) were synthesized and characterized as
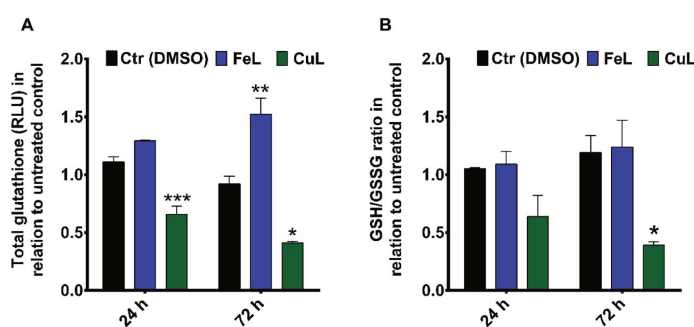

Fig. 5 FeL and CuL complexes alter glutathione metabolism or oxidative stress in H4 spheroids. Total glutathione (A) and GSH/GSSG ratio (B) in H4 spheroids after 24 h and 72 h of incubation with 25 µM of FeL and CuL. Results are shown as fold change normalized to the untreated control and represent the mean ± S.E.M of three independent replicas. Statistical significance was calculated using one-way ANOVA, followed by Dunnet's test (*$p \leq 0.05$, **$p \leq 0.01$, ***$p \leq 0.001$) in comparison to the DMSO control.

Paper

described previously.[23–25] Elemental analyses (CHN) and ESI-(+)-MS confirmed the identity and purity of the compounds.

A 1.0 mM stock solution of each complex was prepared by dissolving it in a 5% solution of dimethylsulfoxide (DMSO) prepared in ultrapure MiliQ water (H_2O). For biological experiments, solutions with the desired concentrations were prepared by diluting the compound's stock in the culture medium used. The stability of the compound's solutions was determined in Dulbecco's Phosphate-Buffered Saline (DPBS) (Gibco™, Thermo Fisher Scientific, Waltham, MA, USA) at physiological pH. For that, a solution of the compounds at a concentration of 25 μM was prepared and the UV-Vis spectrum of the solutions was obtained at different times (0, 24, 48 and 72 h) in a UV-Vis Spectrophotometer (Varian Cary 400).

Cell culture

Human brain neuroglioma (H4) cells (ATCC, Manassas, VA, USA) were grown in Dulbecco's Modified Eagle's Medium (DMEM) supplemented with 10% Fetal Bovine Serum (FBS) and 1% Penicillin/Streptomycin (all from Gibco™, Thermo Fisher Scientific). The cell line was cultured continuously as a monolayer at 37 °C and 5% of CO_2.

Viability assays

For IC_{50} determination, H4 cells were seeded at a density of 1.0 × 10^4 cells in 150 μL of medium in a 96-well black polystyrene microplate (Corning, NY, USA) and allowed to attach for 24 h at 37 °C. Then, the medium was removed and the wells were washed with DPBS before the addition of 150 μL of the 200, 100, 50, 25 and 12.5 μM solutions of the complexes, the respective vehicle controls (DMSO at the same concentration than in the complexes' solutions), or fresh medium (untreated control sample) to the wells. After 24 h of incubation, the medium in each well was removed, the wells washed with DPBS and 150 μL of a 10% solution of AlamarBlue (Thermo Fisher Scientific) in medium were added to each well. The plate was covered with aluminum foil and incubated for 2 h at 37 °C and subsequently read in a CLARIOstar® microplate reader (BMG LABTECH GmbH, Offenburg, Germany) for fluorescence detection.

For viability determination by flow cytometry, 7.0 × 10^5 cells were seeded in 75 cm^2 flasks (Greiner Bio-one, Frickenhausen, Germany) and incubated for 24 h at 37 °C. The medium was removed and cells were washed once with DPBS before 10.5 mL of fresh medium, medium with 25 μM of FeL and CuL, or medium with 0.125% of DMSO (as the vehicle control) were added to the flasks. The flasks were incubated for an additional 24 h, after which cells were detached and washed with DPBS. Then, for each sample, 1.0 × 10^6 cells were resuspended in DPBS and analyzed using a flow cytometer (BD FACS CANTO™ II) (unstained control samples). Then, those same cells were stained with 1 μg mL^−1 of propidium iodide (PI) (Sigma Aldrich, St. Louis, MO, USA) and re-analyzed. The percentage of live cells calculated for each sample was normalized to the untreated control sample, and three independent experiments were performed.

Fluorescence study by confocal microscopy

H4 cells were seeded at a density of 5.0 × 10^4 cells on a 22 mm coverslip placed in a 6-wells plate (CELLSTAR®, Greiner Bio-One), and allowed to attach overnight. Cells were then incubated or not (as a control) with 50 μM of FeL for 24 h at 37 °C. Then, cells were washed once with Hank's Buffered Salt Solution (HBSS; Thermo Fisher Scientific) and stained with 75 nM Lyso-Tracker™ Red DND-99 (Molecular Probes, Thermo fisher Scientific) for 30 min at 37 °C. The staining solution was removed and cells were fixed for 5 min in 4% of paraformaldehyde at room temperature. Samples were washed thrice, coverslips were mounted on HBSS onto a glass slide, and sealed with nail polish. Fluorescence was visualized on a confocal microscope (Zeiss LSM 710) using a standard DAPI filter for visualization of FeL fluorescence, while Lysotracker was visualized using a 561 nm laser for excitation followed by emission detection on the 566–691 nm range.

SOD/SOO-like activity

The reactivity on the superoxide anion was evaluated by a methodology described previously, which involves the reduction of nitroblue tetrazolium (NBT) by the superoxide anion.[33] Stock solutions of xanthine, nitroblue tetrazolium (NBT) and xanthine oxidase were prepared at the concentrations of 4.5 × 10^−4 mol dm^−3, 5.6 × 10^−5 mol dm^−3 and 0.2 U cm^−3, respectively, using a 0.05 mol dm^−3 phosphate buffer solution at pH 7.8 (all reagents from Sigma-Aldrich).

A control solution containing 1000 μL of the xanthine solution, 400 μL of the phosphate buffer solution and 1000 μL of NBT was added to a cuvette followed by the quick addition of 200 μL of the xanthine oxidase solution and then the absorbance was measured over time in a UV-Vis spectrophotometer (Varian Cary 50), thus obtaining the rate of change of the absorption in the absence of the complex.

To evaluate the activity of FeL and CuL, different concentrations of the complexes were employed: for FeL, the concentrations used were 1.92 × 10^−6, 3.85 × 10^−6, 7.69 × 10^−6, 1.15 × 10^−5, and 1.54 × 10^−5 mol dm^−3; for CuL, the concentrations used were 9.62 × 10^−8, 1.92 × 10^−7, 3.85 × 10^−7, 5.77 × 10^−7 and 7.67 × 10^−7 mol dm^−3. The concentration of the compounds which reduced 50% of NBT in relation to the control experiment was calculated, obtaining the IC_{50}, which was then transformed to K_{cat} using the equation proposed by McCord and Fridovich, $K_{cat} = K_{NBT} \times [NBT]/IC_{50}$, where $K_{NBT} = 5.94 \times 10^4$ M^−1 s^−1.[48,49]

CAT-like activity

The ability of the compounds in promoting H_2O_2 degradation was evaluated by the methodology described by Beers and Sizer.[50] Initially, the concentration of H_2O_2 was evaluated by titration with iodide/thiosulfate.[51] To determine the CAT-like activity of FeL, solutions of H_2O_2 at different concentrations (1.64 × 10^−2, 1.23 × 10^−3, 8.2 × 10^−3 and 4.1 × 10^−3 mol dm^−3) were prepared in a total volume of 2200 μL of a phosphate buffer solution at pH 7.8. Then, each solution was mixed with a FeL

solution yielding a final concentration of FeL of 7.69×10^{-5} mol dm^{-3}, and the decrease of the absorbance associated with the reaction with H$_2$O$_2$ was followed by UV-Vis spectroscopy at 240 nm (Varian Cary 50) in a 1 cm path length cell. For CuL, the above protocol was followed but the solutions were prepared on a piperazine solution (0.1 mol dm^{-3}) and the final CuL concentration in the mixture was 9.25×10^{-5} mol dm^{-3}. The experiments were performed in triplicate, and the Michaelis Menten constant (K_M) and the turnover number (K_{cat}) were then calculated for each complex.

Intracellular ROS measurements

For determination of intracellular ROS levels, H4 cells were prepared and incubated with the compounds (or respective medium and DMSO controls) as described above for the viability analysis by flow cytometry. Upon detaching and washing, 4.0×10^5 cells were incubated with 5 µM of CM-H$_2$DCFDA (Life Technology, Thermo fisher Scientific) in HBSS for 20 min at 37 °C in the dark. Stained cells were then washed once and resuspended in DPBS. Samples were analyzed in a flow cytometer (BD FACS CANTO™ II) and the average fluorescence intensity of each sample was normalized to the untreated control sample.

Cell cycle assay

For the cell cycle assay, cells were grown as described above for the viability determination by flow cytometry. After detaching and washing, 1.0×10^6 cells were fixed through drop by drop addition of 70% cold ethanol (v/v in DPBS) under gently vortexing. Samples were stored at 4 °C for 24 h, centrifuged and the supernatant was removed. Subsequently, 250 µL of RNase A (10 mg mL^{-1} in PBS; Sigma Aldrich) were added to each sample, which was then incubated at room temperature for 30 min and washed twice with DPBS. In the dark, each sample was stained with 20 µg mL^{-1} of propidium iodide (PI) (eBioscience, Thermo Fisher Scientific) for 15 min before being analyzed using a flow cytometer (BD FACS CANTO™ II). Three independent experiments were performed.

q-PCR

For RNA extraction, cells were prepared and incubated with the complexes (or respective medium and DMSO controls) as described above for the ROS determination and cell cycle analyses. Upon detaching and washing twice with DPBS, 1.0×10^6 cells were centrifuged, the supernatant was removed, and the pellet was stored at −20 °C until further use. Total RNA was extracted using the High Pure RNA isolation kit (Roche, Basel, Switzerland) according to the manufacturer's instructions. All the RNA samples were treated with DNase-1 to remove any contaminating genomic DNA, and the purity of the RNA was checked spectroscopically in a NanoDropND-1000 (NanoDrop Technologies). Then, 1 µg of purified RNA was reverse-transcribed using RT^2 First Strand Kit (Qiagen, Hilden, Germany) according to the manufacturer's instructions. Gene expression was assessed by real-time PCR using the cDNA obtained. For that, 25 ng of cDNA was amplified in 15 µL of

a reaction mix containing Power SYBR Green PCR Master mix (Thermo Fisher Scientific), 20 pmol of each primer pair (ESI Table 1†) and nuclease-free water. The thermal profile consisted of 1 cycle at 95 °C for 10 min followed by 40 cycles at 95 °C for 15 s, 60 °C for 1 min. The human GAPDH cDNA fragment was amplified as the internal control. Data analysis was performed using the $2^{-\Delta\Delta C_t}$ method.

Transwell migration assay

Cells starved overnight were detached and seeded onto cell culture inserts in 24-well plates (Millipore transwell PET filters, 8 µm pore; Merck, Kenilworth, NJ, USA) at a density of 1.0×10^4 cells in 150 µL of FBS-free medium, or FBS-free medium containing 0.125% DMSO, 25 µM of FeL or 25 µM of CuL. The lower transwell chambers were filled with 600 µL of media without FBS (negative control) or with medium containing 10% FBS. After 24 h of incubation at 37 °C, the inserts were washed with DPBS, fixed with 4% paraformaldehyde, washed again, and stained with 1 µg mL^{-1} of Hoechst 33 342 (Thermo Fisher Scientific) for 20 min at room temperature. Cells were then imaged using a 20× objective on a confocal microscope (Zeiss LSM 710). Seven random fields were photographed per insert, with at least two inserts being analyzed for each condition per experiment. The results shown were calculated based on three independent experiments.

Spheroid viability assay

For spheroids formation, 2.5×10^3 cells were seeded in 100 µL per well in 96-well plates coated with 1.5% agarose (w/v in PBS). After 1 day of incubation, spheroids were fully formed, and 100 µL of fresh medium or medium with DMSO or the complexes was added to a final concentration of 0.125% and 25 µM, respectively. Cells were incubated for 24 h or 72 h at 37 °C before cell viability was estimated using the CellTiter-Glo® 3D assay (Promega, Madison, WI, USA) according to the manufacturer's instructions. Luminescence was read in a CLARIOstar® microplate reader and the average luminescence of 8 spheroids per condition was normalized to the average luminescence of the untreated control sample, for at least two independent experiments.

In addition, spheroid viability was also estimated based on spheroid growth. For that, the total area of each spheroid was determined using the INSIDIA macro in FIJI,[52] and then normalized to the area of the spheroid at day 0 (to account for possible differences in the spheroids' initial size) and to the size of the untreated spheroids at each time point (to assess the effect of the DMSO and the compounds on spheroids' growth). Several spheroids (at least 7) were analyzed per condition and time point, for at least two independent experiments.

Spheroid invasion assay

Each one-day old spheroid, formed as described above, was collected into a tube, washed once with FBS-free medium, and resuspended in 40 µL of a 4.5 mg mL^{-1} Matrigel (Cat. Number 356231; Corning) solution in FBS-free medium. Then, each spheroid-containing suspension was spotted onto the centre of

a well of a 24-well plate and incubated as a hanging drop for 1 h until the matrigel had polymerized. Complete medium, complete medium with 0.125% DMSO, or complete medium containing 25 μM of the complexes were added and the spheroids were incubated for 24 h at 37 °C before being irradiated (or not as a control) with 6 Gy X-rays on a Faxitron MultiRad225 and further incubated at 37 °C. Images of spheroids and invading cells were acquired immediately after embedment and every 24 h after that, using an Eclipse Ts2 microscope (Nikon). At each time point (24 h, 48 h, and 72 h) the total area of the spheroid and invading cells was determined as described above.

Spheroid GSH/GSSG assay

Spheroids were formed and incubated with the compounds or respective controls as described above for the viability assessment. Then, the spheroids were carefully transferred to a white 96-wells polystyrene plate (Greiner Bio-One) and the media was aspirated. Total glutathione and the ratio of GSH/GSSG were then estimated using the GSH/GSSG-Glo™ Assay (Promega) according to the manufacturer's instructions with one minor change: after addition of the lysis buffer, the plate was shaken for 30 min to allow for proper lysis of the spheroids. Luminescence was then read in a CLARIOstar® microplate reader. Three spheroids were analyzed per day and condition, and the average luminescence of those spheroids was normalized to the average luminescence of the untreated control sample. Three independent experiments were performed.

Statistics

All data are shown as mean values ± standard error of the mean (S.E.M.) of the DMSO-treated or complex treated samples relative to the untreated control. Statistical and data analysis was carried out using GraphPad Prism 6 software. Statistical differences between treatment and control samples were assessed by one-way ANOVA or two-way ANOVA followed by Dunnett's test. The threshold for statistical significance was set to $P = 0.05$.

Conflicts of interest

There are no conflicts to declare.

Acknowledgements

References

1 C. Alifieris and D. T. Trafalis, *Pharmacol. Ther.*, 2015, **152**, 63–82.

2 Q. Sun, R. Xu, H. B. Xu, G. M. Wang, X. M. Shen and H. Jiang, *World J. Surg. Oncol.*, 2017, **15**, 181.

3 J. Rosen, T. Blau, S. J. Grau, M. T. Barbe, G. R. Fink and N. Galldiks, *Case Rep. Oncol.*, 2018, **11**, 591–600.

4 D. L. Ma, C. Wu, S. S. Cheng, F. W. Lee, Q. B. Han and C. H. Leung, *Int. J. Mol. Sci.*, 2019, **20**, 341.

5 U. Ndagi, N. Mhlongo and M. E. Soliman, *Drug Des., Dev. Ther.*, 2017, **11**, 599–616.

6 N. Muhammad and Z. Guo, *Curr. Opin. Chem. Biol.*, 2014, **19**, 144–153.

7 A. Bergamo and G. Sava, *Chem. Soc. Rev.*, 2015, **44**, 8818–8835.

8 B. Tang, D. Wan, S. H. Lai, H. H. Yang, C. Zhang, X. Z. Wang, C. C. Zeng and Y. J. Liu, *J. Inorg. Biochem.*, 2017, **173**, 93–104.

9 Y. H. He, H. Y. Xue, W. D. Zhang, L. Wang, G. Y. Xiang, L. Li and X. M. Shang, *J. Organomet. Chem.*, 2017, **842**, 82–92.

10 M. C. Ruiz, J. Kljun, I. Turel, A. L. Di Virgilio and I. E. Leon, *Metallomics*, 2019, **11**, 666–675.

11 S. S. Gu, P. Yu, J. N. Hu, Y. N. Liu, Z. W. Li, Y. Qian, Y. Wang, Y. Gou and F. Yang, *Eur. J. Med. Chem.*, 2019, **164**, 654–664.

12 B. Tang, D. Wan, Y. J. Wang, Q. Y. Yi, B. H. Guo and Y. J. Liu, *Eur. J. Med. Chem.*, 2018, **145**, 302–314.

13 J. P. C. Coverdale, T. Laroiya-McCarron and I. Romero-Canelon, *Inorganics*, 2019, **7**, 31.

14 E. D. Williams, D. Gao, A. Redfern and E. W. Thompson, *Nat. Rev. Cancer*, 2019, **19**, 716–732.

15 L. Avila-Carrasco, P. Majano, J. A. Sanchez-Tomero, R. Selgas, M. Lopez-Cabrera, A. Aguilera and G. G. Mateo, *Front. Pharmacol.*, 2019, 10.

16 A. Sánchez-Mora, H. Valdés, M. T. Ramírez-Apan, A. Nieto-Camacho, S. Hernández-Ortega, D. Canseco-González and D. Morales-Morales, *Inorg. Chim. Acta*, 2019, **496**, 119061.

17 W. S. Wu, *Cancer Metastasis Rev.*, 2006, **25**, 695–705.

18 C. H. Wu, S. C. Tang, P. H. Wang, H. Lee and J. L. Ko, *J. Biol. Chem.*, 2012, **287**, 25292–25302.

19 W. Lv, L. L. Sui, X. N. Yan, H. Y. Xie, L. P. Jiang, C. Y. Geng, Q. J. Li, X. F. Yao, Y. Kong and J. Cao, *Chem.-Biol. Interact.*, 2018, **279**, 136–144.

20 C. Ninsontia, P. P. Phiboonchaiyanan and P. Chanvorachote, *Cancer Cell Int.*, 2016, **16**, 48.

21 S. H. Jeong, Y. J. Jeon and S. J. Park, *Mol. Med. Rep.*, 2016, **14**, 5148–5154.

22 J. W. Jiang, K. Wang, Y. Chen, H. N. Chen, E. C. Nice and C. H. Huang, *Signal Transduction Targeted Ther.*, 2017, **2**, 17036.

23 A. Horn, I. Vencato, A. J. Bortoluzzi, R. Horner, R. A. N. Silva, B. Spoganicz, V. Drago, H. Terenzi, M. C. B. de Oliveira, R. Werner, W. Haase and A. Neves, *Inorg. Chim. Acta*, 2005, **358**, 339–351.

24 A. Horn, I. Vencato, A. J. Bortoluzzi, V. Drago, M. A. Novak and A. Neves, *J. Braz. Chem. Soc.*, 2006, **17**, 1584–1593.

25 C. Fernandes, A. Horn, O. Vieira-da-Motta, V. M. de Assis, M. R. Rocha, L. D. Mathias, E. S. Bull, A. J. Bortoluzzi, E. V. Guimaraes, J. C. A. Almeida and D. H. Russell, *J. Inorg. Biochem.*, 2010, **104**, 1214–1223.

26 A. Horn, A. Neves, I. Vencato, V. Drago, C. Zucco, R. Werner and W. Haase, *J. Braz. Chem. Soc.*, 2000, **11**, 7–10.

27 A. Horn, L. Firn, A. J. Bortoluzzi, B. Szpoganicz, M. D. Silva, M. A. Novak, M. B. Neto, L. S. Eberlin, R. R. Catharino, M. N. Eberlin and C. Fernandes, *J. Mol. Struct.*, 2006, **797**, 154–164.

28 J. Fan, Y. W. Ou, C. Y. Wu, C. J. Yu, Y. M. Song and Q. M. Zhan, *Acta Pharmacol. Sin.*, 2012, **33**, 1301–1310.

29 T. D. Ribeiro, F. L. Fonseca, M. D. C. de Carvalho, R. M. D. Godinho, F. P. de Almeida, T. D. Saint'Pierre, N. A. Rey, C. Fernandes, A. Horn and M. D. Pereira, *Biochem. J.*, 2017, **474**, 301–315.

30 K. A. Mapuskar, C. M. Anderson, D. R. Spitz, I. Batinic-Haberle, B. G. Allen and R. E. Oberley-Deegan, *Semin. Radiat. Oncol.*, 2019, **29**, 72–80.

31 F. De Lazzari, L. Bubacco, A. J. Whitworth and M. Bisaglia, *Aging Dis.*, 2018, **9**, 716–728.

32 I. Batinic-Haberle, A. Tovmasyan and I. Spasojevic, *Redox Biol.*, 2015, **6**, 656.

33 T. P. Ribeiro, C. Fernandes, K. V. Melo, S. S. Ferreira, J. A. Lessa, R. W. A. Franco, G. Schenk, M. D. Pereira and A. Horn, *Free Radicals Biol. Med.*, 2015, **80**, 67–76.

34 R. O. Costa, S. S. Ferreira, C. A. Pereira, J. R. Harmer, C. J. Noble, G. Schenk, R. W. A. Franco, J. A. L. C. Resende, P. Comba, A. E. Roberts, C. Fernandes and A. Horn, *Front. Chem.*, 2018, **6**, 491.

35 A. Horn, G. L. Parrilha, K. V. Melo, C. Fernandes, M. Horner, L. D. Visentin, J. A. S. Santos, M. S. Santos, E. C. A. Eleutherio and M. D. Pereira, *Inorg. Chem.*, 2010, **49**, 1274–1276.

36 U. Weser and L. M. Schubotz, *J. Mol. Catal.*, 1981, **13**, 249–261.

37 J. Switala and P. C. Loewen, *Arch. Biochem. Biophys.*, 2002, **401**, 145–154.

38 B. Kalyanaraman, V. Darley-Usmar, K. J. A. Davies, P. A. Dennery, H. J. Forman, M. B. Grisham, G. E. Mann, K. Moore, L. J. Roberts and H. Ischiropoulos, *Free Radicals Biol. Med.*, 2012, **52**, 1–6.

39 S. Tuncer, R. Gurbanov, I. Sheraj, E. Solel, O. Esenturk and S. Banerjee, *Sci. Rep.*, 2018, **8**, 14828.

40 J. Lu and A. Holmgren, *Free Radicals Biol. Med.*, 2014, **66**, 75–87.

41 Z. Liao, D. Chua and N. S. Tan, *Mol. Cancer*, 2019, **18**, 65.

42 E. H. Verbon, J. A. Post and J. Boonstra, *Gene*, 2012, **511**, 1–6.

43 G. K. Schwartz and M. A. Shah, *J. Clin. Oncol.*, 2005, **23**, 9408–9421.

44 T. Ishiguro, H. Ohata, A. Sato, K. Yamawaki, T. Enomoto and K. Okamoto, *Cancer Sci.*, 2017, **108**, 283–289.

45 S. Nath and G. R. Devi, *Pharmacol. Ther.*, 2016, **163**, 94–108.

46 M. Wank, D. Schilling, T. E. Schmid, B. Meyer, J. Gempt, M. Barz, J. Schlegel, F. Liesche, K. A. Kessel, B. Wiestler, S. Bette, C. Zimmer and S. E. Combs, *Cancers*, 2018, **10**, 456.

47 A. Bansal and M. C. Simon, *J. Cell Biol.*, 2018, **217**, 2291–2298.

48 M. Grau, F. Rigodanza, A. J. P. White, A. Soraru, M. Carraro, M. Bonchio and G. J. P. Britovsek, *Chem. Commun.*, 2014, **50**, 4607–4609.

49 G. N. Ledesma, H. Eury, E. Anxolabehere-Mallart, C. Hureau and S. R. Signorella, *J. Inorg. Biochem.*, 2015, **146**, 69–76.

50 R. F. Beers and I. W. Sizer, *J. Biol. Chem.*, 1952, **195**, 133–140.

51 J. P. N. Ribeiro, M. A. Segundo, S. Reis and J. L. F. C. Lima, *Talanta*, 2009, **79**, 1169–1176.

52 C. Moriconi, V. Palmieri, R. Di Santo, G. Tornillo, M. Papi, G. Pilkington, M. De Spirito and M. Gumbleton, *Biotechnol. J.*, 2017, **12**, DOI: 10.1002/biot.201700140.

Discussion and Conclusion

In this thesis, the role of oxygen in radiotherapy was investigated at three different levels: (i) on a (radio-)chemical level in water measurements, (ii) on a genetic level in cancer cell lines and (iii) on a mechanistic level in cancer cells and spheroids. Additionally, radiolytic processes as investigated in (i) for FLASH-dose rates were further investigated on UHDRs and feasibility studies were conducted for joined oxygen-biological tissue-studies. In this chapter, the findings of the studies are discussed and put in the overall context.

Radiochemical oxygen effects

In Publication I, the dependence of oxygen abundance on imparted dose as a function of dose rate was measured in a water phantom. This study was performed to test the oxygen depletion hypothesis, a common hypothesis to explain the FLASH effect (see Section 3.1). For this experiment, a 3D-printed plastic phantom was filled with air-nitrogen-enriched water in order to modify the oxygen content of the water-filling and the phantom was sealed airtight. Inside the phantom, an oxygen sensor was placed which could be read-out optically via a 633 nm LED. The optical read-out technique allowed for non-invasive measurements, which is of critical importance, as any other read-out method, which involves opening the phantom, would affect the oxygen content itself. The phantom was then irradiated with photons, protons and carbon ions at different dose rates and the oxygen content in the water was measured as a function of time and dose. It was observed, that oxygen decreased almost linearly with dose, which contradicts theories claiming an exponential decrease[71]

and instead fits theories proposing an inverse Michaelis-Menten Kinetics (see Section 3.1.3). Interestingly, the results presented in Publication I showed less oxygen depletion for higher dose rates. The same trend of higher dose rates causing less O_2 depletion has been confirmed by other research labs this year on both experimental and modeling approaches.[74,86,87] Theoretical approaches so far either postulated a constant dose-independent depletion, which stems from calculations of radiolytic reactions and could explain FLASH effects due to radiation induced hypoxia[67], or postulated a larger total depletion.[71] Consequently, the findings shown in this thesis rejected the oxygen depletion hypothesis as a sole cause for the FLASH effect. Instead, more importance needs to be given to radio-chemical studies: Measurements of oxygen during and after irradiation allow for insights on the "end state" of reactions between radicals or reactions involving O_2, as they contribute to the depletion of oxygen itself (see Table 3.1). A smaller oxygen depletion measured at large dose rates means that either fewer radicals were produced initially to react with oxygen, or that the same amount of radicals was produced but radical-radical recombinations took place before reactions with oxygen could happen. In the latter case, the amount of radicals present would decrease shortly after irradiation (i.e. on a timescale of 10^{-12}-10^{-6} s[48]). This would imply, that there might be fewer radicals to react with DNA or cell organelles, leading to less overall cellular damage at higher dose rates. This hypothesis is in good agreement with several studies showing that FLASH dose rates cause less damage on cellular level compared to conventional dose rates due to altered ROS levels.[69]

Genetic oxygen effects

The effects of radiation on cells cannot be explained by reactions between radicals and DNA or cell compartments alone: Intracellular processes such as DNA repair mechanisms or apoptosis systems play a crucial role in cell survival and can be altered by hypoxia. Since both hypoxia and radiation can heavily impact the abundance of ROS[88] and the cell's oxidative stress regulation mechanisms, both effects are closely intertwined. Hence, the next aim was to investigate the effect of both hypoxia and radiation on a genetic level in four human cancer cell lines and to establish an analysis method to separate the two effects from each other. For this purpose, cells from Non-small-cell lung cancer (H460), brain neuroglioma (H4), urinary bladder carcinoma (T24) and prostate adenocarcinoma (PC3) were first incubated in hypoxia at 0.3 % O_2 and then irradiated with photons at 6 Gy in a LINAC. Another set of sample was irradiated at 6 Gy in normoxia. Also, unirradiated controls for both oxygen conditions were prepared. Three days after treatment, cell pellets were harvested and a genome analysis was performed on the cells. As a result, some modifications in cellular genetic profiles were visible depending on their respective

treatment, especially in DNA-repair genes. When comparing the gene expression sets of all four cell lines, however, the changes in gene expression were strongly influenced by the cell line itself and only slightly by the treatment. This was observed by performing a PCA on the data set, which revealed clustering based on cell line features and no clustering based on treatment, implying that cell line features outweighed treatment effects on a genetic level. By normalizing the gene expression levels of irradiated cells to non-irradiated cells for both hypoxic and normoxic settings, the developed "oxygen-impact" analysis pathway allowed for an elimination of unwanted cell line features in the gene expression data. Additionally, the "radiation-in-hypoxia" pathways was set up, which normalizes gene expression of irradiated, hypoxic cells onto gene expression values of the non-irradiated, hypoxic samples. After applying the self-developed analysis pathways, gene data clustered together in the PCA based on their pathway transformation, whereas the cell line dependence vanished. Hence, the analysis pathways turned out to be a robust tool for investigating genetic regulations in cancer cells after irradiation in normoxia and hypoxia while suppressing cell line specific features, which allowed for a broad genomic analysis. In a next step, a hierarchical cluster analysis was performed on the data modulated by the "radiation-in-hypoxia" and "radiation-in-normoxia" analysis pathways which normalize the cell's gene expression values after irradiation onto the non-irradiated counterpart. Applying the analysis pathways onto the gene expression sets together with a hierarchical cluster analysis allowed for (i) a successful reduction of cell line specific features while maintaining oxygen-dependent effects in radiation treatment and (ii) reorganization of patterns in the gene sets.

The hierarchical cluster analysis in combination with the two radiation analysis pathways resulted in a three-level-clustering of the genetic data. For the further interpretation, only genes were taken into account, which showed a similar expression behavior over the four cell lines in order to increase robustness of the analysis. The three clustering levels were: 1. genes that showed up-regulation after irradiation, independent on the oxygen content present during irradiation; 2. genes that showed down-regulation after irradiation, and 3. genes whose up- or down-regulation was dependent on the oxygen content. For the understanding of the interplay of oxygen and radiation, group 3 is of major importance as a change in oxygen level can alter genetic expression levels drastically. In the present study, this affected mainly the genes CD274, IL13, NOX1, and TNF. CD274 is a gene encoding for PD-L1, an immune inhibitory receptor ligand. PD-L1 is over-expressed by some tumors which helps the tumor cells to evade the immune system[89]. IL13 is involved in immune system processes as a messenger and mediates the production of antibodies by B-Lymphocytes[90,91]. NOX1 is the gene encoding for the enzyme NADPH-oxidase 1, which is involved in generating superoxide or H_2O_2 via the catalytic one-electron transfer of oxygen, leading to an increased production of endogenous ROS[92]. The

proinflammatory cytokine Tumor Necrosis Factor (TNF) is, among other functions, involved in cell proliferation, apoptosis and lipid metabolism[93,94]. In the present study, CD274 / PD-L1 and NOX1 were up-regulated after irradiation in hypoxia and down-regulated in normoxia, whereas IL13 and TNF showed opposite regulation pattern. These mentioned genes were the only ones showing a clear oxygen dependence leading to an inverse effect in gene expression following radiation. This finding is of high importance as the genes affected are involved in oxidative stress mechanisms, immune-response, inflammation and apoptosis implying that these cellular mechanisms are potentially differently triggert in radiation depending on the cells' O_2 state.

In addition, it was also observed that CCNB3, the gene encoding for cyclinB, was less expressed after irradiation for both oxygen condition. Together with a cell cycle study performed in the course of this experiment, these results agree well since a down-regulation of cyclinB leads to a delayed start of mitosis and hence more cells are arresting in G2 phase, which was observed to be the case in the cell cycle analysis.

Another observation of this study was a higher expression of the gene SOD2, encoding for MnSOD (see Section 2.3.1), after irradiation with this effect being even more pronounced after irradiation in normoxia.

From this study, it could be concluded from a methodological point of view, that the usually intertwined effects of oxygen and radiation on the genetic expression levels in cancer cells could be detangled and analyzed using newly designed analysis pathways and applying them onto the gene sets in combination with a PCA and hierarchical cluster analysis. From a gene content perspective, it could be observed that in all oxygen conditions, DNA repair pathway modulating genes were down regulated after irradiation. Since SOD2 and HIF1 were simultaneously up-regulated, a conclusion can be made that cells deal with higher ROS concentrations after radiation, leading to up-regulation of ROS-scavenging systems such as SOD. The findings from this study strengthen the importance of the interplay of radiation, hypoxia and genetic response with respect to application in immune-therapy and radio-immune-therapy[95] as well as therapeutic concepts focusing on SOD modulation[96,97].

Mechanistic oxygen effects

As it became clear that oxygen can act as a switch in radiation treatment in a way that the presence or absence cannot only amplify radiation effects but can even have an inverse effect on genetic response, oxygen effects were also studied on radical scavenging systems in human neuroglioma cells (H4) (see Publication III). Using CuL and FeL compounds mimicking SOD and CAT, the cellular radical scavenging

systems were intended to be influenced. CuL and FeL concentrations were chosen in a way to impact cellular's SOD activity while simultaneously not influencing cells' viability. It was found that both CuL and FeL showed antioxidant activity outside of cells, and for FeL, also in H4 cells. Cell spheroids treated with the compounds were irradiated with 6 Gy photon irradiation under normoxic conditions and their invasiveness was observed after irradiation using an invasion assay in matrigel. It is well known, that photon irradiation can cause an EMT transition, implying a greater metastatic potential[98]. After treatment with the compounds, a decreased invasive behavior was observed, strengthening the importance of ROS scavenging systems for both cellular survival and metastatic behavior. The exact mechanism responsible for the reduced invasiveness was not completely elucidated, however, oxidative stress or gluthadione metabolism seemed to be involved.

Oxygen effects in FLASH radiotherapy

As a summary, oxygen effects were examined on radio-chemical, genetic, and mechanistic levels in the course of this thesis in (conventional) photon, proton and carbon ion radiotherapy. However, regarding the role of oxygen in FLASH radiotherapy, there are currently three main open questions:

1. Does the FLASH effect of protecting tissue only occur in a specific O_2 regime?

2. Does the beam pulse structure matter in FLASH effects, and if yes, how?

3. What is the underlying mechanism causing the FLASH effect?

At first glance, question 1 seems clear, since many *in vivo* studies and simulation studies showed that the FLASH effect is prominent in a low O_2 regime. However, new findings obtained in this thesis showed a prominent FLASH effect also at higher O_2 levels in clonogenic survival experiments in cell culture (see Appendix B.2): Using the O_2 sensor technique presented in Publication I, it was possible to perform combined O_2-and-cell-measurements allowing for a specific O_2 control of irradiated cell samples under FLASH conditions. In this cell survival study, it was found that the FLASH effect increased with O_2 level. This was especially surprising since even at 21 % O_2, a FLASH effect was visible (see Figure B.2) with a DMF of around 2 at a survival of 0.001 in normoxic conditions, being slightly higher than DMF values previously reported of around 1.4 - 1.8.[99] Here it is important to mention, that existing data mostly focuses on *in vivo* measurements and not necessarily on *in vitro* measurements. Excitingly, a new publication from Adrian et al. (2021)[83] observed as well a FLASH effect *in vitro* at normoxic conditions, reporting DMF values around 1.3 at a survival fraction of 0.1. It is not understood yet why FLASH

effects seem to occur also in normoxic conditions *in vitro*, but further experiments including close oxygen monitoring using the optical O_2 sensors could provide further insights. In addition, in Appendix B.1, combined irradiation experiments of O_2 levels and wildtype-zebrafish-embryos were performed and radiation-induced damage was studied during a four day follow-up. The analysis of the biological response is still ongoing, but it can be already stated that it was feasible to measure O_2 depletion directly at irradiation site of zebrafish-embryos allowing for close O_2 monitoring. From studies with zebrafish embryos, it is known that they act in principle as a suitable model organism between classical *in vitro* cell culture and animal studies. Recent studies have succeeded to show a FLASH effect also in zebrafish embryos[65] which gives a great basis to perform further investigations into mechanistic studies in cell culture and zebrafish embryos and, with the result from Appendix B.1, also in combination with O_2 measurements.

In the presented study in Appendix B.1, the irradiation was carried out with the electron accelerator ELBE, on which various combinations of pulse durations and dose rates could be tested, which leads to the answer to question 2: **Does the pulse structure matter, and if yes, how?**
The effect of the beam's macro- and micropulse structure on FLASH effects has not been conclusively clarified yet[100]. However, more and more publications started to state these beam settings explicitly[10,101]. In this thesis, work presented in Appendix A.1 and B.1 focused on the impact of pulse structure on both oxygen depletion and tissue response. Hereby, oxygen depletion measurements were similarly conducted to the setup used in Publication I, but broader O_2 ranges were chosen, which allowed for an improved quantification of the depletion effects. Four different beam pulse structures for electrons were tested, as well as irradiation at UHDR from laser-accelerated protons obtained at the DRACO laser. Photon measurements served as base line and cross reference. A fixed dose was applied onto the water phantom and steady-state O_2 levels were analyzed, i.e. O_2 levels before radiation and about 20 s after. This method represents a changed read-out method compared to Publication I, in which gradients of O_2 and dose were determined. While the gradient-method was suitable for low and intermediate dose rates, it was not suitable for the UHDRs used in the study presented in Appendix A.1, due to the detector's readout-speed being slow compared to the dose rates used. The analysis of steady-states allowed for a robust measurement technique independent from dose rate. The depletion data plotted against initial oxygen values (similar to typical *G*-value depictions) revealed a strong LET dependence of oxygen depletion, and more depletion was found for higher dose rates as also seen in Publication I. Furthermore, it became clear from the results, that the pulse structure had an impact on depletion, revealing that the average dose rate seamed to be more dominant for depletion processes than the pulse

dose rate. While the LET dependence of G-values is well known[48], the dose-rate dependence is entirely new and has not been reported so far. FLASH-effect simulations typically assume a constant G-value which translates into dose-dependent radical production by multiplying with the dose rate. The results in this thesis, however, showed a strong dose rate G-value dependence. In addition, this dependence was not linear, but was proportional to $1/\sqrt{D}$.

The findings imply, that simulation studies should implement dose-rate and beam pulse structure-dependent G-values in order to cover more radiolytic processes. In addition, potentially special pulse sequences could be developed in order to optimize the FLASH effect and hence a clinical outcome in patient treatment.

From the findings in this thesis, it can be conducted that the oxygen depletion measurements in water correlate clearly with the cellular effects (Publication I and Appendix B.2), leading to the question of **what is the underlying mechanism causing the FLASH effect?** I.e. whether FLASH is simply a radiochemical phenomenon, or if it is a combination of multiple aspects such as radiochemistry but also immunoresponse or differences in radical scavenging systems. If one considers the FLASH effect as a result of the treatment of the same tissue with two different beams at different dose rates, then the radiochemistry contribution is most likely the dominant part, since all cellular response mechanisms remain the same. If, in contrast, one considers the FLASH effect as a result of a treatment of different tissue (i.e. tumorous and healthy) with the same high-dose-rate-beam and compares this setting to conventional dose rate treatment, many tissue-related mechanisms need to be taken into account. In this thesis the focus was placed on the former by examining the effect of different dose rates on the same target object.

The observation that FLASH depleted less O_2 compared to conventionally applied dose rates suggests that although oxygen levels are changed during radiation, this change is most likely not sufficient to have significant effect on cellular metabolism caused by radiation-induced hypoxia. However, the findings suggest that due to less O_2 depletion being observed in FLASH radiation, potentially less radicals could interact with O_2 present in the water under FLASH conditions. This may be due a to a higher production rate of radicals directly after irradiation compared to conventional radiotherapy. Although the total number of radicals being produced would be constant, a higher initial rate would lead to an increased reaction of radicals with each other before they can react with O_2. Transferred to cellular levels, this would imply, an initially increased production rate of radicals but a decreased production of macro-radicals such as H_2O_2 originating from radiolysis would occur that could harm the DNA. This also applies to lipid peroxidations as a cause for DNA damage, since the relevant $ROO^{\bullet}$ molecules could undergo self-reactions lead-

ing to chain termination[77]. It seems logical that ROS levels are most likely lowered in FLASH radiation compared to conventional radiation, like it was already confirmed by Montay-Gruel et al. (2019) in mice[69]. In addition, decreased ROS levels would imply a decreased EMT induction and hence potentially less metastatic potential[102,103,104]. Combining these two phenomenons, it seems likely that FLASH radiotherapy could decrease metastasis formation. This, however, is yet to be investigated.

The assumption of decreased metastasis potential fits to the observation that high-LET radiation causes less O_2 depletion and also less radiation-induced metastasis[105], potentially also due to decreased ROS levels. However, further research needs to be conducted on the question whether ROS and radical-scavenging systems like SOD, CAT and GPX play a critical role in FLASH. This could potentially be reached applying the FeL and CuL compounds presented in Publication III or other radiosensitizers in FLASH studies and to investigate the impact on the oxygen-sensing genes IL13, PD-L1, TNF and NOX1 investigated in Publication II. In fact, first ideas have been formulated to test FLASH together with anti-PD-L1 drugs[106,107] in order to gain deeper knowledge about the FLASH effects and potential links to immune-response and to ultimately broaden the way into clinical application.

CHAPTER 6 ▪

Summary

In the course of this thesis, oxygen effects in conventional radiotherapy were investigated on a radio-chemical level, a genetic level and a mechanistic level in human cancer cell lines. Moreover, the impact of FLASH dose rates (i.e. dose rates above 40 Gy/s) on oxygen depletion in water and on cell survival was tested. In addition, the impact of the beam pulse structure on oxygen depletion was investigated.

Oxygen plays an important role in many cellular mechanisms and acts as a radiosensitizer in radiotherapy. However, it is not entirely clear which radiation effect stems from the radiation itself and which aspect results from oxygen or a lack thereof - since both hypoxia and radiation can alter the ROS levels and gene levels of cells. Hence, this thesis investigated the impact of oxygen abundance on both radio-chemical and cellular level. For FLASH radiotherapy as a special case with a growing influence in radiation therapy, the effect of oxygen is only poorly understood. It was observed that FLASH dose rates have the potential to spare healthy tissue while maintaining tumor control. However, oxygen effects in FLASH are critical, since too high or too low oxygen levels in the target volume seem to turn off any effect. A popular explanation is given by the oxygen depletion hypothesis but this has not yet been confirmed. The purpose of the thesis was therefore to study oxygen effects in radiotherapy in general, with a focus on FLASH dose rates in order to examine the oxygen depletion hypothesis.

For that purpose, oxygen measurements in water using an TROXSP5 optical sensor were conducted for photon, electron, proton and carbon ion beams. Furthermore, gene expression studies using a self-developed analysis method including PCA and hierarchical clustering were performed. ROS scavenging systems were modulated in cells and spheroids using CuL and FeL compounds and the effect on metastasis formation was tested in migration assays. In addition, cell survival studies with

varying oxygen levels were conducted using FLASH dose rates. Furthermore, beam pulse structures were varied in electron beams in order to test the impact on oxygen depletion. This was combined with feasibility studies of hybrid-O_2-and-bio-samples like cells and zebrafish embryos.

From a radio-chemical perspective, it was found that oxygen levels in water are affected by radiation, with depletion measurable after and during irradiation. However, depletion was rather small, being less than 0.5 % decrease in oxygen after 10 Gy radiation, which was in accordance with literature. Higher-LET radiation caused less depletion. Surprisingly, oxygen depletion was smaller for higher dose rates, which contradicts the oxygen depletion hypothesis. Therefore, oxygen depletion cannot be further considered as the main factor in explaining FLASH effects. On a genetic level, it was found that gene expression levels were groupable into patterns when comparing expression after radiation with photons at conventional dose rate and at different oxygen levels. Hereby, the developed analysis algorithm was able to detangle oxygen effects from radiation effects and to suppress cell line specific features. The genes TNF, PD-L1, NOX1 and IL13 appeared to have a inverse expression pattern after radiation, depending on the O_2-level before. Since these genes are involved in oxidative stress mechanisms, immune-response, apoptosis and inflammation, the finding underlines the importance of knowledge about the oxygen state of a cell culture or, transferred to a clinical purpose, of a tumor tissue. In a third step, changes of ROS levels via CuL and FeL compounds could be linked to decreased metastatic behavior of glioma cell spheroids after conventional irradiation.

In summary, oxygen is of great relevance in various areas of radiation therapy. In particular, it should be emphasized that it is still unclear whether oxygen-dependent FLASH effects are the same *in vivo* and *in vitro*. The experiments in this thesis have shown that the FLASH effect also occurred at high oxygen levels *in-vitro*, which does not seem to be the case *in vivo*. The reasons for this may be various; it could be worthwhile to further involve the immune system in research of FLASH effects. The immune-response gene PD-L1 being a switching gene depending on oxygen in irradiation supports that suggestion. FLASH dose rates actually depleting less oxygen compared to conventional dose rates also raises the question whether fewer radicals and therefore fewer ROS are generated. Together with the results that ROS modulation by CuL / FeL compounds reduces the metastatic potential, this leads to the open question of whether FLASH dose rates also have an effect on the formation of metastases by reducing metastatic potential. Furthermore, beam pulse dose rate was found to play a role in oxygen depletion and hence in radical production. Further research could address the optimization of beam pulse dose rates in order to achieve maximal tumor response at minimal normal tissue complication in patient treatment. The interplay of oxygen and radiation investigated in this

thesis strengthens the relevance of radiolytic chemical yields in radiotherapy and their impact on water and cellular material, laying the foundation for future patient treatment optimization.

A.1 The dose-rate dependence of G-values: Impact of beam structure parameters and ultra high dose rates (FLASH) on oxygen depletion in water

Introduction

In the past years, FLASH radiotherapy i.e. the irradiation with high and ultra-high dose rates has gained increased importance due to its sparring of healthy tissue whilst maintaining tumor control. High dose rates are typically defined as dose rates above 40 Gy/s. Already in the '60s and '70s, it was found in in-vitro studies with bacteria, that irradiation with high dose rates show in increased radio-resistance, compared to conventional dose rates. As radiation techniques improved, this treatment modality became interesting again in the 2010s, when FLASH was applied to animals: In studies by Favaudon et al[63], it was found, that after irradiation with FLASH, cancer cells showed comparable response to conventional dose rates, whereas healthy tissue showed a protective effect. This study was confirmed by others, like Vozenin et al. in cat cancer patients[64]. From these studies, it could be concluded that FLASH irradiation leads to two effects: On the one hand, *in-vivo*, a differential effect was observed, i.e. radio-protection of healthy tissue with comparable tumor control probability compared to conventional radio therapy. This effect was even observed in a first-in-man-study[66]. On the other hand, in-vitro, i.e. in cell culture experiments, FLASH irradiation causes an increase in radio-resistance within

the same (cancer-) cell line. It is known, that this effect depends on the oxygen concentration of the tissue[68,108]. These findings were interpreted as a hint towards an oxygen depletion hypothesis: A high dose rate could cause an increased depletion of oxygen, leading to decreased oxygen levels present in the tissue. Hence, irradiation could cause a radiation-induced hypoxia leading to an increased radio-resistance via the Oxygen Enhancement Ratio (OER). This hypothesis was controversially discussed in the past years, including many theoretical and experimental studies[109]. However, recent studies showed on an experimental and simulation approach, that oxygen depletion cannot be the sole cause for the FLASH effect[74,86,87,110]. Although it is very clear, that the FLASH effect strongly depends on oxygen, the underlying mechanism remains unknown. Different studies propose a dependence of cell survival not only on dose rate but also on pulse structure of the beams used for irradiation[100]. Hence, open questions are, if the dominant factor is the average dose rate, the peak dose rate, or a combination of both. In addition to that, it is not clear, how oxygen in cytoplasm or water is affected by irradiation with ultra-high dose rates. The present study aims to measure oxygen depletion in sealed water phantoms under irradiation with electron beams at ultra-high dose rate and conventional dose rates, and after irradiation with laser accelerated protons. In that, a combination of different pulse structures was tested in order to understand better the contributions of pulse dose rate and average dose rate to the production of radicals and oxygen depletion. Since it is known, that the FLASH effect depends on oxygen, the measurement of depletion can give insights into the underlying mechanisms in FLASH, and especially the effect of pulse structure at ultra-high dose rates. We found, that, the oxygen depletion was highly dependent on both dose rate and pulse patterns.

Materials and Methods

Water Phantom

To investigate the oxygen depletion in water, sealed water phantoms were used as previously described[110]. The size of the phantoms was 2.5 mm in diameter and 5 mm length. The geometry of the phantoms matched the beam's diameters to ensure that the phantom was homogeneously irradiated. The oxygen level of the water inside the phantom was modified by inducing a gas-exchange in double de-ionized H_2O in a Baker Ruskinn hypoxic chamber with a fixed O_2 level. The water was placed long enough inside the chamber to obtain a O_2 level below 10 % O_2. In the used scale, air saturated water contains 21 %, i.e. 10 % O_2 corresponds to half of the level which could be obtained with air saturated water.

To measure O_2 in the hypoxic chamber and in the water phantoms, TROXSP5 sen-

sors from PyroScience were used. They were 2-point-calibrated, including temperature correction. As previously described, this set-up allowed for non-invasive oxygen measurement before, during, and after irradiation[110]. Hence, it is guaranteed, that the O_2 measurement itself does not have any influence on the O_2 level present in the phantom.

Irradiation Beams

The focus of this study was the measurement of oxygen depletion at ultra-high dose rates of protons and electrons and to investigate the impact of pulse-rate patterns on O_2 depletion. The ultra-high dose rates were obtained for electrons at ELBE, Dresden, Germany. Different combinations of pulse-dose rates and average dose rates were tested (see Tab. A.1). For all tested setups, the electron beam energy was 30 MeV, which corresponds to an LET of 0.27 keV/μm in water.

The beams were configured in a way so that the same target dose was generated, independent from the used settings. The target dose used in these electron experiments was around 28.8 ± 0.5 Gy.

	mean dose rate [Gy/s]	pulse dose rate [Gy/s]	beam type
i)	0.12	10^3	electrons
ii)	180	10^9	electrons
iii)	290	10^6	electrons
iv)	2.5×10^5	10^9	electrons
v)	10^9	10^9	protons
vi)	10	10	photons
vii)	0.17	0.17	photons

Table A.1: Overview on beam pulse settings used for pulse structure - dependent O_2 study

For measurements performed with proton irradiation at ultra-high dose rates, the femto-second laser DRACO was used (Dresden, Germany). In a recent upgrade, DRACO was able to generate doses per pulse of around 20 Gy[111]. In short, the PW-laser shoots at a target, which releases protons which can then be accelerated and filtered by energy. A detailed description of the functioning of DRACO can be found in Brack et al.[21]. In the setting used in the present study, doses of about 20 Gy were
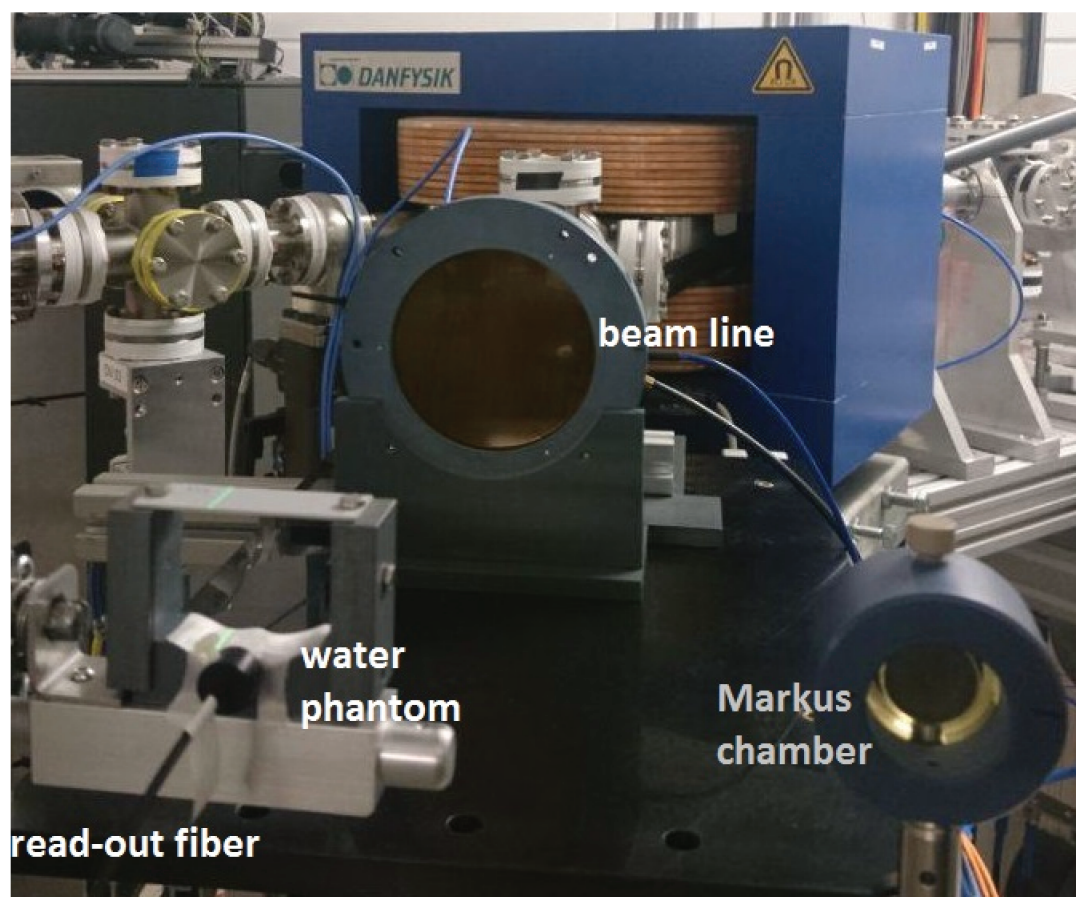
Figure A.1: Experimental set-up at ELBE; irradiation with electrons.

reached, at a pulse dose rate of 10^9 Gy/s. The beam's energy was around 35 MeV (corresponds to an LET of 1.65 keV/μm); beam sharpening done by solenoid coils[21]. In addition, photon radiation was used (200 kV) with continuous beam structure and dose rates of 10 Gy/s and 10 Gy/min.

Dosimetry

Dosimetry was done by EBT3 dosimetric films both at ELBE and DRACO for electron and proton beams. Dosimetric films have a great advantage in ultra-high dose-rate dosimetry, as they deliver dose-rate independent results[18]. In addition to EBT3 film dosimetry, also a Markus chamber was used for electron dosimetry and proton dosimetry. At DRACO, also a newly installed Time-Of-Flight (TOF) dosimetry method was established for a spectral characterization of proton pulses[111].
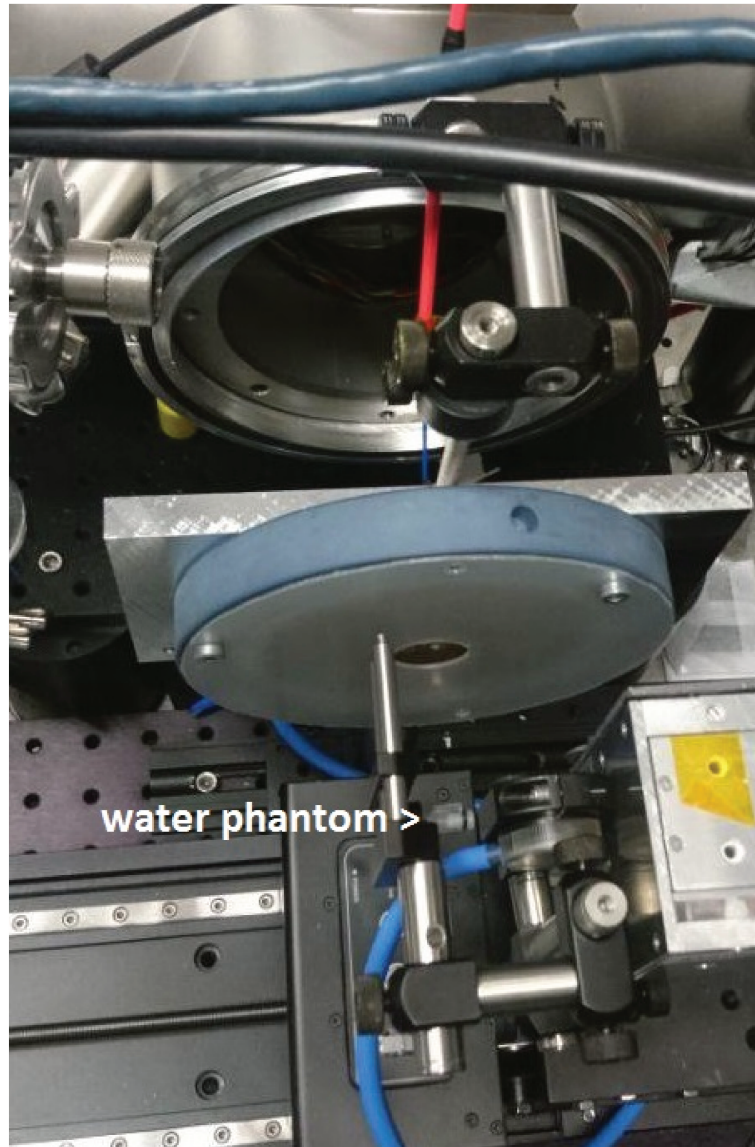
Figure A.2: Experimental set-up: Laser accelerated protons at DRACO.

Measurement Technique

In our previous study[110], O_2 depletion was measured at lower peak dose rates. As a key quantity in the analysis, the average depletion per dose, dO/dD, was determined as it was mostly constant during radiation. This use of gradients is only suitable if the dose rate is slow enough compared to the read-out speed of the O_2 detector. In the present study instead, measurements at ultra-high peak dose rates were performed, which exceeded the read-out-speed by several orders of magnitude. Hence, a defined dose was applied instead of a continuous beam, and the oxygen was measured during the whole process, starting from a plateau value, measuring the decrease during radiation, and also the reaction of radicals plus detector delay after radiation. It was waited, until a steady state was reached after radiation. Then, the difference between starting and end-plateau value was obtained. This difference was named $\Delta c(O_2)$. Using this technique allowed for measurements also at very high peak dose rates and independently on the read-out-speed of the sensor.

Results

Oxygen depletion was measured during radiation for proton, photon, and electron beams for a variety of oxygen levels (see Figure A.3) and peak dose rates. Starting from an equilibrium O_2 level, irradiation caused a drop in O_2 level which reached a new equilibrium after several seconds. The curves were analyzed step-wise in order to make sure, that the equilibrium-states before and after irradiation were compared. The difference in oxygen levels before and after irradiation was determined by the quantity $\Delta c(O_2)$. Then, the ratio of $\Delta c(O_2)$ and the dose needed for the decrease in O_2 was analyzed as a function of the oxygen level present at start of radiation. This analysis was performed on all data obtained from proton, photon and electron measurements. An overview of the results is shown in Figure A.4. In this depiction, the ratio of $\Delta c(O_2)$ and can be directly transformed into a G-value for oxygen depletion. From the data, it became clear that higher LET caused less depletion than low LET radiation. If plotted against O_2 concentration, the G-value data can be fitted with a Michaelis-Menten fit:

$$\frac{\Delta c(O_2)}{D} = \frac{a \cdot c(O_2)}{b + c(O_2)} \tag{A.1}$$

In order to evaluate the dependence of $\Delta c(O_2)/D$ on the peak dose rate and the average dose rate individually, the numerically determined $\Delta c(O_2)/D$ - value was obtained from the Michaelis-Menten fit for a given O_2 level of 3 % and plotted against peak dose rate and average dose rate respectively (see Figure A.5). The fit was applied with a $a + b \cdot \dot{D}^{-0.5}$ dependency as done in a previous study[78,110].
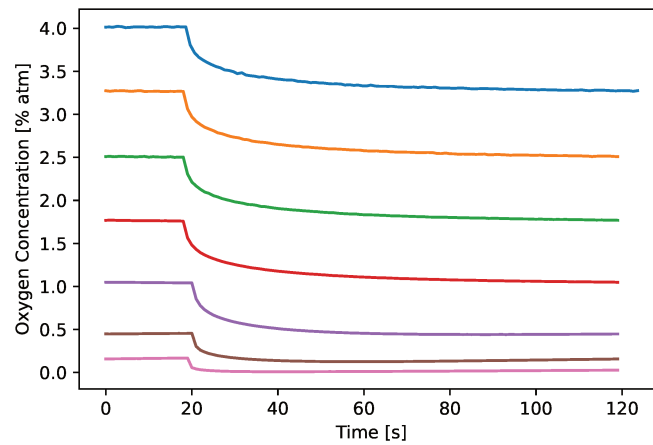
Figure A.3: Oxygen concentration measured within the water phantom as a function of time for different starting O_2 levels. Electron beams of around 28 Gy and 290 Gy/s mean dose rate (configuration iii)) were applied to the phantom at t = 20 s and another 100 s were waited for the phantom's O_2 levels to be in equilibrium again. For further analysis, start- and end-values were used.
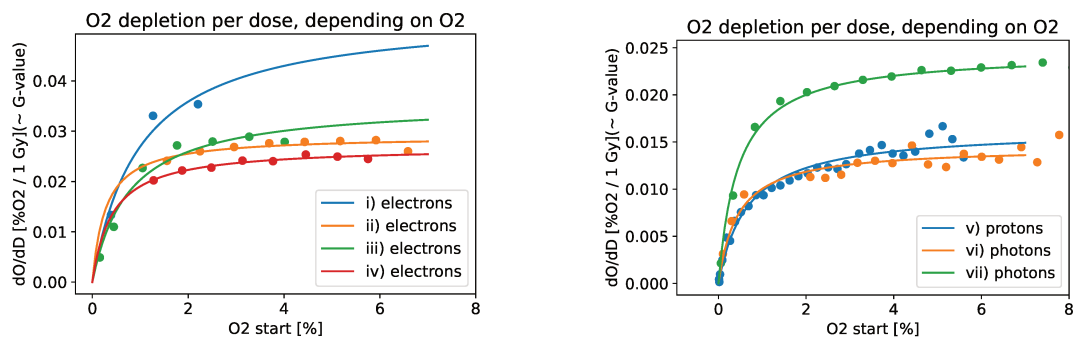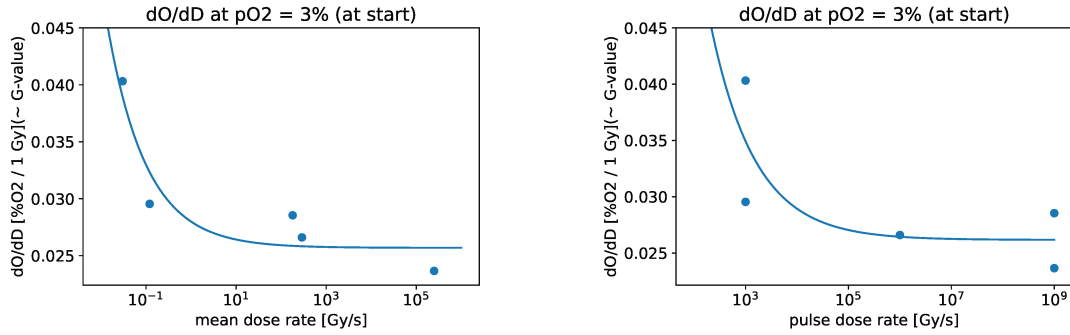

Figure A.4: The ratio of $\Delta c(O_2)$ and the dose applied to the phantom is plotted for each measurement as a function of the initially measured O_2 value. Data are fitted using Michaelis-Menten kinetics.

(a) dO/dD at 3 % O_2 as a function of mean dose rate for electron studies.

(b) dO/dD at 3 % O_2 as a function of pulse dose rate for electron studies.

Figure A.5: Numerically determined $\Delta c(O_2)/D$ at $c(O_2) = 3$ % as a function of pulse dose rate. Fit was done proportionally to (dose rate)$^{-0.5}$ (see [78,110]).

Discussion

The aim of the present study was to investigate the impact of pulse structure and dose rate at ultra-high dose rates on the depletion of O_2 in pure water by measuring the O_2 levels before, after, and during irradiation. Only steady-state O_2-values were taken into account. We observed, that within experiments performed with electrons at the same energy and LET, large differences in the depletion behavior were observed, depending on the pulse structure and dose rate. It was found that higher dose rates depleted less O_2, which was in good agreement with previous results[110]. Also, we observed, for beam configuration ii) and iv), that irradiation with the same pulse dose rates but ii) having a smaller mean dose rate than iv) lead to ii) showed more depletion than iv). From that, it can be concluded that the mean dose rate is more dominant than the pulse dose structure (see Figure A.4 (a) and A.5 (b)). An interesting finding was, that the *G*-values for oxygen consumption determined from the oxygen depletion curves followed the expected Michaelis-Menten-kinetics, but a strong dose-rate and beam structure dependence was visible. In earlier simulation studies[48], an LET-dependence of the *G*-value of oxygen consumption was postulated (and measured by LaVerne et al.[112]), which fit well with the data presented in the present study. Interestingly, it could be shown for the first time in this study, that also dose rate and pulse structure influences the *G*-value. This raises the question, what happens on a radio-chemical basis at ultra-high dose rates, as used for FLASH radiation. Our results strongly suggest that reaction kinetics present in radiolysis in the physio-chemical stage are heavily influenced by the dose rate of the incoming radiation. This might especially be te case if the dose rate is high enough to interfere with reaction velocity, and hence disturb the reactions in a way. In that

case, a higher flux of incoming ionizing radiation causes a higher production rate of primary radicals like for example e_{aq}^-, but less reaction partners are present after the physio-chemical stage to react with oxygen leading to higher abundance of O_2 remaining in water.

This study was carried out in pure water and also here, an effect of FLASH is visible on a radio-chemical level. This finding suggests, that the FLASH effect observed *in-vivo* or in cell culture has at least some fundamental radio-chemical reason, independently from biological mechanisms such as radical scavenging systems, immune-response, or other typically mentioned biological FLASH contributors.

Interestingly, recent studies in cell cultures have shown that FLASH has a protective effect even when comparing the same tissues, instead of healthy tissue vs. cancerous tissue[83]. This protective effect was found also for normoxic conditions.

From the results shown in the present study, it was shown that the difference in G-value was constant for oxygen levels above 1-2 % (i.e. the G-value curves were parallel) and the G-values reaching almost a constant value implying that the O_2 depletion per dose does not depend on O_2 for levels above 2 % and only depend on pulse dose rate. Our results strengthen the hypothesis, that the FLASH-effect is not caused by oxygen depletion, but rather by a change in reaction kinetics of radicals, leading to a decreased abundance of radicals left to interact either with O_2 (as in our measurements) or with cellular compartments or DNA (as in other studies)[77]. In addition to that, an impact of pulse structure on the oxygen depletion was measurable, opening the question on how these findings translate into biological response.

B.1 Oxygen Depletion at Ultra-High Dose Rates For Protons And Electrons: Experimental Approach In Water And Biological Samples

Jeannette Jansen[1,2], Elke Beyreuther[3,4], Jörg Pawelke[3,5], Leonhard Karsch[3,5], Michael Schürer[7,3], Florian Kroll[4], Florian-Emanuel Brack[4,6], Marvin Reimhold[4,6], Josephine Metzges-Ng[4], Ulrich Schramm[4,6], Joao Seco[1,2]

[1] Division of Biomedical Physics in Radiation Oncology, German Cancer Research Center (DKFZ), Heidelberg, Germany

[2] Faculty of Physics and Astronomy, Ruprecht-Karls-University Heidelberg, Germany

[3] OncoRay – National Center for Radiation Research in Oncology, Faculty of Medicine and University Hospital Carl Gustav Carus, TU Dresden and Helmholtz-Zentrum Dresden–Rossendorf, Dresden, Germany

[4] Helmholtz-Zentrum Dresden – Rossendorf (HZDR), Institute of Radiation Physics, Dresden, Germany

[5] Helmholtz-Zentrum Dresden – Rossendorf (HZDR), Institute of Radiooncology - OncoRay, Dresden, Germany

[6] Technische Universität Dresden, Dresden, Germany

[7] National Center for Tumor Diseases (NCT), Partner Site Dresden, Germany: German Cancer Research Center (DKFZ), Heidelberg, Germany

Background and aims   In FLASH radiotherapy (RT), a protective effect of healthy tissue was observed, while tumor control remains comparable to conventional RT. One possible explanation is the oxygen depletion hypothesis, in which radiolysis of water/cytoplasma causes the production of radicals that then react with O_2 dissolved in water. This would cause a reduction in O_2, which results in a hypoxic target and thus a radio-protective effect. In a previous study (Jansen et al. 2021), we measured O_2 depletion using an optical sensor in sealed water phantoms during irradiation at high dose rates (<300 Gy/s) for protons, carbon ions and photons.

Methods   In the study presented here, this experiment was conducted further to ultra-high dose rates (10^9 Gy/s) with protons at DRACO and electrons at ELBE, where also the impact of different pulse structures on O_2 depletion in water was tested. In addition, various settings were tested in order to irradiate zebrafish embryos with FLASH while simultaneously measuring O_2.

Results   We were able to confirm the results of our previous study even at ultra-high dose rates and with electrons. Furthermore, it was possible to measure O_2 depletion during zebrafish embryo irradiation making a simultaneous study of biological response and O_2 depletion possible.

Conclusion   Not enough O_2 was depleted at clinical doses to explain a FLASH effect based on radiation-induced hypoxia. The amount of O_2 depleted per dose depends on dose rate, and higher dose rates deplete slightly less O_2. The experimental set up allows for future joint experiments of biological samples and oxygen monitoring.
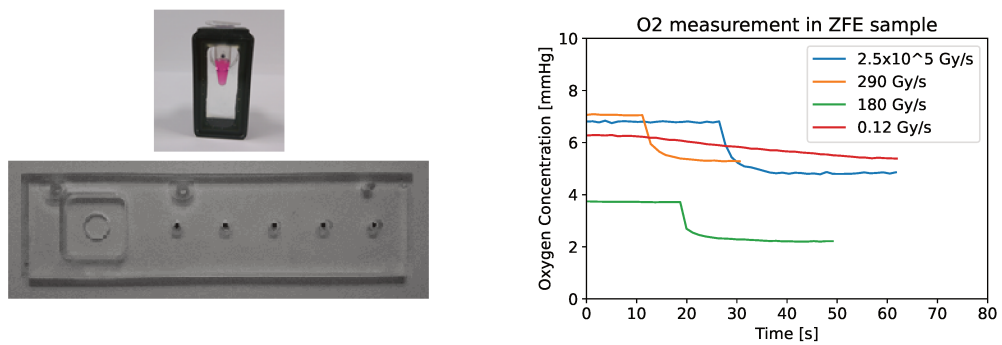
(a) Sample holders for studying O_2 depletion in zebrafish-embryo samples. The black dots are oxygen sensors.

(b) O_2 measurements in zebrafish-embryos at various dose rates.

Figure B.1: Supplement: Sample holder configuration including oxygen sensors and their application in zebrafish-embryo studies under different dose rates.

B.2   Modulating The FLASH Effect On A Cellular Level For Variable Oxygen Levels

Jeannette Jansen[1,2], Jan Knoll[1,2], Karolin Milewski[1,2], Amelie Wüllner[1,2], Rachel Hanley[1,2], Ilenia Aversa[1,3], Francesca Pagliari[1], Luca Tirinato[1,3], Joao Seco[1,2]

[1] Division of Biomedical Physics in Radiation Oncology, German Cancer Research Center (DKFZ), Heidelberg, Germany
[2] Faculty of Physics and Astronomy, Ruprecht-Karls-University Heidelberg, Germany
[3] BioNEM (Bio and Nano Engineering and Technology for Medicine) Laboratory, Department of Experimental and Clinical Medicine, University Magna Graecia of Catanzaro, 88100, Catanzaro, Italy

Background and aims   Several studies in the past suggest that the FLASH effect is due to oxygen depletion: Radiolysis of the cytoplasm would cause radicals which then react with dissolved O_2, creating a hypoxic and thus radio-protective environment. Although biological data show a clear oxygen dependence of the FLASH effect, it is still unclear what the biological mechanism is. In a previous study, we were able to show that less O_2 was depleted at higher dose-rates, which contradicts the oxygen depletion hypothesis. Therefore, other O_2 related mechanisms need to be investigated.

Methods   H460 and PANC1 cells were irradiated with 225kV photons at different dose-rates (2 Gy/min – 40 Gy/s) at low and medium O_2 levels. The O_2 levels were selected between 0.1 %-2 % O_2 using a hypoxic chamber and were monitored with an oxygen sensor in the cells culture flask before, during and after irradiation to allow for stable O_2 conditions.

Results   Preliminary data indicate a clear dependence of the cell survival on both dose-rate and oxygen level. We were able to get robust data for very low O_2 regimes of 0.1 %-2 % O_2 which showed a strong increase of cell survival towards lower O_2 values and this effect being overly dominant in FLASH dose-rates. Further analysis of the impact of oxygen level modulation is ongoing.

Conclusion   Although the FLASH effect depends on oxygen, the mechanism behind is most likely not related to radiation-induced hypoxia. Instead, we will pursue the mechanism in further studies to untangle the strongly linked effects of dose-rate and oxygen exposure.
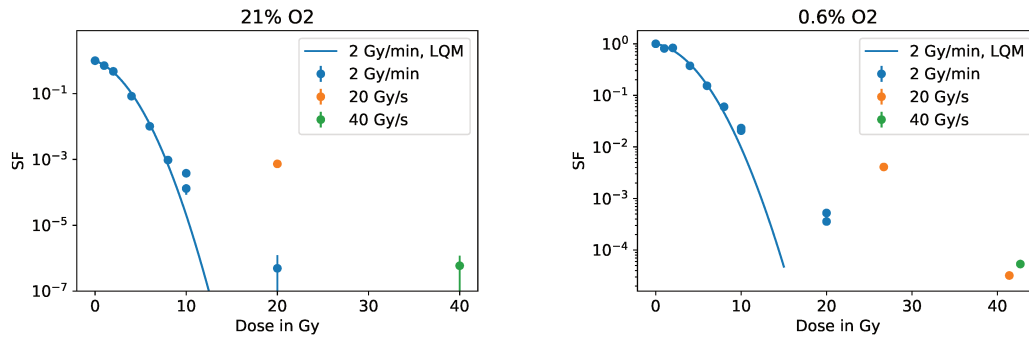

Figure B.2: Supplement: Survival curves of human non-small cell lung cancer cells (H460), cultured in normoxic and hypoxic environment. Irradiated with photons at 2 Gy/min, 20 Gy/s and 40 Gy/s. An overall higher survival was found in hypoxia. In both oxygen conditions, increased survival was measurable at FLASH dose rates. The dose modulating factor was around 2 for both oxygen levels.

List of Scientific Contributions

Peer reviewed articles

P.I **Jansen, J.**, Knoll, J., Beyreuther, E., Pawelke, J., Skuza, R., Hanley, R., Brons, S., Pagliari, F.,& Seco, J. (2021). Does FLASH deplete oxygen? Experimental evaluation for photons, protons, and carbon ions. *Medical Physics*, 48(7), 3982–3990. https://doi.org/10.1002/mp.14917

P.II **Jansen, J.**, Vieten, P., Pagliari, F., Hanley, R., Marafioti, M. G., Tirinato, L., & Seco, J. (2021). A Novel Analysis Method for Evaluating the Interplay of Oxygen and Ionizing Radiation at the Gene Level. *Frontiers in Genetics*, 12, 597635. https://doi.org/10.3389/fgene.2021.597635

P.III Guerreiro, J., Gomes, M.A., Pagliari, F., **Jansen, J.**, Marafioti, M.G., Nisticò, C., Hanley, R., Costa, R.O., Ferreira, S.S., Mendes, F., Fernandes, C., Horn, A., Tirinato, L., & Seco, J. (2020). Iron and copper complexes with antioxidant activity as inhibitors of the metastatic potential of glioma cells. *RSC Advances*, 10, 12699-12710.

P.IV Tirinato, L., Pagliari, F., Di Franco, S., Sogne, E., Marafioti, M. G., **Jansen, J.**, Falqui, A., Todaro, M., Candeloro, P., Liberale, C., Seco, J., Stassi, G., & Di Fabrizio, E. (2019). ROS and Lipid Droplet accumulation induced by high glucose exposure in healthy colon and Colorectal Cancer Stem Cells. *Genes & diseases*, 7(4), 620–635. https://doi.org/10.1016/j.gendis.2019.09.010

Conference Contributions

C.I   **Jansen, J.**, Knoll, J., Beyreuther, E., Pawelke, J., Skuza, R., Hanley, R., Brons, S., Pagliari, F., Seco, J.: **Oral presentation**: Does oxygen depletion occur in FLASH-RT? Experimental evaluation for photons, protons and carbon ions. (Abstract No. PTC59-2325) *PTCOG59, 59th annual meeting of the Particle Therapy Co-Operative Group (PTCOG)* 2021

C.II   **Jansen, J.**, Knoll, J., Skuza, R., Hanley, R., Hehn, L., Echner, G., Brons, S., Pagliari, F., Seco, J.: **Oral presentation**: Implementation of an online oxygen meter for studying oxygen removal during FLASH irradiation. (Abstract No. PTC59-0333) *PTCOG59, 59th annual meeting of the Particle Therapy Co-Operative Group (PTCOG)* 2020

C.III   **Jansen, J.**, Tirinato, L., Marafioti, M.G., Hanley, R., Yao, X.Q., Pagliari, F., Seco, J.: **Poster presentation**: Gene expression of cancer cells in hypoxic and normoxic environment under irradiation. (Abstract No. PTC58-0642) *PTCOG58, 58th annual meeting of the Particle Therapy Co-Operative Group (PTCOG)* 2019

C.IV   **Jansen, J.**, Tirinato, L., Marafioti, M.G., Hanley, R., Yao, X.Q., Pagliari, F., Seco, J.: **Oral Presentation:** Preliminary gene expression results of cancer cells in hypoxic and normoxic environment under irradiation (doi: 10.15129/GSI-2019-00596) *International Biophysis Collaboration Meeting* 2019

C.V   **Jansen, J.**, Tirinato, L., Marafioti, M.G., Yao, X.Q., Hanley, R., Ribeiro, T., Pagliari, F., Seco, J. **Poster Prestentation**: Gene Expression of SK-BR-3 in Hypoxic and Normoxic Environment under Photon Radiation, *3rd Heidelberg Symposium on Novel Techniques in Ion Beam Radiotherapy* 2018

C.VI   Hanley, R., Pagliari, F., Dias, M.F., Marafioti, M.G., **Jansen, J.**, Guerreiro, J., Tirinato, L., Seco, J. **Poster Presentation**: Evaluation of Novel Optical O2 Sensor Spots: Oxygen Consumption Rate of Cancer Cells in Radio-Biology, *3rd Heidelberg Symposium on Novel Techniques in Ion Beam Radiotherapy* 2018

C.VII   Marafioti, M.G., Tirinato, L., Pagliari, F., **Jansen, J.,** Hanley, R., Yao, X.Q., Ribeiro, T., Costanzo, F.S., Seco, J. **Poster presentation**: Lipid Droplets: A new player in radioresistance of breast and lung cancer cells *Frontiers in Cancer Research Conference Heidelberg* 2018

List of Figures

List of Tables

Acronyms

A Adenine. 11, 12

ATP Adenosine Triphosphate. 17, 18

C Cytosine. 11, 12

CAT Catalase. 14, 19, 32, 76, 80

DMF Dose Modifying Factor. 27, 77

DNA DeoxyriboNucleic Acid. 9–11, 13–15, 23, 74

DSB Double Strand Break. 13, 14

EMT Epithelial-To-Mesenchymal-Transition. 32, 77

ER Endoplasmatic Reticulum. 9, 10

G Guanine. 11, 12

GPX Glutathione Peroxidase. 19, 80

GSH Glutathione. 19

HIF1 Hypoxia-inducible Factor 1. 18

HR Homologous Recombination. 14, 18

LET Linear Energy Transfer. 6, 16, 33, 78, 90

LQM Linear Quadratic Model. 15, 16

MMEJ Microhomology-Mediated End Joining. 14

NHEJ Non-Homologous End Joining. 14, 18

OER Oxygen Enhancement Ratio. 16, 17, 22

PCA Principal Component Analysis. 32, 75, 76, 81

RBE Relative Biological Effectiveness. 6, 16

ROS Reactive Oxygen Species. 2, 13, 18, 22, 32, 33, 74, 75, 77, 79, 81, 82

SOD Superoxide Dismutase. 14, 18, 19, 28, 32, 33, 76, 80

SSB Single Strand Break. 13, 14

T Thymine. 11, 12

TOF Time-Of-Flight. 88

UHDR Ultra High Dose Rate. 33, 73, 78

Bibliography

[1] "Global cancer, facts and figures." `https://
www.cancer.org/content/dam/cancer-org/
research/cancer-facts-and-statistics/
global-cancer-facts-and-figures/
global-cancer-facts-and-figures-4th-edition.pdf`. Last
accessed 2021-11-01.

[2] M. Durante and J. S. Loeffler, "Charged particles in radiation oncology," *Nature Reviews Clinical Oncology*, vol. 7, no. 1, pp. 37–43, 2010.

[3] P. Montay-Gruel, K. Petersson, M. Jaccard, G. Boivin, J.-F. Germond, B. Petit, R. Doenlen, V. Favaudon, F. Bochud, C. Bailat, *et al.*, "Irradiation in a flash: Unique sparing of memory in mice after whole brain irradiation with dose rates above 100 Gy/s," *Radiotherapy and Oncology*, vol. 124, no. 3, pp. 365–369, 2017.

[4] M. R. Horsman and J. Overgaard, "The impact of hypoxia and its modification of the outcome of radiotherapy," *Journal of Radiation Research*, vol. 57, no. S1, pp. i90–i98, 2016.

[5] S. Rockwell, I. Dobrucki, E. Kim, S. Marrison, and V. Vu, "Hypoxia and Radiation Therapy: Past History, Ongoing Research, and Future Promise," *Current Molecular Medicine*, vol. 9, pp. 442–458, may 2009.

[6] B. Schlegel, ed., *Medizinische Physik 2*. Springer Verlag, 2002.

[7] Particle Data Group. `https://pdg.lbl.gov/2019/reviews/
rpp2018-rev-passage-particles-matter.pdf`. Last accessed
2021-10-28.

[8] H. Bethe, "Bremsformel für Elektronen relativistischer Geschwindigkeit," *Zeitschrift f. Phys*, vol. 76, p. 293–299, 1932.

[9] P. Zyla *et al.*, "Review of Particle Physics," *PTEP*, vol. 2020, no. 8, p. 083C01, 2020.

[10] J. Bourhis, P. Montay-Gruel, P. G. Jorge, C. Bailat, B. Petit, J. Ollivier, W. Jeanneret-Sozzi, M. Ozsahin, F. Bochud, R. Moeckli, *et al.*, "Clinical translation of FLASH radiotherapy: Why and how?," *Radiotherapy and Oncology*, vol. 139, pp. 11–17, 2019.

[11] R. Moeckli, P. Gonçalves Jorge, V. Grilj, R. Oesterle, N. Cherbuin, J. Bourhis, M.-C. Vozenin, J.-F. Germond, F. Bochud, and C. Bailat, "Commissioning of an ultra-high dose rate pulsed electron beam medical linac for FLASH RT preclinical animal experiments and future clinical human protocols," *Medical Physics*, vol. 48, no. 6, pp. 3134–3142, 2021.

[12] M. Rahman, M. R. Ashraf, R. Zhang, P. Bruza, C. A. Dexter, L. Thompson, X. Cao, B. B. Williams, P. J. Hoopes, B. W. Pogue, and D. J. Gladstone, "Electron FLASH Delivery at Treatment Room Isocenter for Efficient Reversible Conversion of a Clinical LINAC," *International Journal of Radiation Oncology*Biology*Physics*, vol. 110, no. 3, pp. 872–882, 2021.

[13] A. Büchner, F. Gabriel, E. Grosse, P. Michel, W. Seidel, and J. Voigtländer, "The ELBE-Project at Dresden-Rossendorf," *EPAC'00, Vienna, June*, 2000.

[14] F. Gabriel, P. Gippner, E. Grosse, D. Janssen, P. Michel, H. Prade, A. Schamlott, W. Seidel, A. Wolf, R. Wünsch, *et al.*, "The Rossendorf radiation source ELBE and its FEL projects," *Nuclear Instruments and Methods in Physics Research Section B: Beam Interactions with Materials and Atoms*, vol. 161, pp. 1143–1147, 2000.

[15] U. A. Weber, E. Scifoni, and M. Durante, "FLASH radiotherapy with carbon ion beams," *Medical Physics*, 2021.

[16] R. Singh, P. Forck, P. Boutachkov, S. Sorge, and H. Welker, "Slow Extraction Spill Characterization From Micro to Milli-Second Scale," vol. 1067, p. 072002, 2018.

[17] T. Tessonnier, S. Mein, D. W. Walsh, N. Schuhmacher, H. Liew, R. Cee, M. Galonska, S. Scheloske, C. Schömers, U. Weber, *et al.*, "FLASH dose-rate helium ion beams: first in vitro investigations," *International Journal of Radiation Oncology* Biology* Physics*, 2021.

[18] L. Karsch, E. Beyreuther, T. Burris-Mog, S. Kraft, C. Richter, K. Zeil, and J. Pawelke, "Dose rate dependence for different dosimeters and detectors:

TLD, OSL, EBT films, and diamond detectors," *Medical Physics*, vol. 39, no. 5, pp. 2447–2455, 2012.

[19] L. Karsch, E. Beyreuther, W. Enghardt, M. Gotz, U. Masood, U. Schramm, K. Zeil, and J. Pawelke, "Towards ion beam therapy based on laser plasma accelerators," *Acta Oncologica*, vol. 56, no. 11, pp. 1359–1366, 2017. PMID: 28828925.

[20] P. Chaudhary, G. Milluzzo, H. Ahmed, B. Odlozilik, A. McMurray, K. M. Prise, and M. Borghesi, "Radiobiology experiments with ultra-high dose rate laser-driven protons: Methodology and state-of-the-art," *Frontiers in Physics*, vol. 9, p. 75, 2021.

[21] F.-E. Brack, F. Kroll, L. Gaus, C. Bernert, E. Beyreuther, T. E. Cowan, L. Karsch, S. Kraft, L. A. Kunz-Schughart, E. Lessmann, *et al.*, "Spectral and spatial shaping of laser-driven proton beams using a pulsed high-field magnet beamline," *Scientific reports*, vol. 10, no. 1, pp. 1–12, 2020.

[22] Wikimedia, "Animal cell." `https://upload.wikimedia.org/wikipedia/commons/1/11/AnimalCell.svg?uselang=de`. Last accessed 2021-10-30.

[23] J. H. Chung, Y. Zhang, and F. Bunz, "Checkpoint bypass and cell viability," *Cell Cycle*, vol. 9, no. 11, pp. 2102–2107, 2010.

[24] R. Watanabe and K. Saito, "Monte Carlo simulation of water radiolysis in oxygenated condition for monoenergetic electrons from 100eV to 1MeV," *Radiation Physics and Chemistry*, vol. 62, no. 2, pp. 217–228, 2001.

[25] J. Ward, "DNA Damage Produced by Ionizing Radiation in Mammalian Cells: Identities, Mechanisms of Formation, and Reparability," *Progress in Nucleic Acid Research and Molecular Biology*, vol. 35, pp. 95–125, 1988.

[26] J. Cadet, C. D'Ham, T. Douki, J.-P. Pouget, J.-L. Ravanat, and S. Sauvaigo, "Facts and artifacts in the measurement of oxidative base damage to DNA," *Free radical research*, vol. 29, no. 6, pp. 541–550, 1998.

[27] A. P. Breen and J. A. Murphy, "Reactions of oxyl radicals with DNA," *Free radical biology and medicine*, vol. 18, no. 6, pp. 1033–1077, 1995.

[28] D. T. Goodhead, "Initial events in the cellular effects of ionizing radiations: clustered damage in DNA," *International journal of radiation biology*, vol. 65, no. 1, pp. 7–17, 1994.

[29] C. von Sonntag, *The chemical basis of radiation biology*, ch. DNA model systems: the base moity, pp. 116–166. Taylor & Francis London, 1987.

[30] C. von Sonntag, *The chemical basis of radiation biology*, ch. DNA model systems: the sugar phosphate moity, pp. 167–193. Taylor & Francis London, 1987.

[31] W. A. Pryor, "Oxy-radicals and related species: their formation, lifetimes, and reactions," *Annual review of Physiology*, vol. 48, no. 1, pp. 657–667, 1986.

[32] A. Phaniendra, D. B. Jestadi, and L. Periyasamy, "Free radicals: properties, sources, targets, and their implication in various diseases," *Indian journal of clinical biochemistry*, vol. 30, no. 1, pp. 11–26, 2015.

[33] R. Willson, "The reaction of oxygen with radiation-induced free radicals in DNA and related compounds," *International Journal of Radiation Biology and Related Studies in Physics, Chemistry and Medicine*, vol. 17, no. 4, pp. 349–358, 1970.

[34] B. Giese, "Long-distance charge transport in DNA: the hopping mechanism," *Accounts of chemical research*, vol. 33, no. 9, pp. 631–636, 2000.

[35] J. Ward, "The yield of DNA double-strand breaks produced intracellularly by ionizing radiation: a review," *International journal of radiation biology*, vol. 57, no. 6, pp. 1141–1150, 1990.

[36] K. Rothkamm, I. Kruger, L. H. Thompson, and M. Löbrich, "Pathways of DNA double-strand break repair during the mammalian cell cycle," *Molecular and cellular biology*, vol. 23, no. 16, pp. 5706–5715, 2003.

[37] S. J. Mcmahon, "The linear quadratic model: usage, interpretation and challenges," *Physics in Medicine & Biology*, vol. 64, p. aaf26a, 2019.

[38] J. K. Moore and J. E. Haber, "Cell cycle and genetic requirements of two pathways of nonhomologous end-joining repair of double-strand breaks in saccharomyces cerevisiae," *Molecular and cellular biology*, vol. 16, no. 5, pp. 2164–2173, 1996.

[39] S. J. Boulton and S. P. Jackson, "Saccharomyces cerevisiae Ku70 potentiates illegitimate DNA double-strand break repair and serves as a barrier to error-prone DNA repair pathways.," *The EMBO journal*, vol. 15, no. 18, pp. 5093–5103, 1996.

[40] L. H. Thompson and D. Schild, "Homologous recombinational repair of DNA ensures mammalian chromosome stability," *Mutation Research/Fundamental and Molecular Mechanisms of Mutagenesis*, vol. 477, no. 1, pp. 131–153, 2001. Analysis and Prevention of Carcinogenesis in Animal Models.

[41] M. McVey and S. E. Lee, "MMEJ repair of double-strand breaks (director's cut): deleted sequences and alternative endings," *Trends in Genetics*, vol. 24, no. 11, pp. 529–538, 2008.

[42] G. Iliakis, Y. Wang, J. Guan, and H. Wang, "DNA damage checkpoint control in cells exposed to ionizing radiation," *Oncogene*, vol. 22, no. 37, pp. 5834–5847, 2003.

[43] N. A. Franken, H. M. Rodermond, J. Stap, J. Haveman, and C. Van Bree, "Clonogenic assay of cells in vitro," *Nature protocols*, vol. 1, no. 5, pp. 2315–2319, 2006.

[44] R. G. Dale, "The application of the linear-quadratic dose-effect equation to fractionated and protracted radiotherapy," *The British journal of radiology*, vol. 58, no. 690, pp. 515–528, 1985.

[45] S. J. McMahon, "The linear quadratic model: usage, interpretation and challenges," *Physics in Medicine & Biology*, vol. 64, no. 1, p. 01TR01, 2018.

[46] T. Wenzl and J. J. Wilkens, "Modelling of the oxygen enhancement ratio for ion beam radiation therapy," *Physics in Medicine and Biology*, vol. 56, pp. 3251–3268, jun 2011.

[47] W. Tinganelli, M. Durante, R. Hirayama, M. Krämer, A. Maier, W. Kraft-Weyrather, Y. Furusawa, T. Friedrich, and E. Scifoni, "Kill-painting of hypoxic tumours in charged particle therapy," *Scientific reports*, vol. 5, no. 1, pp. 1–13, 2015.

[48] D. Boscolo, M. Krämer, M. C. Fuss, M. Durante, and E. Scifoni, "Impact of target oxygenation on the chemical track evolution of ion and electron radiation," *International Journal of Molecular Sciences*, vol. 21, no. 2, p. 424, 2020.

[49] T. Alper and P. Howard-Flanders, "Role of oxygen in modifying the radiosensitivity of E. coli B.," *Nature*, vol. 178, no. 4540, p. 978, 1956.

[50] S. McKeown, "Defining normoxia, physoxia and hypoxia in tumours—implications for treatment response," *The British journal of radiology*, vol. 87, no. 1035, p. 20130676, 2014.

[51] O. Trédan, C. M. Galmarini, K. Patel, and I. F. Tannock, "Drug resistance and the solid tumor microenvironment," *Journal of the National Cancer Institute*, vol. 99, p. 1441—1454, October 2007.

[52] R. H. Thomlinson and L. Gray, "The histological structure of some human lung cancers and the possible implications for radiotherapy," *British journal of cancer*, vol. 9, no. 4, p. 539, 1955.

[53] N. Chaudary and R. P. Hill, "Hypoxia and metastasis," *Clinical Cancer Research*, vol. 13, no. 7, pp. 1947–1949, 2007.

[54] J. Brown, "Evidence for acutely hypoxic cells in mouse tumours, and a possible mechanism of reoxygenation," *The British journal of radiology*, vol. 52, no. 620, pp. 650–656, 1979.

[55] M. G. V. Heiden, L. C. Cantley, and C. B. Thompson, "Understanding the warburg effect: The metabolic requirements of cell proliferation," *Science*, vol. 324, no. 5930, pp. 1029–1033, 2009.

[56] U. G. A. Sattler and W. Mueller-Klieser, "The anti-oxidant capacity of tumour glycolysis," *International Journal of Radiation Biology*, vol. 85, no. 11, pp. 963–971, 2009.

[57] R. G. Bristow and R. P. Hill, "Hypoxia, DNA repair and genetic instability," *Nature Reviews Cancer*, vol. 8, no. 3, pp. 180–192, 2008.

[58] L. Miao and D. K. St. Clair, "Regulation of superoxide dismutase genes: Implications in disease," *Free Radical Biology and Medicine*, vol. 47, no. 4, pp. 344–356, 2009.

[59] C. K. Tsang, Y. Liu, J. Thomas, Y. Zhang, and X. S. Zheng, "Superoxide dismutase 1 acts as a nuclear transcription factor to regulate oxidative stress resistance," *Nature communications*, vol. 5, no. 1, pp. 1–11, 2014.

[60] C. D. Putnam, A. S. Arvai, Y. Bourne, and J. A. Tainer, "Active and inhibited human catalase structures: ligand and NADPH binding and catalytic mechanism," *Journal of Molecular Biology*, vol. 296, no. 1, pp. 295–309, 2000.

[61] V. Favaudon, R. Labarbe, and C. L. Limoli, "Model studies of the role of oxygen in the FLASH effect," *Medical Physics*, 2021.

[62] S. Hornsey and T. Alper, "Unexpected dose-rate effect in the killing of mice by radiation," *Nature*, vol. 210, no. 5032, pp. 212–213, 1966.

[63] V. Favaudon, L. Caplier, V. Monceau, F. Pouzoulet, M. Sayarath, C. Fouil-lade, M. F. Poupon, I. Brito, P. Hupé, J. Bourhis, J. Hall, J. J. Fontaine, and M. C. Vozenin, "Ultrahigh dose-rate FLASH irradiation increases the differential response between normal and tumor tissue in mice," *Science Translational Medicine*, vol. 6, no. 245, pp. 1–10, 2014.

[64] M.-C. Vozenin, P. De Fornel, K. Petersson, V. Favaudon, M. Jaccard, J.-F. Germond, B. Petit, M. Burki, G. Ferrand, D. Patin, *et al.*, "The advantage of FLASH radiotherapy confirmed in mini-pig and cat-cancer patients," *Clinical Cancer Research*, vol. 25, no. 1, pp. 35–42, 2019.

[65] J. Pawelke, M. Brand, S. Hans, K. Hideghéty, L. Karsch, E. Lessmann, S. Löck, M. Schürer, E. R. Szabó, and E. Beyreuther, "Electron dose rate and oxygen depletion protect zebrafish embryos from radiation damage," *Radiotherapy and Oncology*, vol. 158, pp. 7–12, 2021.

[66] J. Bourhis, W. J. Sozzi, P. G. Jorge, O. Gaide, C. Bailat, F. Duclos, D. Patin, M. Ozsahin, F. Bochud, J.-F. Germond, *et al.*, "Treatment of a first patient with FLASH-radiotherapy," *Radiotherapy and oncology*, vol. 139, pp. 18–22, 2019.

[67] G. Pratx and D. S. Kapp, "A computational model of radiolytic oxygen depletion during FLASH irradiation and its effect on the oxygen enhancement ratio," *Physics in Medicine & Biology*, vol. 64, no. 18, p. 185005, 2019.

[68] G. Adrian, E. Konradsson, M. Lempart, S. Bäck, C. Ceberg, and K. Petersson, "The FLASH effect depends on oxygen concentration," *The British journal of radiology*, vol. 92, no. 1106, p. 20190702, 2020.

[69] P. Montay-Gruel, M. M. Acharya, K. Petersson, L. Alikhani, C. Yakkala, B. D. Allen, J. Ollivier, B. Petit, P. G. Jorge, A. R. Syage, *et al.*, "Long-term neurocognitive benefits of FLASH radiotherapy driven by reduced reactive oxygen species," *Proceedings of the National Academy of Sciences*, vol. 116, no. 22, pp. 10943–10951, 2019.

[70] E. S. Diffenderfer, B. S. Sørensen, A. Mazal, and D. J. Carlson, "The current status of pre-clinical proton flash radiation and future directions," *Medical Physics*, 2021.

[71] K. Petersson, G. Adrian, K. Butterworth, and S. J. McMahon, "A quantitative analysis of the role of oxygen tension in FLASH radiotherapy," *International Journal of Radiation Oncology* Biology* Physics*, 2020.

[72] D. Boscolo, M. Krämer, M. Durante, M. Fuss, and E. Scifoni, "Trax-chem: A pre-chemical and chemical stage extension of the particle track structure code trax in water targets," *Chemical Physics Letters*, vol. 698, pp. 11–18, 2018.

[73] R. Skuza, "FLASH effect: An investigation into radical dynamics of H2O," Master's thesis, University of Heidelberg, 2020.

[74] D. Boscolo, E. Scifoni, M. Durante, M. Krämer, and M. C. Fuss, "May oxygen depletion explain the FLASH effect? a chemical track structure analysis," *Radiotherapy and Oncology*, vol. 162, pp. 69–75, 2021.

[75] P. Wilson, B. Jones, T. Yokoi, M. Hill, and B. Vojnovic, "Revisiting the ultra-high dose rate effect: implications for charged particle radiotherapy using protons and light ions," *The British journal of radiology*, vol. 85, no. 1018, pp. e933–e939, 2012.

[76] M. Durante, E. Bräuer-Krisch, and M. Hill, "Faster and safer? FLASH ultra-high dose rate in radiotherapy," *The British journal of radiology*, vol. 91, no. 1082, p. 20170628, 2018.

[77] R. Labarbe, L. Hotoiu, J. Barbier, and V. Favaudon, "A physicochemical model of reaction kinetics supports peroxyl radical recombination as the main determinant of the FLASH effect," *Radiotherapy and Oncology*, 2020.

[78] B. Mihaljević, I. Tartaro, C. Ferreri, and C. Chatgilialoglu, "Linoleic acid peroxidation vs. isomerization: a biomimetic model of free radical reactivity in the presence of thiols," *Organic & biomolecular chemistry*, vol. 9, no. 9, pp. 3541–3548, 2011.

[79] P. Wardman, "Radiotherapy using high-intensity pulsed radiation beams (FLASH): a radiation-chemical perspective," *Radiation research*, vol. 194, no. 6, pp. 607–617, 2020.

[80] R. Moeckli, J.-F. Germond, C. Bailat, F. Bochud, M.-C. Vozenin, and J. Bourhis, "In Regard to van Marlen et al," *International Journal of Radiation Oncology, Biology, Physics*, vol. 107, no. 5, pp. 1012–1013, 2020.

[81] S. Acharya, N. Bhat, P. Joseph, G. Sanjeev, B. Sreedevi, and Y. Narayana, "Dose rate effect on micronuclei induction in human blood lymphocytes exposed to single pulse and multiple pulses of electrons," *Radiation and environmental biophysics*, vol. 50, no. 2, pp. 253–263, 2011.

[82] C. Fouillade, S. Curras-Alonso, L. Giuranno, E. Quelennec, S. Heinrich, S. Bonnet-Boissinot, A. Beddok, S. Leboucher, H. U. Karakurt, M. Bohec, *et al.*,

"FLASH irradiation spares lung progenitor cells and limits the incidence of radio-induced senescence," *Clinical Cancer Research*, vol. 26, no. 6, pp. 1497–1506, 2020.

[83] G. Adrian, E. Konradsson, S. Beyer, A. Wittrup, K. T. Butterworth, S. J. McMahon, M. Ghita, K. Petersson, and C. Ceberg, "Cancer Cells Can Exhibit a Sparing FLASH Effect at Low Doses Under Normoxic In Vitro-Conditions," *Frontiers in Oncology*, p. 2890, 2021.

[84] M. Buonanno, V. Grilj, and D. J. Brenner, "Biological effects in normal cells exposed to FLASH dose rate protons," *Radiotherapy and Oncology*, vol. 139, pp. 51–55, 2019.

[85] E. Bayart, A. Flacco, O. Delmas, L. Pommarel, D. Levy, M. Cavallone, F. Megnin-Chanet, E. Deutsch, and V. Malka, "Fast dose fractionation using ultra-short laser accelerated proton pulses can increase cancer cell mortality, which relies on functional PARP1 protein," *Scientific reports*, vol. 9, no. 1, pp. 1–10, 2019.

[86] Y. Lai, X. Jia, and Y. Chi, "Modeling the effect of oxygen on the chemical stage of water radiolysis using GPU-based microscopic Monte Carlo simulations, with an application in FLASH radiotherapy," *Physics in Medicine & Biology*, vol. 66, no. 2, p. 025004, 2021.

[87] X. Cao, R. Zhang, T. V. Esipova, S. R. Allu, R. Ashraf, M. Rahman, J. R. Gunn, P. Bruza, D. J. Gladstone, B. B. Williams, *et al.*, "Quantification of oxygen depletion during FLASH irradiation in vitro and in vivo," *International Journal of Radiation Oncology* Biology* Physics*, 2021.

[88] P. Hernansanz-Agustín, A. Izquierdo-Álvarez, F. J. Sánchez-Gómez, E. Ramos, T. Villa-Piña, S. Lamas, A. Bogdanova, and A. Martínez-Ruiz, "Acute hypoxia produces a superoxide burst in cells," *Free Radical Biology and Medicine*, vol. 71, pp. 146–156, 2014.

[89] C.-Y. Huang, S.-F. Chiang, T.-W. Ke, T.-W. Chen, Y.-S. You, W. T. L. Chen, and K. S. C. Chao, "Clinical significance of programmed infiltration in stage II III colorectal cancer," *Scientific Reports*, vol. 8, no. 15658, pp. 1–10, 2018.

[90] A. Minty, P. Chalon, J.-M. Derocq, X. Dumont, J.-C. Guillemot, M. Kaghad, C. Labit, P. Leplatois, P. Liauzun, B. Miloux, *et al.*, "Interleukin-13 is a new human lymphokine regulating inflammatory and immune responses," *Nature*, vol. 362, no. 6417, pp. 248–250, 1993.

[91] R. L. G. Iii, T. R. Ramalingam, K. M. Hart, K. M. Vannella, D. A. Cantu, W.-y. Lu, S. Ferreira-gonzález, S. J. Forbes, L. Vallier, and T. A. Wynn, "Interleukin-13 activates distinct cellular pathways leading to ductular reaction, steatosis, and fibrosis," *Immunity*, vol. 45, no. 1, pp. 145–158, 2019.

[92] H. S. Eun, S. Y. Cho, J. S. Joo, S. H. Kang, H. S. Moon, E. S. Lee, S. H. Kim, and B. S. Lee, "Gene expression of NOX family members and their clinical significance in hepatocellular carcinoma," *Scientific Reports*, vol. 7, no. 11060, pp. 1–10, 2017.

[93] K. Benihoud, S. Esselin, D. Descamps, B. Jullienne, B. Salone, P. Bobe, D. Bonardelle, E. Connault, P. Opolon, I. Saggio, and M. Perricaudet, "Respective roles of TNF- α and IL-6 in the immune response-elicited by adenovirus-mediated gene transfer in mice," *Gene Therapy*, vol. 14, pp. 533–544, 2007.

[94] Y. Jiang, J. Chen, E. Bi, Y. Zhao, T. Qin, Y. Wang, A. Wang, S. Gao, Q. Yi, and S. Wang, "TNF- α enhances Th9 cell differentiation and antitumor immunity via TNFR2-dependent pathways," *Journal of ImmunoTherapyof Cancer*, vol. 7, no. 28, pp. 1–12, 2019.

[95] P. Singh, P. de Souza, K. F. Scott, B. M. Hall, N. D. Verma, T. M. Becker, J. W. Toh, M. Sajinovic, and K. J. Spring, "Biomarkers in immune checkpoint inhibition therapy for cancer patients: what is the role of lymphocyte subsets and PD1/PD-L1?," *Translational Medicine Communications*, vol. 4, no. 1, pp. 1–13, 2019.

[96] D. S. Gridley, L. M. Green, G. A. Nelson, M. J. Pecaut, and J. M. Slater, "Therapeutic utilities of SOD mimetics: cancer, radiotherapy and SOD mimetics," in *Madame Curie Bioscience Database*, Landes Bioscience, 2013.

[97] M. Che, R. Wang, X. Li, H.-Y. Wang, and X. S. Zheng, "Expanding roles of superoxide dismutases in cell regulation and cancer," *Drug discovery today*, vol. 21, no. 1, pp. 143–149, 2016.

[98] J. Lu, Y. Zhong, J. Chen, X. Lin, Z. Lin, N. Wang, and S. Lin, "Radiation Enhances the Epithelial–Mesenchymal Transition of A549 Cells via miR3591-5p/USP33/PPM1A," *Cellular Physiology and Biochemistry*, vol. 50, no. 2, pp. 721–733, 2018.

[99] M.-C. Vozenin, J. H. Hendry, and C. Limoli, "Biological benefits of ultra-high dose rate FLASH radiotherapy: sleeping beauty awoken," *Clinical oncology*, vol. 31, no. 7, pp. 407–415, 2019.

[100] M.-C. Vozenin, P. Montay-Gruel, C. Limoli, and J.-F. Germond, "All irradiations that are ultra-high dose rate may not be FLASH: the critical importance of beam parameter characterization and in vivo validation of the FLASH effect," *Radiation Research*, vol. 194, no. 6, pp. 571–572, 2020.

[101] P. Montay-Gruel, M. M. Acharya, P. G. Jorge, B. Petit, I. G. Petridis, P. Fuchs, R. Leavitt, K. Petersson, M. Gondré, J. Ollivier, *et al.*, "Hypofractionated FLASH-RT as an effective treatment against glioblastoma that reduces neurocognitive side effects in mice," *Clinical Cancer Research*, vol. 27, no. 3, pp. 775–784, 2021.

[102] C.-H. Wu, S.-C. Tang, P.-H. Wang, H. Lee, and J.-L. Ko, "Nickel-induced epithelial-mesenchymal transition by reactive oxygen species generation and E-cadherin promoter hypermethylation," *Journal of Biological Chemistry*, vol. 287, no. 30, pp. 25292–25302, 2012.

[103] W. Lv, L. Sui, X. Yan, H. Xie, L. Jiang, C. Geng, Q. Li, X. Yao, Y. Kong, and J. Cao, "ROS-dependent Atg4 upregulation mediated autophagy plays an important role in Cd-induced proliferation and invasion in A549 cells," *Chemico-Biological Interactions*, vol. 279, pp. 136–144, 2018.

[104] C. Ninsontia, P. P. Phiboonchaiyanan, and P. Chanvorachote, "Zinc induces epithelial to mesenchymal transition in human lung cancer H460 cells via superoxide anion-dependent mechanism," *Cancer cell international*, vol. 16, no. 1, pp. 1–16, 2016.

[105] M. Wank, D. Schilling, T. E. Schmid, B. Meyer, J. Gempt, M. Barz, J. Schlegel, F. Liesche, K. A. Kessel, B. Wiestler, *et al.*, "Human glioma migration and infiltration properties as a target for personalized radiation medicine," *Cancers*, vol. 10, no. 11, p. 456, 2018.

[106] Y. Zhang, Z. Ding, J. Perentesis, D. Khuntia, S. Pfister, and R. Sharma, "Can rational combination of ultra-high dose rate FLASH radiotherapy with immunotherapy provide a novel approach to cancer treatment?," *Clinical Oncology*, vol. 33, no. 11, pp. 713–722, 2021. Clinical Applications of Novel Radiobiology.

[107] J. Boustani, B. Lecoester, J. Baude, C. Latour, O. Adotevi, C. Mirjolet, and G. Truc, "Anti-PD-1/Anti-PD-L1 Drugs and Radiation Therapy: Combinations and Optimization Strategies," *Cancers*, vol. 13, no. 19, 2021.

[108] H. Weiss, E. R. Epp, J. M. Heslin, C. C. Ling, and A. Santomasso, "Oxygen depletion in cells irradiated at ultra-high dose-rates and at conventional dose-rates," *International Journal of Radiation Biology*, vol. 26, no. 1, pp. 17–29, 1974.

[109] J. D. Wilson, E. M. Hammond, G. S. Higgins, and K. Petersson, "Ultra-high dose rate (FLASH) radiotherapy: Silver bullet or fool's gold?," *Frontiers in Oncology*, vol. 9, p. 1563, 2020.

[110] J. Jansen, J. Knoll, E. Beyreuther, J. Pawelke, R. Skuza, R. Hanley, S. Brons, F. Pagliari, and J. Seco, "Does FLASH deplete oxygen? Experimental evaluation for photons, protons, and carbon ions," *Medical Physics*, vol. 48, no. 7, pp. 3982–3990, 2021.

[111] F.-E. Brack, F. Kroll, L. Gaus, C. Bernert, E. Beyreuther, T. E. Cowan, L. Karsch, S. D. Kraft, E. Lessmann, J. Metzkes-Ng, J. Pawelke, M. Rehwald, M. Reimold, H.-P. Schlenvoigt, U. Schramm, M. Sobiella, M. E. P. Umlandt, T. Ziegler, and K. Zeil, "Fully characterised and online monitored beamline for high-dose-rate laser-proton irradiation experiments at Draco PW," in *Applying Laser-driven Particle Acceleration II, Medical and Nonmedical Uses of Distinctive Energetic Particle and Photon Sources: SPIE Optics + Optoelectronics Industry Event* (P. R. Bolton, ed.), vol. 11790, International Society for Optics and Photonics, SPIE, 2021.

[112] J. A. LaVerne and R. H. Schuler, "Track effects in radiation chemistry: production of hydroperoxy radical in the radiolysis of water by high-LET nickel-58 ions," *Journal of Physical Chemistry*, vol. 91, no. 26, pp. 6560–6563, 1987.

Acknowledgments

Now that this thesis is written, I want to thank so many people who made this thesis and the project possible.

First of all, my thank goes to Prof. Joao Seco, for being a wonderful supervisor. He had always an open door when it came to research ideas and gave a lot of support during the last years. Also, I am very happy to be part of the wonderful E041 group, which has been a really amazing experience. No matter if it was for doing science together or for going skiing, climbing, for a drink, or just chatting over a coffee - it has always been a pleasure.

Also my great thanks to Prof. Oliver Jäkel for being a very supportive member of my TAC and the second examiner. Already during my Master's thesis, he gave me the opportunity to do research in his group, which was a great time and led to me starting a PhD.

Many thanks go to Luca Tirinato and Francesca Pagliari, who taught me so many things in the bio-lab so that I became nearly a biocists... the hybrid of biologist and physicist. Without them I would not work in the lab as I do.

For me, an important point to stress is the HGSFP, the graduate school which provided me with all the support, a PhD student can think of. I am very grateful for the many opportunities this brought to me, from courses, over the legendary winterschools, and the opportunity of being involved in the organization of one myself. I've made great friends over this time, which I am very glad for.

Joining the Helmholtz DKFZ International PhD Program, opened many opportunities I could only have dreamt about at the beginning of the thesis. The last years have really been an immense change in my personal direction, towards a scientific career. I am very grateful for meeting Elke Beyreuther during that program. Thank you, Elke, for supporting me in many ways, not only professionally, but also on a personal level. I hope we will have many other fun beam times and time around beam times together.

I also want to thank my proof readers. It was a huge help!

Last but definitely not least: Thank you to my family; my parents, my sister and my cousin who have always supported me. To know that I always have their back

> *Remember to look up at the stars and not down at your feet.*
>
> — Stephen Hawking